The development of population-wide descriptions of human rib and rib cage geometry

by

Sven Alan Holcombe

A dissertation submitted in partial fulfillment
of the requirements for the degree of
Doctor of Philosophy
(Biomedical Engineering)
in the University of Michigan
2016

Doctoral Committee:

Professor James B. Grotberg, Co-Chair
Professor Stewart C. Wang, Co-Chair
Assistant Professor Clive D'Souza
Professor Douglas Noll

2016

Dedication

To Todd, Rose, Mum, Dad, and my family and friends in Australia.

Acknowledgments

Dr. James Grotberg and Dr. Stewart Wang have each been tremendous advisors throughout my PhD. I have noticed a shared quality that has been exceptionally valuable to me – that of vision and foresight. Their advice extends beyond my usual scope of "this week" and they've always helped me to notice the bigger picture either within a research topic or (most frequently) in my academic career as a whole. Individually, Jim, thank you in particular for seeing a spiral and pushing me out of my comfort zone to make it work. Your advice mixed with your humor while giving it have been greatly valuable and for that you will always have my respect and appreciation. To Stu, thank you for the huge amounts of trust, support, and direction that you have given me since we met in Japan 10 years ago. I can only marvel at your motivation and energy, and I'm truly grateful for how much of it has been directed my way. This PhD could only have happened with your help.

I am very fortunate to have had Clive D'Souza and Doug Noll serve on my committee. Clive's honest advice early on has shaped the trajectory of my work, and his course on human variability has been the most informative and enjoyable of all that I've taken. Doug has, on multiple occasions, won my "favorite committee member" award. He understands what's needed to help you and is quickest to offer it. Each time we've met I've left feeling encouraged, motivated, and reassured.

I would also like to thank the people from the multiple UM institutions (Surgery, Engineering, Biomedical Engineering, Rackham, International Center) who helped in all the steps related to applying, enrolling, navigating visas, navigating greencards, securing funding, actually attending, and (fingers crossed) graduating. Here in particular Maria Steele has always been on the ball.

I would like to thank everyone at ICAM, and in particular the ICAM morphomics processing team whose diligence even in the face of perpetually-beta software lets the whole group improve and expand their research. Special thanks go to Brianna Henderson, Lucy Hully, Pat Rabban, Brian Ross, and Rebecca Goulson for their work processing ribs and spines that has made this study possible. Special thanks also to Nick and Binu who understand what it takes to even get to perpetually-beta in the first place! To Ejima-san: your friendship and mentorship in Japan is what started my career. It makes me happy to see you and Kyoko and Rika enjoying life here too.

To June Sullivan and Brian Derstine: Thank you for everything you do. It has definitely improved this thesis and life is significantly easier and better with you around ($p < 0.05$). And to Joel for the outings in spherical Newtonian dynamics. Your golf score is always improving ($p > 0.05$).

To Matt Kindig: You've been amazingly generous with your time, insight, data, and oftentimes counseling. I always enjoy our discussions and they've helped focus large chunks of this thesis (which, as you know, is very much prompted from your own work anyway). It's a pleasure to talk with someone else who enjoys making the tools to study these biomechanics questions ~~more than~~ just as much as answering the questions themselves.

To Jacobo Antona: Mate, not much needs to be said. Let's add "PhD" to the aspects of life where we seem to share experiences and an uncanny understanding. Huateng and I always look forward to catching up with you and Eri (and now added extras). Thanks for being a great friend.

I've learned that the best way to build a support team in a new city is to start with a sports team. Mark, Dave, Dan, Patrick, Steve, Andy, Bill, Craig, Eric, Spencer, Yaacov, Casey, and everyone from the soccer and tennis groups: cheers all!

Last and most, to Huateng: You're amazing and I love you. Thank you for always making days better and I'm so excited to start this next chapter with you and meet our xiao-xiao.

TABLE OF CONTENTS

LIST OF FIGURES

Figure

LIST OF TABLES

Table

LIST OF SYMBOLS

A Person age

H Person height

S Person sex

W Person weight

x Axis of rib coordinate system directed from proximal to distal rib ends

y Axis of rib coordinate system directed towards lateral aspect of rib

z Out-of plane axis of rib coordinate system

3D Three-dimensional

2D Two-dimensional

Rib shape parameters and measures

S_x Rib end-to-end size or span parameter

X_{Pk} Rib peak coordinate (X) parameter, describes rib skewness

Y_{Pk} Rib peak coordinate (Y) parameter, describes aspect ratio

B_d Distal spiral shape parameter

B_p Proximal spiral shape parameter

ϕ_{pia} Proximal inner angle rib parameter

ϕ_{dia} Distal inner angle

κ_{dist} Rib curvature at the distal rib end

κ_{post} Rib curvature at the posteriorly-extending region

L_{3d} 3-dimensional rib centroidal arc length

L_{2d} In-plane rib centroidal arc length

Z_A Rib out-of-plane deviation first Bezier parameter

Z_B Rib out-of-plane deviation second Bezier parameter

ℓ Positional coordinate along rib length from proximal to distal end

Finite element model constants and outcomes

ν Poisson's Ratio

ρ Material density

E Young's Modulus

K_{ax} Rib stiffness under axial loading

K_{axCon} Rib stiffness under constrained axial loading

K_{lat} Rib stiffness under lateral loading

K_{latCon} Rib stiffness under constrained lateral loading

Thorax and body parameters and measures

α_{PH} Rib pump-handle angle

α_{LS} Rib lateral swing angle

α_{BH} Rib bucket-handle angle

$RIBOFF_{[x|y|z]}$ Offset from spinal canal to rib in x, y, z

$L5_{pitch}$ Orientation (pitch) angle of the L5 vertebra

$VBSEG_{\alpha}$ Vertebral segment angle with respect to its inferior neighbor

$VBSEG_{Sz}$ Vertebral segment height

$STNOTCH_{[x|y|z]}$ Position of rib notches on sternum in local x, y, z

$STNM_{[y|z]Offset}$ Offset of sternum plane origin from midpoint of 2nd rib distal ends

$STNM_{pitch}$ Orientation (pitch) angle of the sternum

LIST OF ACRONYMS

AIS	Abbreviated Injury Scale.
ATD	Anthropomorphic Test Device.
BMI	Body Mass Index.
CPR	Cardiopulmonary Resuscitation.
CT	Computed Tomography.
CTI	Combined Thoracic Index.
FE	Finite Element.
GHBMC	Global Human Body Models Consortium.
GM	General Motors.
GPA	Generalized Procrustes Analysis.
ICAM	International Center for Automotive Medicine.
MAE	Mean Absolute Error.
MSE	Mean Squared Error.
MVC	Motor Vehicle Crash.
NHTSA	National Highway Traffic Safety Administration.
PCA	Principal Component Analysis.
PMHS	Post-mortem Human Surrogate.
SAE	Society of Automotive Engineers.
SRF	Surgical Rib Fixation.
THUMS	Total Human Model for Safety.

ABSTRACT

The development of population-wide descriptions of human rib and rib cage geometry

by

Sven Alan Holcombe

Co-Chairs: Professor James B. Grotberg, Professor Stewart C. Wang

Elderly individuals, obese individuals, and females all have greater risk of rib fractures and other associated thoracic injuries than younger mid-sized male adults in motor vehicle crashes. Differences in body morphology between these vulnerable populations and the subjects represented by physical or computational human body models is a potential source for this risk disparity, and efforts are required to quantify these differences in order to protect a wider population.

We present a novel parametric shape model of the human rib centroidal path using logarithmic spirals. It provides a more accurate and efficient fit than previous models of overall rib geometry, and it utilizes direct geometric properties such rib size, aspect ratio, and "skewness" in its parameterization.

The model was fitted to $21{,}124$ ribs from 1000 adult CT scans, and regression analyses produced a flexible rib shape model to build ribs typical for any population of a given age, height, weight, and sex. Significant differences in rib shape were quantified across populations, and a new aging effect was uncovered whereby rib span and rib aspect ratio are seen to increase with age, producing characteristically shallower and flatter overall

rib shapes in elderly populations. This effect was more strongly and directly associated with age than previously documented age-related changes in rib angulation. Simulated mechanical loading of ribs showed that the specific changes in shape found with age also had implications on their ability to resist deformation. Stiffness to body-anterior loading was seen to increase with age by up to 30% across a 70-year age difference.

Finally, we place ribs into their appropriate thoracic context by building a similar parametric model of the surrounding skeleton. A modular approach is used that ensures accuracy in key geometric measures, and results show the accumulated effects on overall chest shape that come from individual variations in the ribs, spine, sternum, and their relative positions.

This study can be used to help build population-specific computational models of the thoracic rib cage. Furthermore, results provide quantitative population corridors for rib shape parameters which can be used to improve the assessment and treatment of rib skeletal deformity and disease.

CHAPTER 1

Introduction

1.1 Epidemiology and vulnerable populations

Motor vehicle crashes (MVCs) are a leading cause of injury and mortality worldwide. Approximately 33,000 people die every year in the United States in MVCs, with even higher rates prior to 2010 (National Highway Traffic Safety Administration, 2014). MVCs are a significant problem when they involve elderly occupants (Zhou et al., 1996; Holcomb et al., 2003; Ridella et al., 2012), and shifts in most countries' demographics show that we, as a population, are aging. The proportion of the population aged 65 and older is projected to make up 20 % of the US population by 2030 (Ortman et al., 2014) and 26 % of the population in developed countries by the year 2050 (United Nations, 2015). An aging population comes with associated increases in the total number of older road users, with 37 million licensed drivers over 65 in the US in 2013, an increase of 37 % from 1999 (Federal Highway Administration, 2015a,b). Preusser et al. (1998) showed that drivers aged 65–69 years were 1.29 times more at risk of being involved in fatal crashes and drivers aged 85 and older were 3.74 times more at risk when compared to drivers aged 40–49.

Obesity rates have also risen substantially since the 1980s in the US and other countries, and in 2009–2010 more than one-third of US adults were categorized as obese (Ogden et al., 2012; Finucane et al., 2011; Shields et al., 2011). Rice and Zhu (2014) found that obese vehicle drivers are more likely to die from MVCs than non-obese occupants involved in

the same collision. Fatality risk increased with increasing Body Mass Index (BMI), with a 1.21 times greater risk at BMI 30–35 than normal BMI (18.5–24.9), and a 1.80 times greater risk at BMI 40+. That same study also found that fatality risk was slightly raised for underweight drivers as compared to normal weight drivers, and that BMI effects varied by gender (Rice and Zhu, 2014). Injury risk is seen to increase with obesity, where front-seat occupants of MVCs with BMI 30–35 had over 54 % higher risk of injury than an occupant with a BMI of 22 (Viano et al., 2008). Ma et al. (2011) similarly found increased injury risk with obesity in non-fatal MVCs and showed that this association was much stronger for obese male drivers than female drivers.

There is also a gender difference in overall crash patterns and injury outcomes. Traffic safety data shows that driving exposure is higher for males than females, with 33 % more annual vehicle miles traveled per male driver (FHA, 2010). However, this difference in exposure is narrowing (Romano et al., 2008; Pulido et al., 2016), and when considering the relative density of incidence, there is a higher proportion of injurious crashes per million vehicle miles traveled for female compared to male drivers (DOT, 2008). Overall this leads to a greater relative injury risk for females (Parenteau et al., 2013), and Bose et al. (2011) showed that the odds for a belt-restrained female driver to sustain severe injuries were 47 % higher than those for a similarly restrained male driver involved in a comparable crash.

When considering MVC fatalities as a whole, over 70 % occur in frontal impacts (Morris et al., 2003). In such crash configurations the body is generally loaded through the chest or thorax, and the crash safety community places continued effort on developing advanced restraint systems that can mitigate or manage that load. In frontal impacts, age is associated with an increased risk of injury to all body regions; however, the most pronounced age effect is seen in the risk of injury to the thorax (Kent et al., 2005a, 2008; Morris et al., 2003; Lee et al., 2006). A gender effect exists in frontal impacts also, with older females in particular more likely to have thoracic injuries than older males (Carter et al., 2014; Ridella et al., 2012). Furthermore, obese occupants are at increased risk of thoracic injuries in

frontal impacts compared to non-obese occupants (Cormier, 2008).

Rib fractures are the most common form of severe chest injury in frontal crashes – they occur in over $90\,\%$ of fatalities to belted occupants – and the risk of mortality goes up as the number of ribs fractured increases (Arajärvi and Santavirta, 1989; Abdulrahman et al., 2013; Holcomb et al., 2003; Bulger et al., 2000). Consistent with chest injuries as a whole, rib fractures show higher incidence rates in the elderly over younger occupants (Lee et al., 2006; Ridella et al., 2012). Once sustained, rib fractures can cause a number of physiological complications including pain, reduced vital capacity, and a decreased ability to clear secretions, and rib fractures are often associated with pulmonary contusions causing further and significant respiratory distress (Livingston and Hauser, 2004). Rib fractures are particularly problematic for the elderly, who tend to experience poorer outcomes when sustaining them, including longer hospital stays, longer periods on ventilation, increased risk of pneumonia, increased risk of mortality, and a greater overall economic burden (Bulger et al., 2000; Lee et al., 2006; Holcomb et al., 2003; Bergeron et al., 2003).

Motor vehicle safety as a whole has improved dramatically over time due to innovations in vehicle systems, restraint technologies, policy changes, and driver education. However, in the adult population, the elderly, the obese, and females are groups that are vulnerable to death or injury – involving the thorax and ribs in particular – and this vulnerability occurs in some of the most prevalent crash configurations. We, as a safety community, have an opportunity to make new gains in occupant protection by specifically identifying and addressing safety concerns for those populations most at risk. In this thesis we will investigate the variability in rib shape and mechanics from broadly sampled subjects who are inclusive of these vulnerable populations. In doing so we can better understand the reasons behind their increased thoracic injury risk in MVCs, and also gain insight for potential remedies.

1.1.1 The rib cage in clinical applications

1.1.1.1 The rib cage in CPR

Rib fractures are also a concern in areas outside of motor vehicle safety. Rib fractures are common during cardiopulmonary resuscitation (CPR), with a review by Hoke and Chamberlain (2004) showing that reported rib fracture rates during CPR varied between 13–97 % across a number of studies with differing detection methodologies. A recent study reported fractures occurring during CPR at rates of 77 % and 85 % for males and females, respectively (Kralj et al., 2015). Furthermore, a 2004 study showed most fractures associated with CPR were left undetected and unreported using conventional X-ray investigations (Lederer et al., 2004), suggesting that the prevalence of rib fractures after CPR may be higher than previously thought. While it is true that rib fractures themselves are a relatively low concern when CPR is being administered, it should be noted that their presence can still cause complications and prolong recovery times. As such, a better understanding of the mechanics of ribs under loading – and how to best avoid fractures during compression – has the potential to improve outcomes from interventions like CPR.

1.1.1.2 Rib shape in device design

When left untreated, poorly healed fractured ribs can lead to chronic pain, disability, and deformity (Gordy et al., 2014). Surgical rib fixation (SRF) is a treatment modality whereby a rib fixation system, usually titanium, is connected to fractured ribs either through screws or clips so as to stabilize and support the fractured region. SRF is becoming increasingly accepted and has been shown in flail chest patients to reduce ventilator times, intensive care stay, and costs of treatment (Tanaka et al., 2002; Granetzny et al., 2005; Marasco et al., 2013). SRF, however, has still not become standard of care, due in part to a lack of appropriate devices, leading to the use of alternative fixations that are associated with hardware failures (Marasco et al., 2010; Marasco and Saxena, 2015). Many of the devices

used in SRF come pre-contoured, however further contouring is often required to better match the rib, and with any device a small amount of spring-back is expected (Marasco and Saxena, 2015). It would be in the best interests of patients, doctors, and device manufacturers to optimize this fit between device and rib cage in advance, which would reduce overall surgery lengths and improve patient outcomes.

1.2 Background on thoracic anatomy

Before investigating rib cage and rib anatomy in detail, we will start with an overview of the human thorax and the role of the rib cage within it. We will also introduce some terminology that will be used throughout this thesis.

The thorax sits in the superior portion of the human trunk above the abdomen. It contains the chest which, broadly speaking, can be compartmentalized from the superficial aspect to the deep aspect into three layers:

Skin and subcutaneous layer contains the skin, subcutaneous fat, and some superficial musculature such as the pectoral muscles and paraspinous muscles.

Thoracic wall (or chest wall) includes the spine, the ribs, the sternum, costal cartilage, and intercostal musculature.

Thoracic cavity includes the pulmonary cavity, and contains vital organs such as the heart, the lungs, and major blood vessels.

This thesis will deal primarily with the skeletal components of the thoracic wall which, together, form the rib cage.

1.2.1 The thoracic rib cage

The primary function of the rib cage is to provide protection to the heart, lungs, and other thoracic organs (Gray, 1918). Additionally, major upper abdominal organs such as

the liver and the spleen are protected by the rib cage, despite sitting below the diaphragm and in the abdominal cavity.

The rib cage contains twelve left and right pairs or levels of ribs, and the ribs are counted from 1st (superior-most) to 12th (inferior-most). Ribs can be further distinguished as true ribs, false ribs, and floating ribs (Figure 1.1). The true ribs (levels 1 to 7) each have a direct connection to the sternum through a segment of costal cartilage. The false ribs (levels 8 to 10) are only indirectly connected to the sternum, with their segment of costal cartilage attaching to one or more ribs above. Finally, the floating ribs (11th and 12th) have no cartilage connection to the sternum, instead ending in the abdominal musculature, and are generally shorter and oriented more laterally than their superior neighbors.

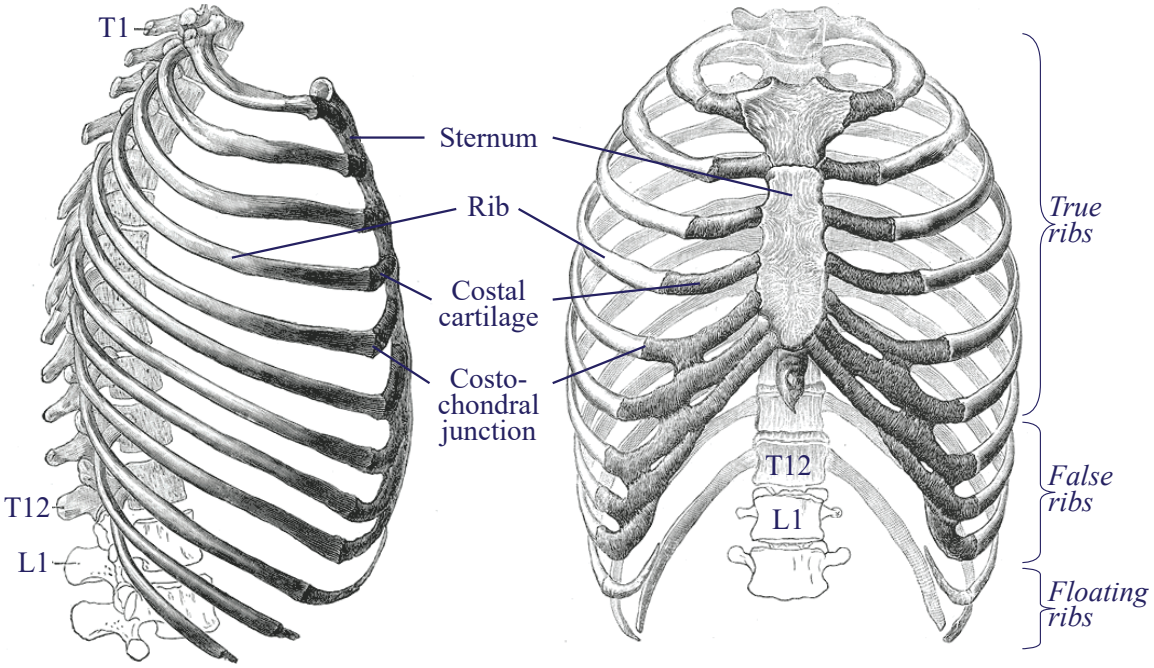

Figure 1.1: Anatomy of the rib cage from lateral and anterior views (Gray 1918).

The ribs are connected to their adjacent neighbors via three layers of intercostal musculature (Huelke, 1976), as well as thin but tough membraneous layers of connective tissue that lines the chest wall on the superficial (external intercostal membrane) and deep (endothoracic fascia and parietal pleura) sides. All of the twelve ribs articulate with the thoracic vertebrae of the spine, and these vertebrae are labeled with equivalent numbers to

the ribs. For example, the 7th ribs articulate primarily with the T7 vertebra at that vertebra's body and transverse process. However, they do additionally articulate with the body of the vertebra above, see below.

Some degree of variation from the standard rib topology is seen, with some individuals having fewer (11) or more (13) rib levels. This is usually in the form of extra floating ribs at what would be the L1 vertebra, but some individuals may instead have an extra thoracic vertebra with an accompanying pair of true or false ribs. Another atypical rib pattern includes bifurcation of one or more ribs, often accompanied by additional costal segments attaching each rib end to the sternum. Throughout this thesis we will generally deal with subjects having a standard rib topology.

1.2.2 The rib

Ribs within the rib cage vary in size and shape; however, there are several geometric features that are shared between rib levels. An overview of those features that are typical of an isolated rib is provided in Figure 1.2. The end closest to the spine is called the *head* of the rib, which articulates with the demifacet (a small indentation) of the thoracic vertebra with matching vertebral number (e.g., 7th rib articulates with T7, the 7th thoracic vertebra) and one vertebra superior (e.g., 7th rib also articulates with T6). Together this joint between a rib and two vertebrae is called the *costovertebral joint*. Each rib also articulates at its *tubercle* process with the transverse process of its same-numbered vertebra at the *costotransverse joint*.

Between the head and the tubercle lies the *neck* of the rib: a short section that is straighter than other regions of the rib. Beyond the tubercle is the rib *shaft* (also known as the rib *body* or *diaphysis*), which provides the rib's typical sweeping arc-like shape and makes up the majority of the rib's length. One main prominence is visible beyond the tubercle, and that is the rib *angle* which forms a line on the superficial side at the attachment site for the iliocostalis tendon. On the deep side, the shaft forms a continuous smooth surface,

which helps accommodate sliding movement of the lungs during respiration. Each rib has its own innervation and blood supply (the *intercostal neurovascular bundle*), which runs along the inferior boundary on the inner surface of the rib in a valley known as the *costal groove*. This groove is most prominent in mid-level ribs and at lateral regions from the rib angle and towards the middle of the shaft.

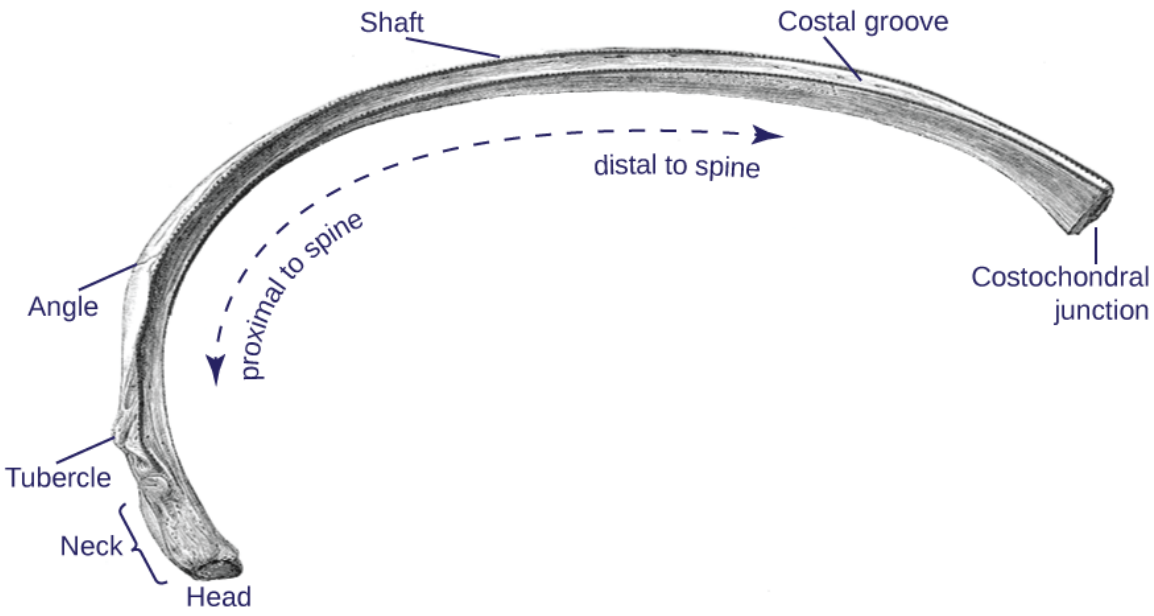

Figure 1.2: Overview of anatomic features of the human rib, shown from an inferior view (Gray, 1918). The head and tubercle articulate with the spine, while the costochondral junction interfaces with costal cartilage.

Due to the variation across the rib cage, confusion can arise from terminology used to describe the two opposite ends of a rib. This occurs because terminology that is applicable to some rib levels might not be both clear and consistent across all rib levels. Referring to "anterior" or "posterior" rib ends is problematic since lower ribs actually extend more laterally than anteriorly. Using "vertebral" and "sternal" terminology has the caveat that lower, floating ribs also do not extend towards the sternum. Here, we will use the anatomical terminology of "proximal" and "distal", with the intention in both cases to refer to ends of the ribs *proximal to the spine* or *distal to the spine*. Thus when referring to a direction along the rib, the terms *proximal* and *distal* will be used throughout this text, and we will occasionally append "to the spine" as a reminder for the reader.

Rib bone material is typical of many long bones in the body, being composed of mineralized Type I collagen fibers and inorganic hydroxyapatite. It consists of a harder outer *cortical* shell and an inner *trabecular* matrix of a network of collagen struts. Bone marrow is stored in a medular cavity inside the trabecular region, covered by the *endosteum* connective tissue layer. Superficially, another membrane-like layer called the *periosteum* surrounds the cortex itself.

To provide context for the variation in size and shape seen throughout the rib cage, Figure 1.3 gives an arrangement of all isolated ribs shown to an equivalent scale. Here it can be seen that the first rib is unique in being the smallest and also having a substantially wider and flatter cross-section than other ribs, as well as a more pronounced tubercle prominence. The 2nd through 7th ribs have a more traditional appearance, and then ribs become longer and less curved as they progress downwards (Saladin, 2009).

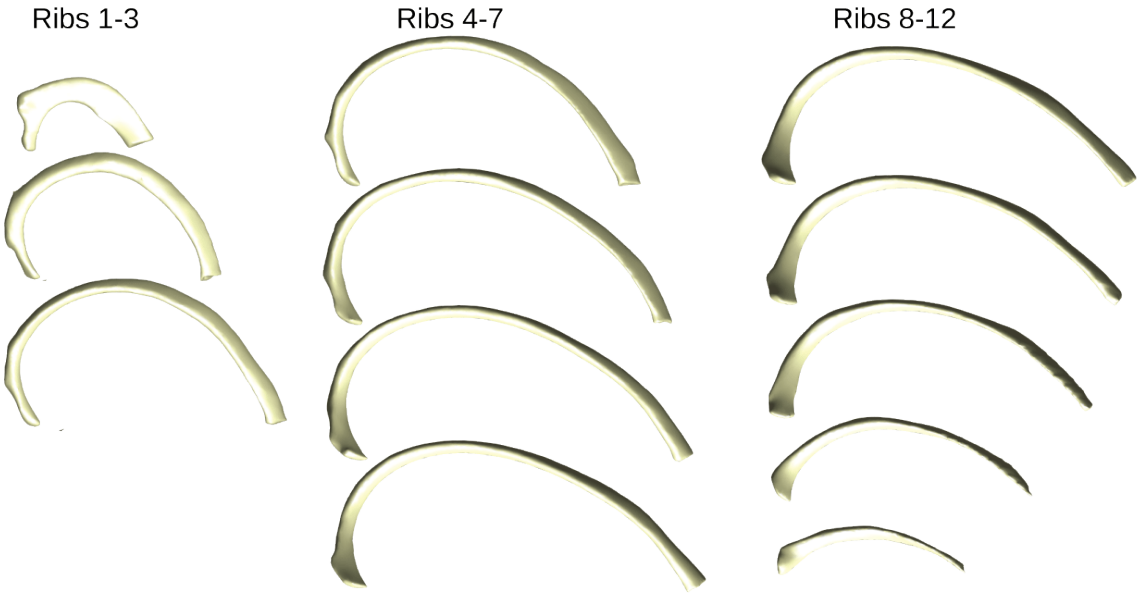

Figure 1.3: Comparative shape and size of all rib levels.

1.2.3 The local rib coordinate system

Here we will introduce a local rib coordinate system similar to that used in a number of past studies (Kindig and Kent, 2013; Holcombe et al., 2013). Figure 1.4 shows the position and orientation of this coordinate system within the rib cage, and Figure 1.5 shows reoriented views of a single rib fitted to its local plane. The origin of this coordinate system is located at the center of the proximal (to the spine) end of the rib. The plane's x-axis extends from this origin and intersects the center of the distal end of the rib at the costo-chondral junction. The y-axis is then chosen so as to minimize the out-of-plane distance of a series of equally spaced points placed at the center of cross-sections along the length of the rib. For instance, Figure 1.5 shows the proximal section of the rib diving below the x-y local plane (negative z-coordinates), and the distal section of the rib rising above it (positive z-coordinates). The exact orientation of the y-axis has been computed such that the sum total of z-coordinates from points along the center of the rib is zero.

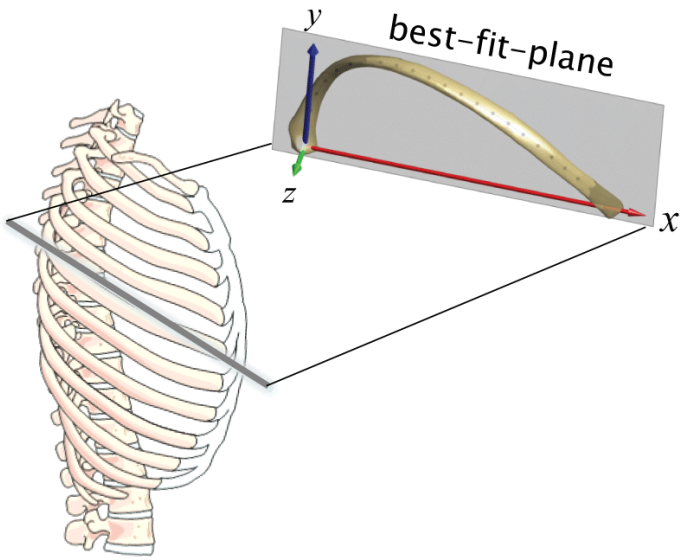

Figure 1.4: Sagittal view of the rib cage and rib plane showing plane orientation. The local rib x-axis extends through the proximal and distal rib ends, and the rib plane is chosen to minimize out-of-plane deviation of points distributed along the rib.

The orientation of this rib plane within the body provides important measures of rib angulation (see Chapter 3). However, within the in-plane view of a single rib, we can also

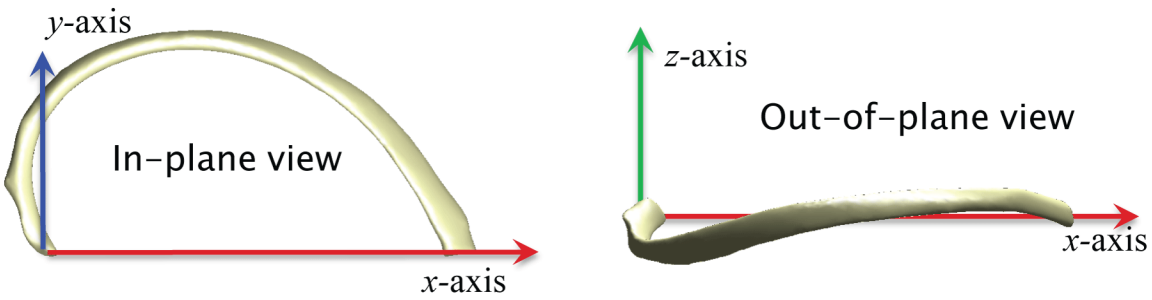

Figure 1.5: In-plane view and out-of-plane view of a single rib.

define some intrinsic geometric characteristics for size and shape. Firstly, the *rib size* or *rib span* is given by the linear distance between proximal and distal rib ends, referred to in this thesis by the parameter S_x. Next, we can specifically label the *rib peak* as the position on the rib (at its cross-sectional centroid) furthest perpendicularly from the x-axis as shown in Figure 1.6. The local x- and y- coordinates of the rib peak then define the rib *aspect ratio* and rib *skewness*. The *aspect ratio* is given by the height (y-coordinate) of the rib peak divided by the rib span S_x, and the *skewness* is given by the relative x-coordinate of the rib peak and S_x. The aspect ratio increases as the rib peak moves closer to the x-axis, and the skewness of a rib increases as the peak shifts towards the local y-axis. These concepts and other intrinsic properties of a rib's geometry will be explored in greater depth in Chapters 2 and 3.

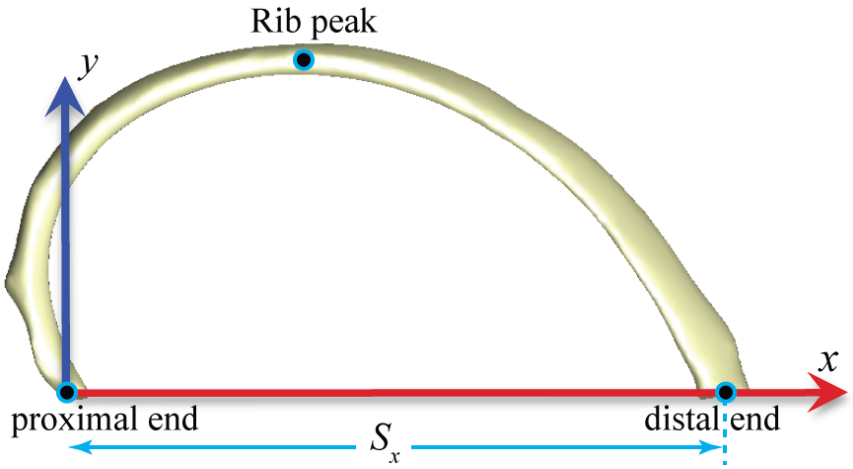

Figure 1.6: In-plane view showing rib size represented by the span from the proximal end to distal end (S_x), and the rib peak position.

1.3 Physical models and ATDs

A ubiquitous tool in motor vehicle safety over the last 30 years has been the anthropomorphic test device (ATD), colloquially termed the crash test dummy. ATDs allow engineers to test vehicles and safety devices under controlled conditions, and to assess whether the forces experienced by the ATD would correspond to injurious conditions for an occupant. As such, ATDs are designed so that their physical response to loading meets corridors that are derived from multiple sources of biomechanical data. When considering thoracic biomechanics, physical models have been primarily used including volunteers (subjected to non-injurious loads), post-mortem human surrogate (PMHS), and animals.

In the 1970s a landmark set of experiments were performed at the General Motors (GM) Research Laboratories, published through a number of studies from Kroell et al. (1971; 1974; 1976), Nahum et al. (1971), Neathery (1974; 1975), and others. These tests were performed on unrestrained PMHS subjects who were subjected to thoracic hub-loading, and their results set the template for biofidelity corridors used to benchmark ATDs. In fact, the National Highway Traffic Safety Administration (NHTSA) standard for occupant protection (FMVS) 208) had originally specified only the type of occupant restraints (i.e., seat belts) required by new vehicles. In 1983, however, GM successfully petitioned NHTSA to allow the use of the Hybrid III mid-size adult male dummy as an alternate device for compliance testing of frontal impact passive restraint systems, based largely on the results and analysis from this prior thoracic testing (Mertz et al., 2003).

Follow-up PMHS studies have added restraints to their experimental setup to investigate the thoracic response to airbag-type distributed loading (Yoganandan et al., 1993; Morgan et al., 1994; Trosseille et al., 2008) and to shoulder-type diagonal belt loading Morgan et al. (1994); Cesari and Bouquet (1994). Tests examining the thoracic response under multiple loading directions have also been performed, representative of loading applied to the body from a lateral direction (Stalnaker et al., 1979; Marcus et al., 1983; Viano et al., 1989; Cavanaugh et al., 1993) and loading from oblique directions (Kent et al., 2003a; Shaw

et al., 2006).

1.3.1 Chest injury criteria

Developed by the Association for the Advancement of Automotive Medicine, the Abbreviated Injury Scale (AIS) is classification scheme for injuries and their severity. It contains a large listing of injuries to all parts of the body, each with an associated severity: 0 (no injury), 1 (minor), 2 (moderate), 3 (serious), 4 (severe), 5 (critical), and 6 (maximal - currently untreatable) (Gennarelli et al., 2008). When considering rib fractures, the number and configuration of fractures determines AIS severity, where a serious AIS 3+ injury involves fracture of at least 3 separate ribs on one side of the body, while a severe AIS 4+ injury involves at least 5 ribs (or 3 bilaterally) including a "flail" rib having two fracture locations. Flail ribs involve a free-floating rib segment between fractures, causing a particularly unstable chest wall and leading to severe breathing difficulties.

ATDs alone do not provide counts of rib fractures under impact; instead they output direct measures of physical stimuli such as forces, displacements, and accelerations at different locations in the thorax. Researchers have used the AIS system in combination with results from the PMHS and other physical tests described above to develop specific injury criteria from the measurements taken by ATDs under similar loading. From the earliest such efforts to predict thoracic AIS (Kroell et al., 1974), measures that included sternal or chest deflection have consistently shown best correlation with injury severity (Neathery et al., 1975; Melvin et al., 1975; Morgan et al., 1994; Eppinger, 1989; Kent et al., 2001). The current vehicle safety standards use the Combined Thoracic Index (CTI) (Eppinger, 1989), which takes into account both deformation and acceleration of the chest measured anteriorly at the sternum. A critical chest deflection of $63\,\mathrm{mm}$ represents a $33\,\%$ chance of an AIS 3+ injury in a mid-sized male, with this value scaled by relative chest depth when smaller or larger ATDs are used.

It is clear that deflection of the chest, either at the sternum or measured in other areas

of the ribs, is strongly associated with the risk of injury. One factor that is not directly addressed by ATDs, however, is that the ability of the body to withstand such deformation has also shown a strong age effect (Kent and Patrie, 2005; Zhou et al., 1996). Specifically, a 30-year-old subjected to $35\,\%$ chest deflection had a $50\,\%$ risk of rib fracture, while that same risk in a 70-year-old was seen after just $13\,\%$ deflection, indicating a wide range in the tolerance to loading across the age spectrum.

1.3.2 Isolated rib testing

Biomechanical testing of the thorax can be performed at multiple scales from full bodies through micro-analysis of bone tissue. ATDs are at the global end of this spectrum and provide measures such as chest deflection as an indicator of potential rib fractures, whereas the fractures themselves occur in the body at the microstructure level. Between these levels, a number of studies have looked at ribs in isolation – as excised from PMHS subjects – to help understand their biomechanical response to loading. Charpail et al. (2005) established a testing framework that simulated the type of anterior-posterior loading seen in frontal impacts. They used 4^{th} to 9^{th} ribs and applied dynamic loading to the distal end in the rib's major plane via a pendulum impactor, and failure force and displacement (giving rib stiffness), as well as rupture energy were reported. A similar experimental setup was used by Daegling et al. (2008) who loaded eight adult ribs (of unspecified subjects and levels) to failure in order to understand strain and fracture patterns for informing forensic analyses. Kindig et al. (2011) tested 2^{nd} to 10^{th} ribs from three subjects, reporting strain histories and average differences in stiffness and mechanical response by rib level, with 2^{nd} ribs being 3 to 4 times stiffer than other levels. Agnew et al. (2015) was the first to assess population trends in isolated rib testing. They applied dynamic loading using an impactor to 140 ribs from 70 individuals across a full age spectrum including children. Results for these isolated rib tests showed a significant decrease in rib stiffness with age (at around $0.33\,\mathrm{N/mm}$ per decade), as well as a decrease in the displacement that ribs underwent before fracture.

1.4 Computational models of the human body

Motor vehicle crash safety is transitioning from solely physical test devices (ATDs) to greater use of computational human body models for impact and injury simulation. These models are largely based on the internal anatomy of selected individuals, usually chosen to represent the average external anatomy of a demographic such as the 50^{th} percentile Male (M50). Over the last 20 years a large collection of finite element (FE) models representing a mid-sized M50 male have been produced including the LAB/CEESAR model (Lizee et al., 1998), the GM model (Deng et al., 1999), the Human Model for Safety (HUMOS) (Robin, 2001; Vezin and Verriest, 2005), the H-model (Choi et al., 1999; Haug et al., 2004), the Takata model (Zhao and Narwani, 2005), the Ford model (Ruan et al., 2003, 2005), the THUMS model (Iwamoto et al., 2002), the Global Human Body Models Consortium (GHBMC) model, and a Chinese 50^{th} percentile male model (Cai et al., 2013, 2015). Notably, the Total Human Model for Safety (THUMS) and GHBMC now include accompanying models for a small female (F05) and large male (M95) in addition to their M50 baseline model, and they have produced or plan to produce models of children of varying ages. Notable still in this group, however, is that females, when represented, are represented only by models for a small-statured individual (F05), obese individuals are not well represented (the M95 models are not obese; having BMI of approximately 28 they are classified as overweight), and the concept of age (i.e., an elderly model or a young model) is not represented within this base group.

A recent review of computational models (Hu and Reed, 2012) identifies a current need for a more diverse modeling approach whereby at-risk or vulnerable populations are specifically included in modeling efforts. In the review and elsewhere, elderly occupants, female occupants, obese occupants, and children are all identified as having greater risk of injury in particular body regions. As introduced above, aging increases the risk of injury to every body-region, with thorax injury risk showing the most pronounced age effect in frontal impacts. The rib cage is of primary structural importance in frontal impacts as it interacts

with multiple safety systems (seatbelt, airbag), and a disproportionately high number of rib fractures are seen in elderly occupants.

Three broad categorizations of the factors affecting injury risk can be made (Kent et al., 2005b):

- geometric characteristics of the body including size, shape, and orientation of bones
- compositional characteristics such as cross-sectional areas of the cortical bones and soft tissues
- material characteristics of the tissues themselves including elastic or viscoelastic properties, failure strengths, and volumetric behavior

A major milestone in computational biomechanics would be a human model, suite of models, or indeed a flexible modeling system, that provided engineers with a tool that incorporated each of the factors above in order to represent a biofidelic thoracic response for any chosen demographic. While this goal has not yet been reached, a number of studies have contributed to the body of knowledge required to build such a tool. This thesis will focus on the first point above – the geometric characteristics of the body – and in particular address the geometric variation in the ribs and rib cage that occurs across populations.

1.4.1 Rib and rib cage characterization

Most of the full-sized human body FE models from above have been developed based on the internal geometry of a single representative individual scanned on a one-off basis. There have also been a number of studies aimed at characterizing parts of thoracic anatomy in a quantitative fashion that could, when applied over a large population, be used to investigate variation in thoracic geometry on a population scale. These efforts to quantify rib and rib cage shape have followed one of two general methodologies. The first takes landmarks placed strategically across the rib cage from a series of individuals, then uses a combination of Generalized Procrustes Analysis (GPA) and Principal Component Analysis (PCA)

to quantify changes in those landmarks across populations. Gayzik et al. (2008) used GPA to analyze 106 landmarks from 63 adult male rib cages (Slice and Stitzel, 2004; Gayzik et al., 2008) and described a rounding of the rib cage with aging. Weaver et al. (2014) used a similar technique with a more complete set of landmarks across the rib cage and applied it to a larger population including 164 adults and 175 children to quantify rib cage morphology changes as a whole, reporting increased rib angles and a rounding of the rib cage with age. Shi et al. (2014) applied GPA and PCA to 464 landmarks from 89 subjects and, along with confirmation of an increase in rib angle with age, reported an increase in rib cage depth coupled with a reduction in rib cage width. A followup to Shi et al. (2014) was published by Wang et al. (2016), who increased the subject count to 101 subjects, added thoracic spine and sternal geometry to their landmark set, and improved aspects of the normalization of subjects for use in PCA. While techniques such as GPA and PCA provide an overall quantification of the rib cage, their results usually combine the changes in bone shape with the changes in bone position and orientation. Such techniques do allow for the creation of morphing maps that, when applied to an atlas or known geometric mesh, allow for the visualization of modes of deformation to the rib cage. However, the quantification itself is in the form of a large array of landmark coefficients, and these can be difficult to interpret or use when comparing subjects outside the original group to those inside the sample population.

A second general methodology isolates the ribs themselves and characterizes their shapes using measures from geometric primitives. Examples include rib shape representations using a circular ring (Kent et al., 2001), an arc (Schultz et al., 1974), an ellipse (Margulies et al., 1989), and a pair of superimposed arcs (Roberts and Chen, 1972; Roberts, 1977). Ribs have also been represented within physical models of the larger thorax using similar geometric primitives. When developing the Society of Automotive Engineers (SAE) scaling protocol for adult ATDs, Mertz et al. (1989) simplified the elastic component of the dummy chest as a rib built from a single circular hoop. This scheme was duplicated

by Kent et al. (2001) in an analytic model of the thorax for comparing restraint conditions during chest compression. Mohr et al. (2007) measured curvature of the external surface using circles fitted to a sliding window along sections of the rib, but no mathematical model of the overall centroidal axis was used. The most recent and thorough exposition of a mathematical shape model was provided by Kindig and Kent (2013), who presented a seven-parameter model using a circle and semi-ellipse connected by short patches. The benefits and limitations of this model will be examined more closely in Chapter 2, where a new formulation using logarithmic spirals is proposed. An overall benefit of all models using this parametric approach is the potential to follow the trends in parameters as they change across populations. In terms of age effects, Holcombe et al. (2013) used the Kindig and Kent model to show the growth of ribs across childhood. However, to date, these direct models of rib shape have not been applied to large adult populations for the study of changes with age within adults, despite experimental studies of isolated ribs under loading reporting significant changes in rib stiffness and fracture onset with age (Agnew et al., 2015).

1.4.2 Understood aging effects

When describing global geometric changes of the rib cage with age, a number of studies have reported that an effect of age on the adult rib cage is to gradually increase the angle of ribs with respect to a horizontal plane over time. This understanding originated from Kent et al. (2005b) and was highlighted by a figure of two individuals' rib cages taken from a lateral view, one with more horizontally oriented ribs than the other. The same figure has been reproduced in a number of publications and presentations, often with annotated labels of "young vs. old" ribs (Figure 1.7). Subsequent studies that address rib cage changes with age have all referred to this rib angle increase and confirmed its presence to some degree (Gayzik et al., 2008; Weaver et al., 2014; Shi et al., 2014; Wang et al., 2016). This has led to the general consensus that rib angle is the primary geometric aging effect asso-

ciated with rib cage geometry. In Kent et al. (2005b) however, it is often overlooked that a multivariate analysis including predictors of age and BMI showed that BMI was the driving factor behind increased rib angle (4^o increase with only 4.8 added BMI points, $p < 0.001$) compared to age (4^o increase with 55 added years, $p = 0.018$). In fact, the original figure actually shows a young rib cage with low BMI compared to an old rib cage with high BMI, rather than simply an age comparison, as it has become known to be.

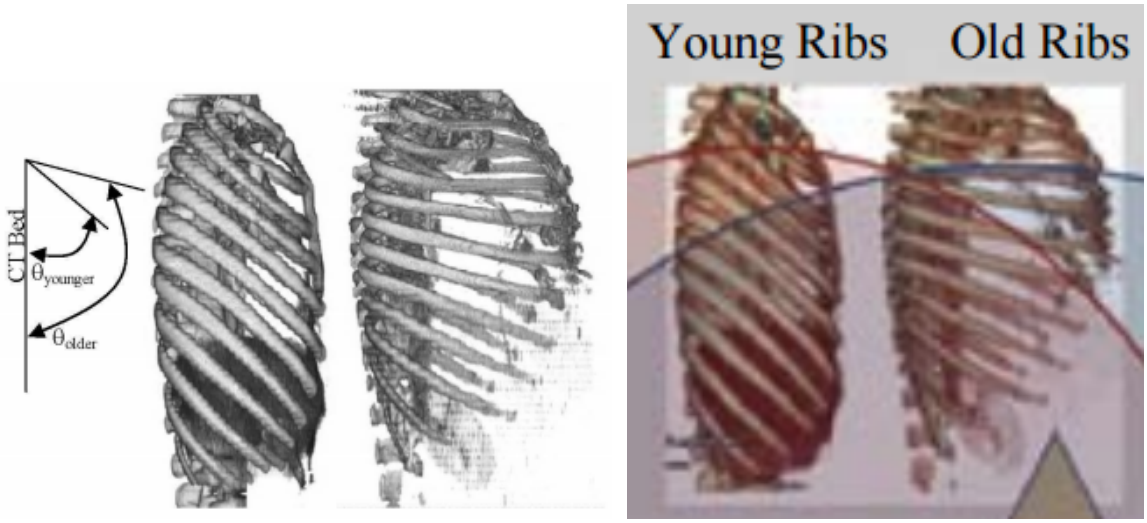

(a) Figure 4 from Kent et al. (2005b). (b) Partial Figure 1 from Hu and Reed (2012).

Figure 1.7: Prior literature has described the primary effect of age on rib shape to be increased rib angle within the chest.

1.5 CT image volumes

The primary data source for the content of this thesis will be computed tomography (CT) scan image volumes taken in a hospital setting as part of routine patient care. A typical CT scan output consists of a series of 2D radiographic slices through the body that are stacked to form a 3D volume. Pixels in slices (or voxels in image volumes) are displayed with pixel intensity representing relative radiodensity of the tissue or material in that spatial location. An exemplar axial image slice through the chest is shown in Figure 1.8. Intensities are given in Hounsfield Units (HU), which are calibrated with air at $-1000\,\mathrm{HU}$, water at

0 HU, and different density bone ranging from around 150 HU to over 1000 HU.

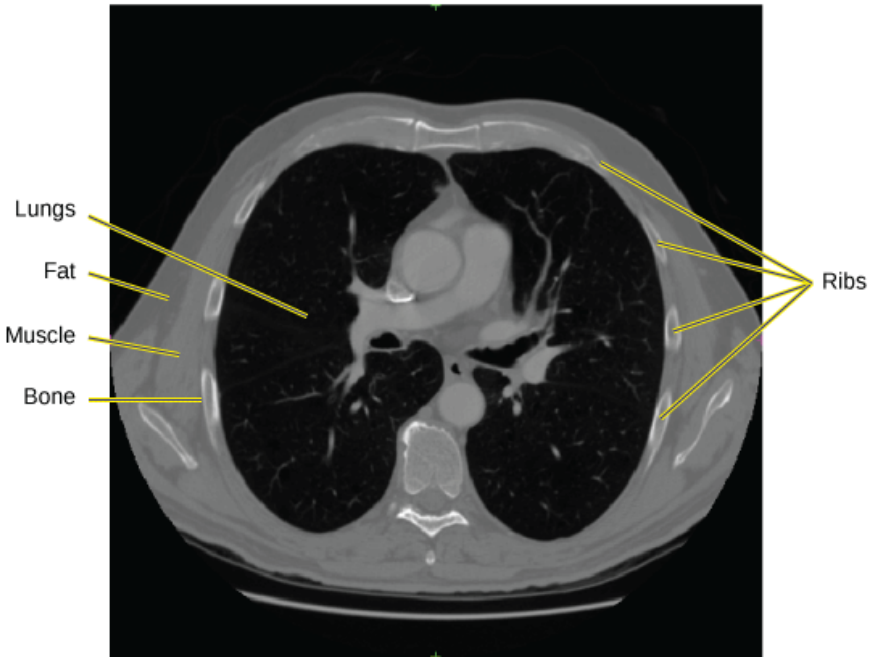

Figure 1.8: Example axial CT slice through the chest. Image intensity indicates tissue radiodensity, and ribs are seen in oblique cross-section as they pass through the axial plane.

When using medical CT images to represent human geometry, a number of factors will affect image detail and clarity, and consequently the ability to extract accurate spatial information from those images:

In-plane image resolution. Typically for abdomen/thorax scans 512-by-512 pixels are used to cover the cross-section of the body, resulting in between approximately $0.3\,\mathrm{mm/pixel}$ for infants to $1.5\,\mathrm{mm/pixel}$ for larger adults.

Slice spacing. Spacing between consecutive image slices gives the out-of-plane resolution, and is usually between $0.625\,\mathrm{mm}$ to $5\,\mathrm{mm}$.

Slice thickness. Controls the physical region aggregated when calculating pixels for a single slice with thinner slices more detailed but also with more high-frequency noise. For typical medical images, slice thickness is similar to slice spacing.

1.5.1 The ICAM morphomics and CT database

The human data to be presented in this thesis has been collected through the International Center for Automotive Medicine (ICAM) scan and morphomics database. The scan database is a collection of CT scans themselves sourced primarily from the University of Michigan or other hospital radiology archives. The scan database is part of the larger UM Morphomics System, which is designed to link 3D image volumes and body geometry of a large number of individuals to clinical data sources.

The system (with overview shown in Figure 1.9) consists of a CT image data store, a spatial geometry database with records describing the 3D geometry of bodies in the image volumes, a "morphomics" database containing a wide array of geometry and material measures from each individual, and a linkage to associated clinical and demographics information about each individual. A MATLAB application program interface (API) has been written that interfaces with the components of the morphomics system.

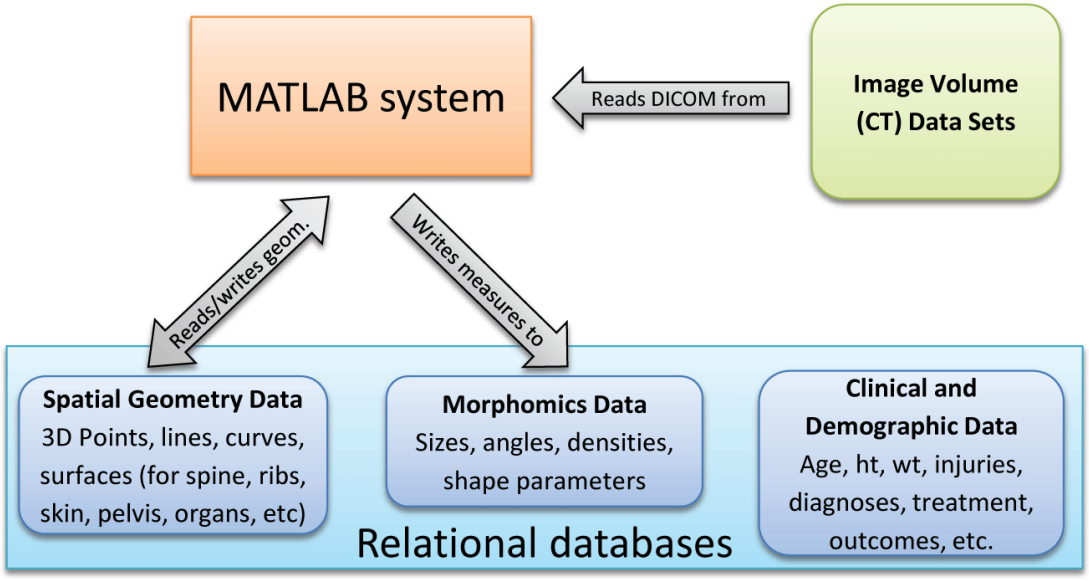

Figure 1.9: ICAM morphomics system overview.

At present the system contains image data from around 80,000 CT scans of individuals. This thesis will utilize a small subset of these scans that 1) were performed as part

of standard care for trauma, 2) covered a large enough portion of the thoracic region of interest, 3) met specific demographics criteria, and 4) have had specific processing steps performed that extract rib cage geometry in the form of 3D points and lines. Chapter 2 will expand on the resulting geometry used for rib characterization, so here we will provide a short introduction into the processing steps that are performed in order to generate this geometric data.

The spatial geometry stored for each individual consists of 3D points, lines (or curves), and triangulated surfaces relating to a variety of anatomical structures. Each geometry is stored in an equivalent coordinate system to the underlying CT image data, such that any geometric data can be directly projected onto – and displayed with – image slices from that region as depicted in Figure 1.10. Equally importantly, the connection between stored geometry and image space allows for systematic re-slicing of that image data to align with local anatomically relevant planes.

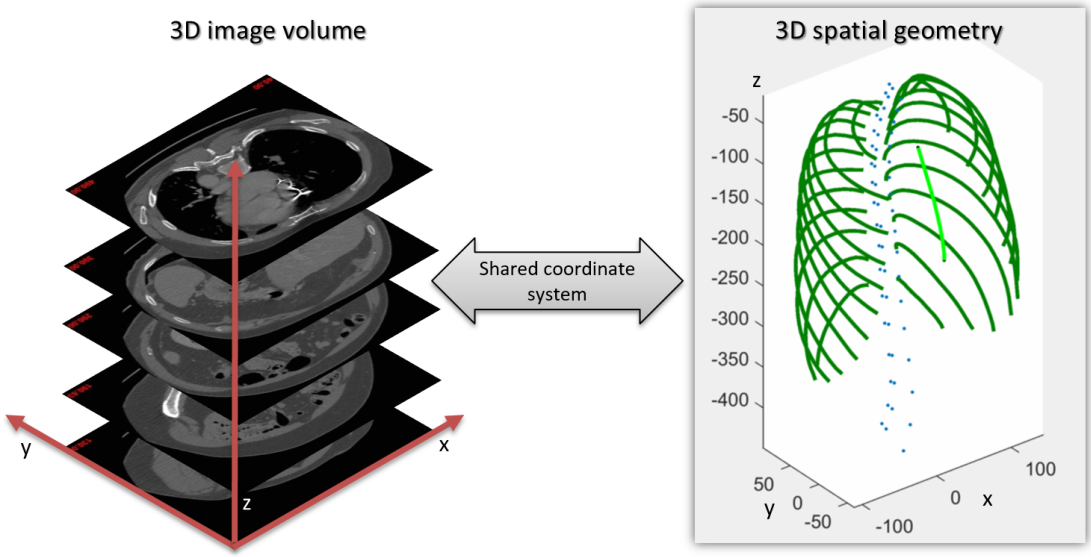

Figure 1.10: Geometry is stored in a spatial database using an equivalent coordinate system to the underlying image volume. Shown geometry includes spine landmarks (blue dots), and rib (dark green) and sternum (light green) central axis curves.

The first geometry that is placed for any scan volume is a simplified representation of the spine using named landmarks. These are placed at the center of the spinal canal in line

with the inferior end-plate of each vertebral body and allow programmatic loading of image volumes relating specifically to a known body region. For example, the presence of points along the thoracic spine (at vertebral levels of T1, T2, etc.) allows for the rapid loading of a localized region of interest around each vertebra, and, with a simple user interface, allows users to quickly and accurately place further landmarks at the proximal ends of ribs. Similarly, Figure 1.11 shows an interface that loads local scan data in the regions surrounding ribs in order to ensure that rib geometric data coincides with resliced cross-sectional views through ribs. This thesis relies on large populations of rib geometric data in order to draw conclusions regarding changes across demographics, and the efficiency with which such data can be collected from scan volumes (and do so accurately) is a significant consideration.

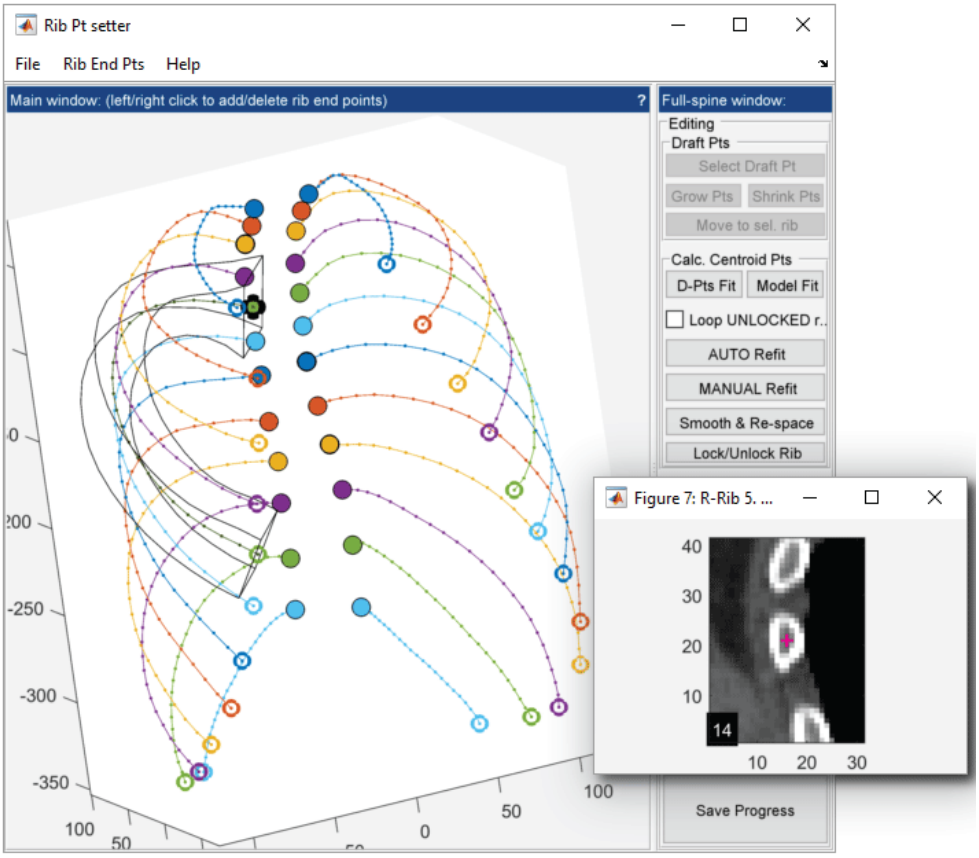

Figure 1.11: Morphomics system editor for rib centroid path geometry. Each rib's centroidal path could be manually adjusted (inset) via images resliced perpendicular to the path in the case of failure of the automatic algorithm to detect the true centroid.

1.6 Summary and goals

Understanding the shape of human ribs can aid in developing models of the thorax, and understanding the changes in that shape across populations allows us to model a wide range of individuals including those most vulnerable to thoracic injuries. The overall aim of this thesis is to investigate those changes in rib centroidal shape and to describe their effects on the biomechanical response of ribs to loading. As is seen from the previous sections, the ribs and rib cage are an important factor in thoracic injury, and a body of working knowledge has been built regarding the role of population variability in injury outcomes.

In order to analyze the shape of multiple individual ribs, a mathematical framework is first required. Chapter 2 takes on this task by presenting a novel parametric model of human rib shape that uses logarithmic spirals as its mathematical basis. The model consists of six independent parameters that include inherent and easily measured geometric properties such as size, aspect ratio, and rib "skewness". The model is compared to previous literature in terms of its accuracy, simplicity, and efficiency, as well as its behavior when aggregating a collection of individual ribs to represent group trends.

To assess overall population variability in rib geometry, Chapter 3 takes the model introduced in Chapter 2 and applies it to data from a large collection of individuals chosen so as to reflect the overall demographics of American adults. From that population, four common demographic factors in anthropometric study are considered – age, height, weight, and sex – and we track the changes in each of the shape model's parameters across those factors. A primary focus of this chapter is to identify the typical changes in rib cage anatomy that are expected as age increases, and one goal of this thesis is to explicitly test a commonly held belief that changes to thoracic rib angle is the dominant geometric effect of age and to compare this effect to other potential changes such as those related to rib shape.

The ubiquitous measure used when setting injury criteria for thoracic loading is chest deflection or deformation, and changes in the overall shape of human ribs is expected to influence the ability of those ribs to resist deformation when loaded (i.e., rib stiffness).

Chapter 4 takes the results from the prior two chapters and applies simulated mechanical loading to simplified FE models of ribs to describe how the changes in rib shape throughout the population affects their mechanical properties.

A final aim of this thesis is to take the ribs as they have been developed in prior chapters and to place them in an appropriate spatial context within the rib cage. Chapter 5 will test the suitability of the methodological approach taken for ribs in this study – where complex geometry is broken down to collections of parameters – to be generalized and applied to surrounding structures in order to build a coherent representation of thoracic skeletal anatomy. In doing so we can once again ask questions of the effects of demographics on geometry, this time with the ribs as part of their surrounding thoracic structure.

CHAPTER 2

A new shape model for human ribs

This chapter describes a new mathematical model for the overall geometric shape of human ribs. The model follows the in-plane shape of ribs using sections of logarithmic spirals (e.g., Figure 2.1), with the key locations for trimming the spirals being determined by a limited set of intrinsic rib properties such as its size, aspect ratio, and rib "skewness".

We provide the mathematical derivation for the model, and also test it on an initial sample of 100 individuals (2197 ribs) to assess its accuracy and its ability to aggregate individual ribs to form "average" rib geometry from a population.

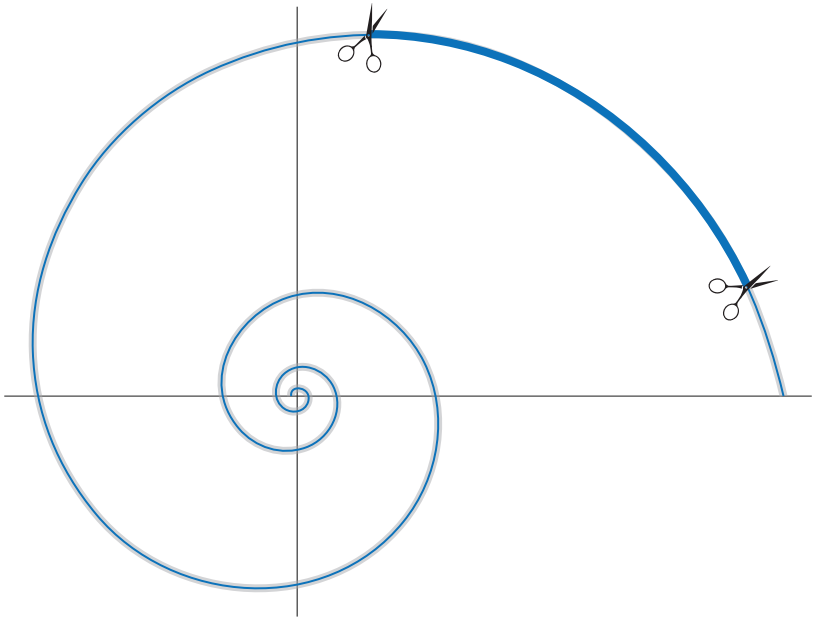

Figure 2.1: An example logarithmic spiral with a small curved section trimmed.

2.1 Background and previous models

As described in Section 1.4.1, the human rib shape has been characterized in a number of ways based on measures of primitive shapes including the use of arcs, circles, and ellipses as a geometric basis (Kent et al., 2001; Schultz et al., 1974; Margulies et al., 1989; Roberts and Chen, 1972; Roberts, 1977).

The most advanced of these – and the first to fully describe a rib's path from parameters alone – is a model from Kindig and Kent (2013) which uses a circle and a semi-ellipse that are joined by a parabolic patch, along with two straight patches at either rib end to create the full centroidal path. While providing a highly accurate model of overall shape at multiple rib levels, the Kindig and Kent rib model (illustrated in Figure 2.2) has some limitations, particularly when aggregating the parameters from multiple ribs to form new geometry. A full derivation of its circle and ellipse can be found in Kindig and Kent (2013), but we will focus on the circle which is placed using two parameters for its center (x_R, y_R), along with its radius parameter, R. This circle is subject to the constraint in Equation (2.1) requiring that it does not fully enclose the origin.

$$x_R^2 + y_R^2 \leq R^2 \tag{2.1}$$

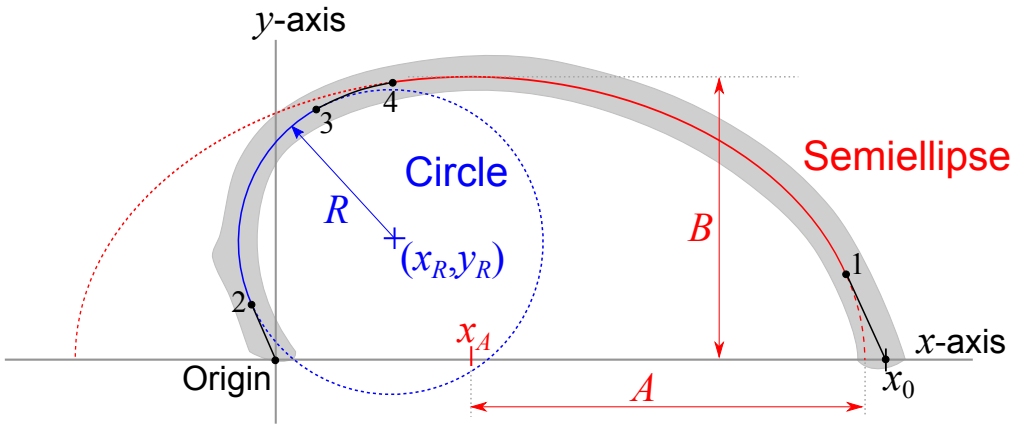

Figure 2.2: Kindig and Kent (2013) model overview showing circle and semiellipse placement. A model constraint requires the circle to avoid overlapping the origin.

One potential drawback of the Kindig and Kent model is that many individual rib shapes are best fit using a circle that passes very near the origin (i.e., $x_R^2 + y_R^2 \approx R^2$). In these cases, common "valid" rib geometry is immediately adjacent in parameter space to "invalid" geometry, so a statistical combination of valid parameters is in danger of stepping into that invalid territory. An example of this phenomenon is illustrated in Figure 2.3. Here, the red and green circles make two valid Kindig model rib shapes (typical for the shape of about ribs 8 to 10), but their average (shown by the blue circle) encompasses the origin and produces invalid geometry.

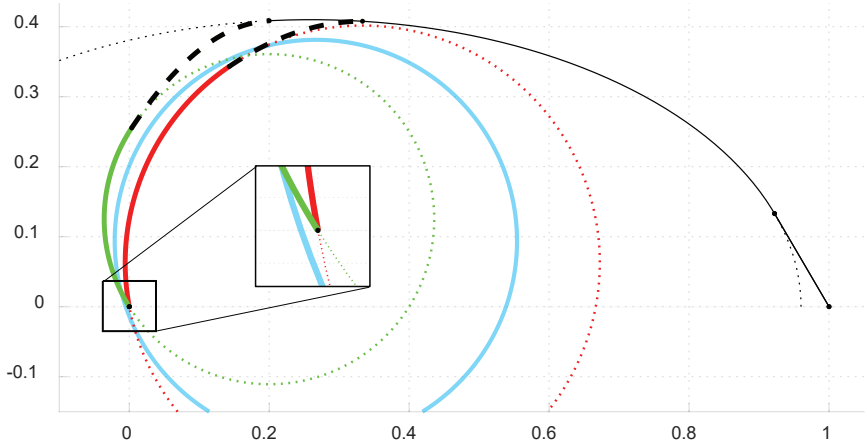

Figure 2.3: Example circle parameters whose average breaks Kindig and Kent (Kindig and Kent, 2013) constraints. The red and green circles show valid and typical circle placements, but their average (blue) encompasses the origin (thus breaking the constraint in Equation (2.1)) and is invalid.

Another limitation of the Kindig and Kent model is the potential for overfitting of rib shapes within the seven-parameter space. An example of this is shown in Figure 2.4. Here the green and red circle have x_R and R circle parameters which differ by about 2 standard deviations (using variances reported in the original paper). The red circle leads to a short parabola patch, while the green leads to a longer parabola (and shorter circle patch). However the resulting overall shape from these different parameter sets are seen to be substantially similar. Consequently, within the parameter space there are multiple ways of recreating (mostly) similar ribs, since in some cases different parameter configurations

can cause parts of the resulting model to be "passed" between belonging to the circle or belonging to the parabola.

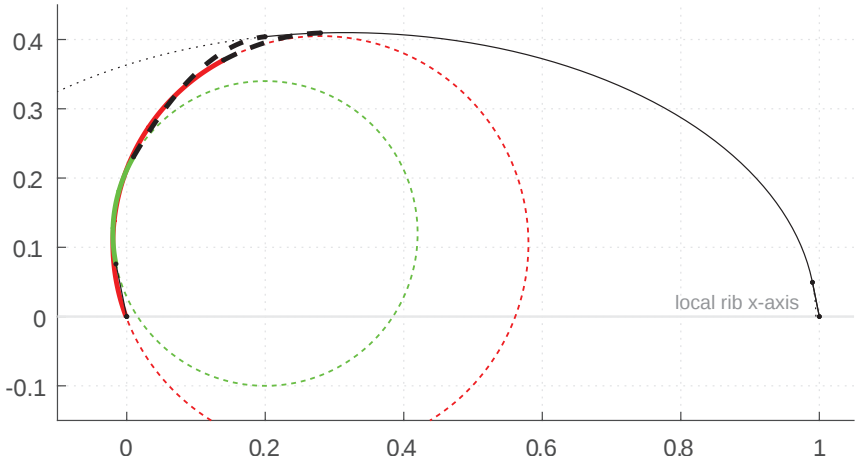

Figure 2.4: Exemplar different parameters producing largely similar ribs. The red and green circles have parameters which differ by 2 standard deviations, yet they produce mostly similar final geometry due to parts of the rib once modeled by the circle being "passed" to the parabola.

2.2 Rib geometry data source

As an initial data source for live human rib geometry, a total of 2197 unfractured ribs were analyzed from CT scans of 50 females and 50 males in the ICAM CT database. Subjects were chosen at random from those who met age criteria (20–69 years with 10 subjects per gender per decade), were free of skeletal abnormality (including scoliosis, kypohosis, bifurcating ribs or abnormal rib counts), were not pregnant at the time of scan, and had at least 9 rib levels fully visible within the scan window. All subject data was obtained under Institutional Review Board approval.

2.2.1 Centroidal path extraction

Rib centroidal geometry was extracted for all ribs using semi-automated routines written in MATLAB R2015b (The Mathworks, Natick, MA) to firstly place landmarks at each

rib end and then determine a series of 3D centroidal path points joining those end landmarks.

2.2.1.1 Distal (sternal) rib end

The transition from rib bone to costo-chondral cartilage at the distal end of each rib occurs through a cup-shaped depression at the rib end. To specify an unambiguous location for the transition point, and to retain consistency with past literature (Lau et al., 2011), software connected to the ICAM morphomics system was written to allow users to place markers at exactly at the apex of this concave transition to costal cartilage, as shown in Figure 2.5. It is not always possible to visualize this precise 3D landmark using only axial image slices, so the custom interface allowed users to first place an approximate marker via axial slices, then they were shown a set of small obliquely oriented image patches at different rotational angles in which the concave transition shape is clearly visible.

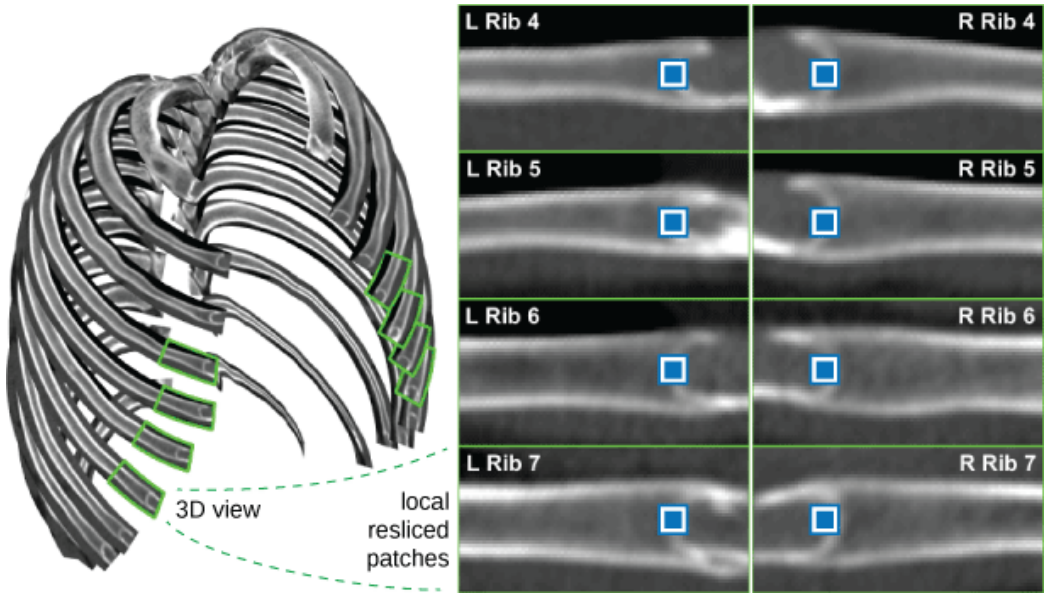

Figure 2.5: Rib end landmark placement at the distal (costo-chondral) rib end for ribs 4 through 7. Patches show locally resliced views of rib end regions that enhance the costo-chondral transition.

2.2.1.2 Proximal (vertebral) rib end

At the rib end that is proximal to the spine, there are two articulation points. Firstly, each rib articulates with the vertebra of its same number (i.e., rib 6 articulates with the T6 vertebral body). There is also a second articulation with the inferior aspect of the superior vertebra (i.e., rib 6 also articulates with the inferior aspect of the T5 vertebral body). Of these two locations, the articular rib surface at the same vertebra was designated as representing the proximal end of the rib. A custom interface was written allowing the user to scroll through a curved planar reformation centered on the spinal canal, with each slice showing the region perpendicular to the spine. In this region rib ends are visible and the orientation of the view is such that the articular surface between rib an vertebral body is clearest. In this view, a second landmark was placed on the cortical rib surface at this end as illustrated in Figure 2.6.

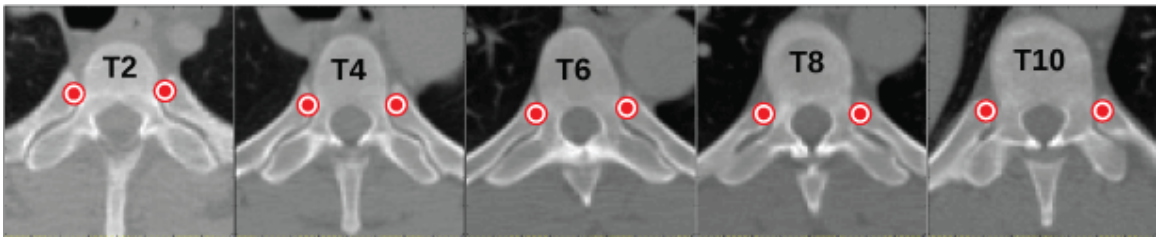

Figure 2.6: Rib end landmark placement at the proximal (to the spine) rib end for ribs 2, 4, 6, and 8. Each image shows a plane perpendicular to the spinal canal that is resampled from the original CT volume.

2.2.1.3 Rib centroidal path

Using an algorithm adapted from Staal et al. (2007), an initial rib path template was built linking these two end landmarks through the CT image space. This path was then iteratively refined by reslicing the CT image volume perpendicular to the rib as seen in Figure 2.7. The centroidal path points were set to match the 2D centroid of a filled segmentation of its cross-section.

Finally, a plane is fitted to each rib's centroidal path with a primary axis (the rib's local

x-axis) passing from the proximal to distal rib end points, and a secondary axis (the local y-axis) that is chosen so as to minimize the total out-of-plane deviation of all points along the rib's path.

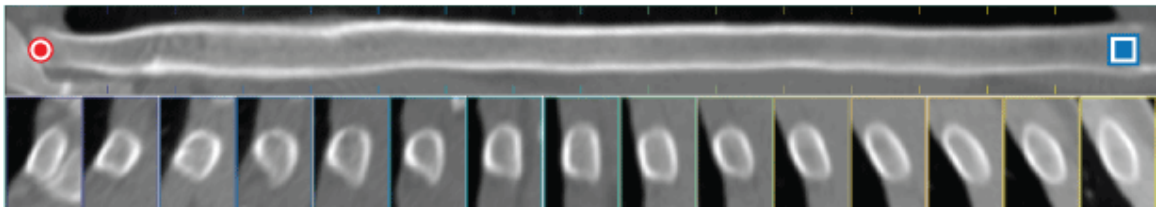

Figure 2.7: Cross-sectional cuts along the rib (upper) and perpendicular to the rib path (lower), where the 2D centroids of rib pixels provide the 3D centroidal path.

2.3 Logarithmic spiral rib shape model

Each set of 3D rib points are viewed "in-plane" with respect to the rib's fitted local x- and y-axes, and a rib shape model is built using one parameter describing the rib size and five describing the rib shape as set out in Table 2.1 and illustrated in Figure 2.8.

Table 2.1: Six independent in-plane parameters capturing centroidal rib shape.

Parameter	Quality	Definition
S_x	Size	Coordinate $[\mathrm{S_x}, 0]$ of distal rib end
X_{Pk}, Y_{Pk}	Shape (skewness, aspect ratio)	Normalized coordinate of rib peak (X,Y)
ϕ_{pia}	Shape (initial angle)	Proximal inner rib angle with X-axis
B_p	Local shape	Proximal spiral shape parameter
B_d	Local shape	Distal spiral shape parameter

The model consists of two logarithmic spiral segments, each separately defined based on four of the five (proximal spiral) or three of the five (distal spiral) shape parameters. These spiral segments are then transformed onto the rib's local coordinate system space to meet with zero slope at the rib's peak, and together create the full centroidal path geometry.

The first parameter, S_x, is the linear distance or span along the local x-axis between the two rib ends. S_x acts as an overall scale factor, and subsequent spatial parameters are given in normalized coordinates ($[X, Y]$) in which the distal rib end coincides with the local $[1, 0]$

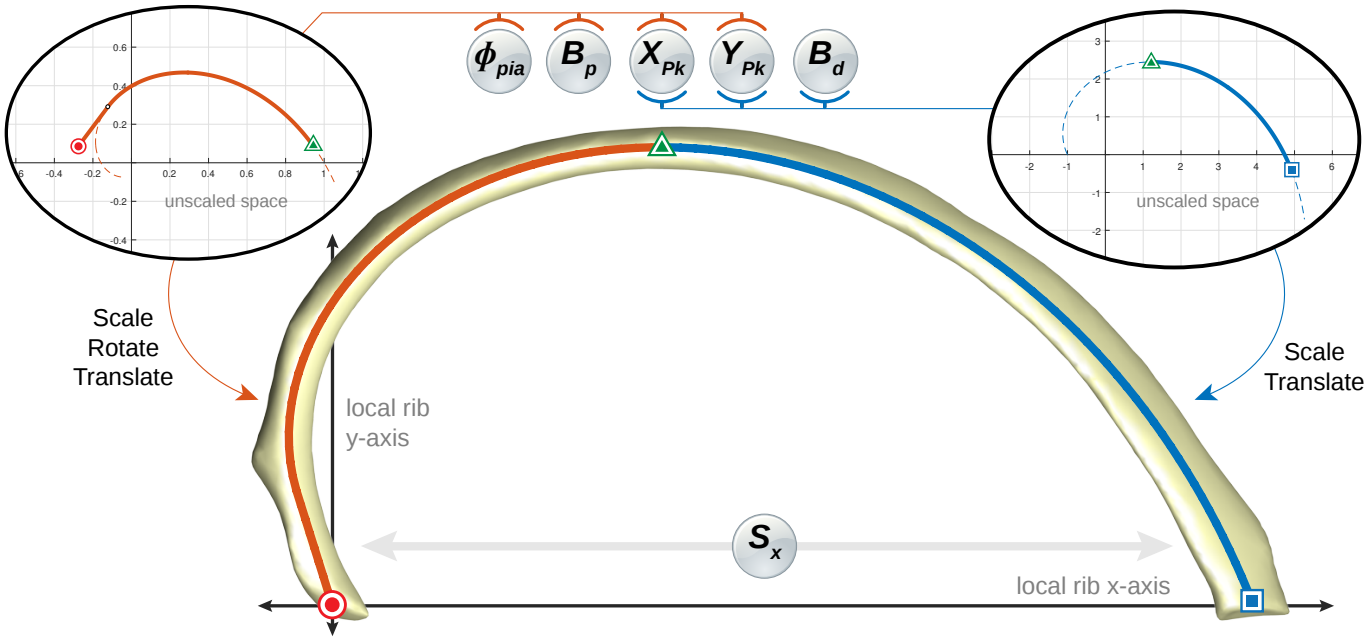

Figure 2.8: Six-parameter rib model with one size and five shape parameters. The proximal (red) and distal (blue) spiral portions (insets) are built from log-spiral equations in unscaled space, and then undergo transformation to meet with zero slope at the rib's peak. S_x acts as an overall scale, while other parameters define the shape of the distal (X_{Pk}, Y_{Pk}, B_d) and proximal (X_{Pk}, Y_{Pk}, B_p, ϕ_{pia}) portions.

coordinate. Two parameters then define the maximum Y-coordinate corresponding to the peak of the rib in normalized coordinates as $[X_{Pk}, Y_{Pk}]$, and mark the join between distal and proximal spirals as illustrated in Figure 2.8. The inner angle between the x-axis and the proximal end of the rib (ϕ_{pia}) and a spiral constant (B_p) define the final shape of the proximal logarithmic spiral spanning $[0, 0]$ to $[\mathrm{X_{Pk}}, \mathrm{Y_{Pk}}]$, and one parameter ($B_d$) gives the spiral shape spanning $[\mathrm{X_{Pk}}, \mathrm{Y_{Pk}}]$ to $[1, 0]$ as derived below.

In basic form, an unscaled logarithmic spiral can be defined by two functions with one constant (B_d, for the distal spiral) as follows:

$$\begin{aligned} x(\theta) &= -\mathrm{e}^{\mathrm{B_d}\,\theta}\cos\theta \\ y(\theta) &= \mathrm{e}^{\mathrm{B_d}\,\theta}\sin\theta \end{aligned} \tag{2.2}$$

That spiral reaches a local y-maximum at the θ_{pk} rotational coordinate which will later be scaled and translated to coincide with the rib peak at $[X_{Pk}, Y_{Pk}]$:

$$\theta_{pk} = 2\arctan(\sqrt{\mathrm{B_d}^2 + 1} + \mathrm{B_d}) \tag{2.3}$$

To find a second rotational coordinate θ_{end} that will coincide with the distal rib end after this transformation, consider that the slope of a line from $[x(\theta_{pk}), y(\theta_{pk})]$ to $[x(\theta_{end}), y(\theta_{end})]$ must equal the slope of a line from $[X_{Pk}, Y_{Pk}]$ to $[0, 1]$ as illustrated in Figure 2.9, which is:

$$M = \frac{\Delta Y}{\Delta X} = \frac{0 - Y_{Pk}}{1 - X_{Pk}} \tag{2.4}$$

θ_{end} is therefore given by the first solution to:

$$\frac{y(\theta) - y(\theta_{pk})}{x(\theta) - x(\theta_{pk})} = M \qquad \theta > \theta_{pk} \tag{2.5}$$

With known bounds at the θ_{pk} and θ_{end} rotational coordinates, a distal scale factor (SF_d) is found that re-scales the portion of the logarithmic spiral between these bounds to the appropriate size to span the rib-peak to rib-end distance in normalized coordinates:

$$\begin{aligned} dist_{xy} &= \sqrt{Y_{Pk}^2 + (1 - X_{Pk})^2} \\ dist_{XY} &= \sqrt{(x(\theta_{pk}) - x(\theta_{end}))^2 + (y(\theta_{pk}) - y(\theta_{end}))^2} \\ SF_d &= dist_{xy}/dist_{XY} \end{aligned} \tag{2.6}$$

Scaling and translation then transforms this spiral segment (between rotational coordinates θ_{pk} and θ_{end}) from its original space to normalized rib coordinates as:

$$\begin{aligned} X(\theta) &= [x(\theta) - x(\theta_{pk})] \times SF_{dist} + X_{Pk} \\ Y(\theta) &= [y(\theta) - y(\theta_{pk})] \times SF_{dist} + Y_{Pk} \end{aligned} \tag{2.7}$$

For the proximal spiral segment, we begin with a new logarithmic spiral and its first derivatives in Equations (2.8) and (2.9):

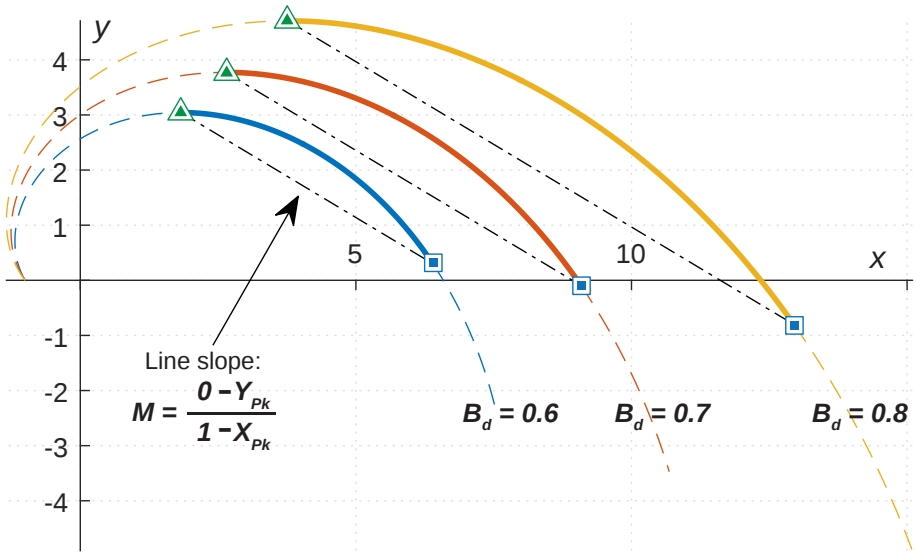

Figure 2.9: The distal spiral segment in unscaled mathematical space. After transformation to the local rib plane, the square and triangular markers will coincide with the rib's distal end and peak, respectively. Multiple spirals are shown using different values of $\mathrm{B_d}$ are shown, with $[X_{Pk}, Y_{Pk}] = [0.25, 0.45]$, and each has solid regions between spiral maximum at θ_{pk} and θ_{end} rotational coordinates as derived below.

$$
\begin{aligned}
x(\theta) &= \mathrm{e}^{\mathrm{B_p}\,\theta}\cos\theta \\
y(\theta) &= \mathrm{e}^{\mathrm{B_p}\,\theta}\sin\theta
\end{aligned}
\tag{2.8}
$$

$$
\begin{aligned}
\dot{x}(\theta) &= \mathrm{B_p}\,\mathrm{e}^{\mathrm{B_p}\,\theta}\cos\theta - \mathrm{e}^{\mathrm{B_p}\,\theta}\sin\theta \\
\dot{y}(\theta) &= \mathrm{B_p}\,\mathrm{e}^{\mathrm{B_p}\,\theta}\sin\theta + \mathrm{e}^{\mathrm{B_p}\,\theta}\cos\theta
\end{aligned}
\tag{2.9}
$$

We can calculate the angle α between a horizontal line and the line from the origin to the known rib peak position ($[\mathrm{X_{Pk}}, \mathrm{Y_{Pk}}]$) as:

$$
\alpha = \arctan\left(\frac{\mathrm{Y_{Pk}}}{\mathrm{X_{Pk}}}\right) \tag{2.10}
$$

A rotational coordinate, θ_{cut}, on the spiral at a location with slope matching this angle

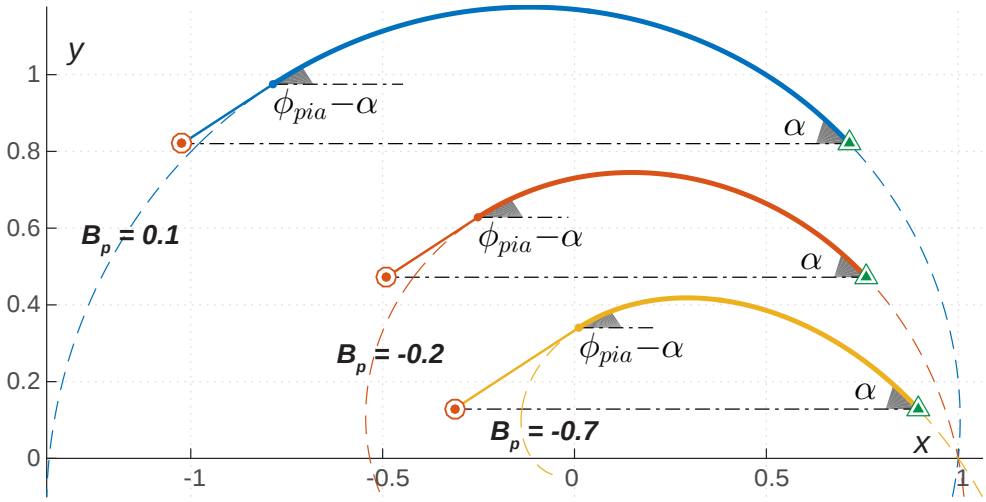

Figure 2.10: The proximal spiral segment in unscaled mathematical space. After transformation to the local rib plane, the circular and triangular markers will coincide with the rib's proximal end and peak, respectively. Multiple different values of $\mathrm{B_p}$ are shown, with $[X_{Pk}, Y_{Pk}] = [0.3, 0.32]$ and $\phi_{\mathrm{pia}} = 80°$. Solid regions lie between rotational coordinates θ_{cut} and $\theta_{tangent}$ (found using angle α as derived below), extended to meet a horizontal cutting level.

α is found by the solution (nearest $\theta = \pi/2$) to the equality:

$$\arctan2\left(-\dot{x}(\theta), -\dot{y}(\theta)\right) = -\alpha \tag{2.11}$$

Leading to a cutting coordinate in Cartesian space of $[x(\theta_{cut}), y(\theta_{cut})]$. After scaling and rotation (described below), this cut location will coincide with the rib peak $[\mathrm{X_{Pk}}, \mathrm{Y_{Pk}}]$.

A second rotational coordinate ($\theta_{tangent}$) is identified at the spiral location having a tangent angle equal to the difference of the rib shape's known proximal inner angle (ϕ_{pia}) and the α angle from Equation (2.10).

$$\alpha_{tangent} = \phi_{\mathrm{pia}} - \alpha_{cut} \tag{2.12}$$

The rotational coordinate $\theta_{tangent}$ can then be found by the solution to the equation:

$$\arctan2\left(-\dot{x}(\theta), -\dot{y}(\theta)\right) = \alpha_{tangent} \tag{2.13}$$

The spiral location $[x(\theta_{tangent}), y(\theta_{tangent})]$ has a tangential slope that forms an angle of $\alpha_{tangent}$ with the horizontal. Extending that tangential line down to intersect the horizontal at $y = y(\theta_{cut})$ completes the proximal spiral portion in its un-transformed $[x, y]$ space. The x-coordinate of that intersection can be found via:

$$x_o = x(\theta_{tangent}) - \frac{y(\theta_{tangent}) - y(\theta_{cut})}{\tan \alpha_{tangent}} \tag{2.14}$$

The coordinate $[x_o, y(\theta_{cut})]$ gives the position that, after transformation, will correspond to the proximal rib end at the origin of the normalized $[X, Y]$ plane.

With the rotational coordinates θ_{cut} and $\theta_{tangent}$ known, we apply successive translation, scale, and rotational transformations as set out in Equation (2.16) to transform the spiral from its original $[x, y]$ coordinates into normalized rib coordinates $[X, Y]$. Translation first shifts the spiral such that the end of the tangent line is coincident with the origin. Scaling (SF_p) is then applied as the ratio of the distance between spiral ends in unscaled $[x, y]$ space (as seen in Figure 2.10), and the target distance from the origin to the rib peak $[\mathrm{X_{Pk}}, \mathrm{Y_{Pk}}]$ in normalized $[X, Y]$ space:

$$\begin{aligned} len_{xy} &= x(\theta_{cut}) - x_{cut2} \\ len_{XY} &= \sqrt{Y_{Pk}^2 + X_{Pk}^2} \\ SF_p &= \frac{len_{XY}}{len_{xy}} \end{aligned} \tag{2.15}$$

Finally, rotation about the origin by α ensures that the $[x(\theta_{cut}), y(\theta_{cut})]$ coordinate on the spiral is mapped directly onto the $[\mathrm{X_{Pk}}, \mathrm{Y_{Pk}}]$ normalized rib peak. The full transformation matrix $\mathbf{T}$ is defined by its components as follows:

$$\mathbf{T} = \underbrace{\begin{bmatrix} 1 & 0 & 0 \\ 0 & 1 & 0 \\ -x_o & -y(\theta_{cut}) & 1 \end{bmatrix}}_{\text{translation}} \underbrace{\begin{bmatrix} SF_p & 0 & 0 \\ 0 & SF_p & 0 \\ 0 & 0 & 1 \end{bmatrix}}_{\text{scale}} \underbrace{\begin{bmatrix} \cos\alpha & \sin\alpha & 0 \\ -\sin\alpha & \cos\alpha & 0 \\ 0 & 0 & 1 \end{bmatrix}}_{\text{rotation}} \tag{2.16}$$

A direct transformation by $\mathbf{T}$ of homogeneous coordinates in $[x, y]$ can then be made to map the proximal spiral into place in normalized rib coordinates:

$$\begin{bmatrix} X(\theta) \\ Y(\theta) \\ 1 \end{bmatrix} = \mathbf{T} \times \begin{bmatrix} x(\theta) \\ y(\theta) \\ 1 \end{bmatrix} \tag{2.17}$$

Overall, the distal spiral segment (between rotational coordinates θ_{end} and θ_{pk}), the proximal spiral segment (between θ_{cut} and $\theta_{tangent}$), and the small straight segment joining $[X(\theta_{tangent}), Y(\theta_{tangent})]$ to the origin at $[0, 0]$ completely define the in-plane rib centroidal geometry via six free parameters.

2.3.1 In-plane optimized parameter fitting

With the in-plane rib parameterization scheme described in Section 2.3, a non-linear optimization was performed using MATLAB's Optimization Toolbox to match the optimal 6 in-plane parameters to each of the extracted rib centroidal paths.

The objective function being minimized was the sum-of-squared error (SSE) between 101 equally spaced points along the original rib central axis (i.e., the target geometry) and the rib path produced by the 6 in-plane rib parameters (the model geometry) as illustrated in Figure 2.11.

To ensure the global minimum was reached, the interior-point search algorithm was seeded via multiple sets of starting parameters based on the typical rib shapes for each rib number, and the solution with lowest error was chosen. In most cases each of the seed parameter sets converged to the same global minimum indicating that the parameter space produced a well conditioned gradient matrix in the objective function during the optimization.

To assist convergence during the optimization routine, linear constraints were applied

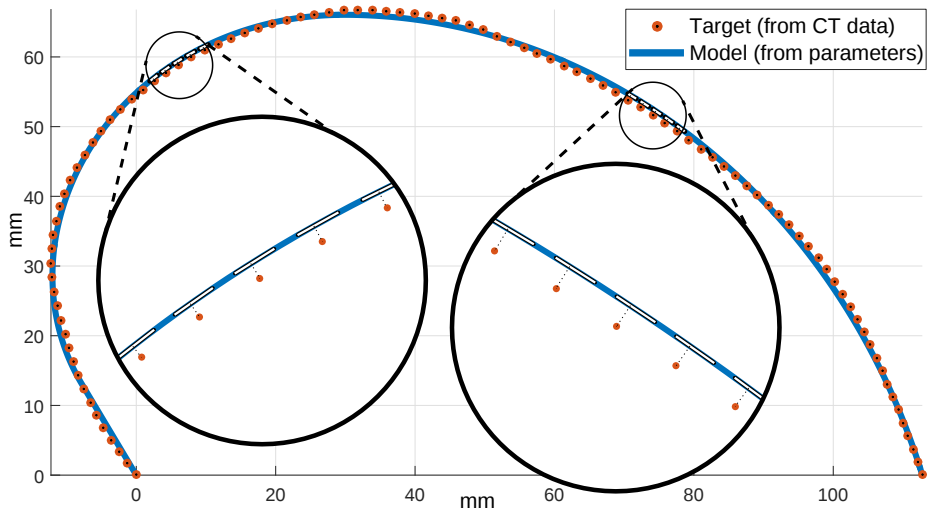

Figure 2.11: In-plane fitting error measurement between target points (extracted from CT images) and model curve. The error is the distance from each target point to a spiral tangent line with the same rotational coordinate, reported in non-normalized units (mm).

in the form of lower and upper bounds on each parameter as given in Table 2.2.

Table 2.2: Parameter constraints during in-plane optimization.

	X_{Pk}	Y_{Pk}	ϕ_{pia}	B_p	B_d
Lower bound	0.05	0.05	1	-2.0	-2.5
Upper bound	0.8	0.9	160	2.0	2.5

Furthermore, non-linear constraints were applied to the objective function to avoid mathematically infeasible parameter sets.

$$\begin{aligned} &\phi_{\mathrm{pia}} > \alpha \\ &\theta_{cut} > y\left(2\arctan\left(\sqrt{\mathrm{B_p}^2+1}+\mathrm{B_p}\right)+\pi\right) \end{aligned} \tag{2.18}$$

The first inequality in Equation (2.18) ensures that the inner angle at the proximal end (ϕ_{pia}) is not so shallow that it excludes the rib peak entirely. The second inequality in Equation (2.18) ensures that ϕ_{pia} is not so wide that it precludes any solution to the equality required in Equation (2.13). When fitting practically all rib shapes these constraints are trivially satisfied, however their explicit inclusion allows for a more economic search of the parameter space when fitting ribs during an optimization.

2.4 Results

2.4.1 Rib shape fit and variation by level

The rib shape model's accuracy was firstly evaluated by fitting it to centroidal paths originally presented in Kindig and Kent (2013). The mean squared error (MSE) between model and centroidal path was $0.23 \pm 0.16\,\mathrm{mm}^2$ (mean$\pm$std). This is a $56\,\%$ reduction in MSE from the previous circle-ellipse model ($0.52\,\mathrm{mm}^2$), or an approximately $34\,\%$ reduction in mean absolute error (MAE) describing the distance each real rib point deviated from the model. The model was then fit to the centroidal path geometry for all 2197 ribs in this study. The MSE for this CT-based data set was $0.29 \pm 0.18\,\mathrm{mm}^2$, and the resulting MAE was $0.40 \pm 0.15\,\mathrm{mm}$.

Figure 2.12 shows the median, inter-quartile range, and extrema across the full population for all six parameters by rib level. Average parameter values by gender are presented in Table 2.3. Using these data fed back into the shape model, sets of statistically average rib shapes for males and females were generated and are shown in Figure 2.13.

The trends seen by rib level in Figure 2.12 encapsulate the shape differences observed across the human rib cage. Firstly, rib sizes (S_x) in Figure 2.12(a) show the relative span of upper-, mid-, and lower-level ribs, with the largest (ribs 7-8) between $160\,\mathrm{mm}$ and $250\,\mathrm{mm}$. Figure 2.12(b) illustrates the aspect ratio and skewness of all ribs independent of size, with 2$^{\text{nd}}$ ribs having the roundest shape with median Y_{Pk} coordinates above 0.6, and a consistent reduction in Y_{Pk} (i.e., increase in aspect ratio) is found with each successive rib level. The X_{Pk} parameter describes overall rib skewness, with the median X_{Pk} values between 0.3 and 0.4, and lower X_{Pk} meaning a rib peak location is more highly skewed towards the rib's proximal end. Proximal inner angle (ϕ_{pia}) of ribs generally fall between $60°$ and $130°$, with highest ϕ_{pia} occurring in ribs 2-7 and transitioning smoothly in sequential levels. Trends in proximal and distal spiral constant parameters (B_p and B_d) in Figure 2.12(c) are less clearly distinguished by rib level, with overall ranges at each rib level relatively large

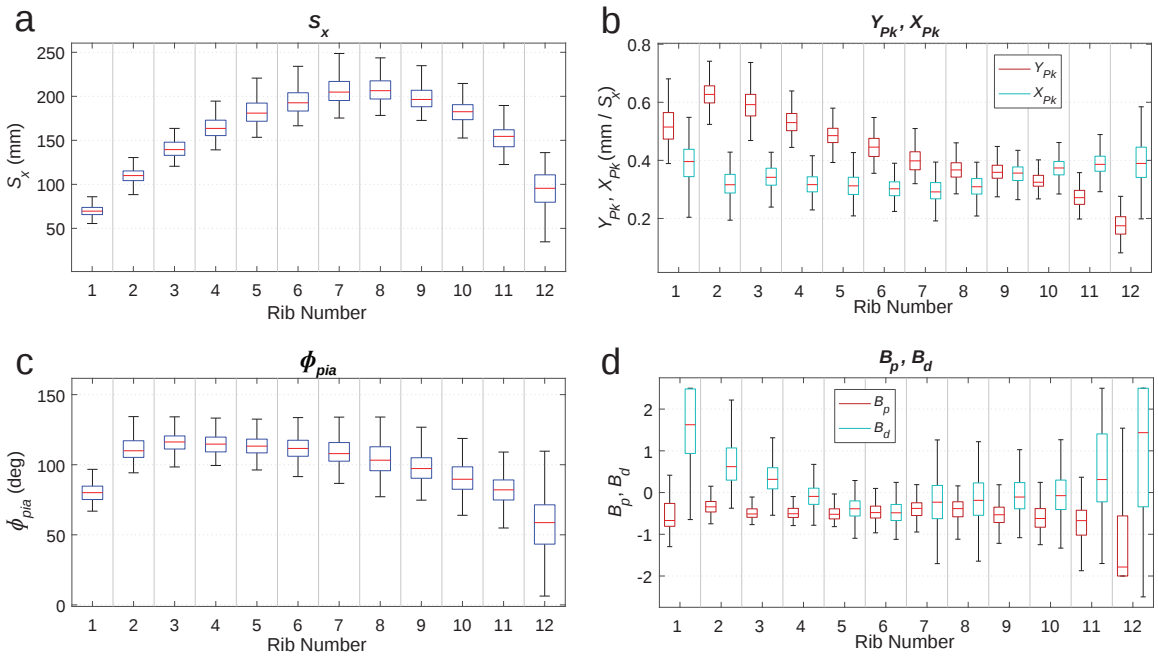

Figure 2.12: The overall trends in rib model parameters across the adult population (N=2197 ribs) including (a) rib end-to-end span, (b) rib peak location in normalized rib units, (c) proximal inner angle, and (d) proximal and distal spiral constants. Boxes show the median and the 25$^{\text{th}}$ to 75$^{\text{th}}$ quantile ranges and whiskers extend to the $\pm 2.7\sigma$ range ($99.7\,\%$ coverage).

when compared to differences between levels.

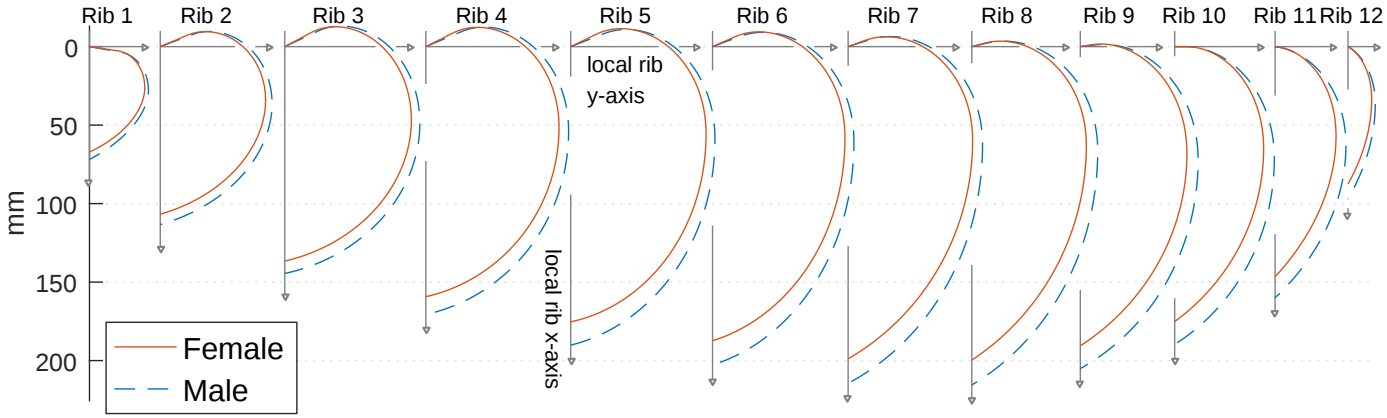

Figure 2.13: Average female and male rib shapes built from the mean parameter sets for each gender.

The most statistically significant ($p < 0.0001$) gender differences are seen in overall rib size, with male S_x values approximately $9\,\%$ larger than those of females for all ribs,

Table 2.3: Average rib shape parameter values for males and females. Parameters significantly different between genders ($p < 0.05$) are bolded.

#	S_x (mm)		X_{Pk}		Y_{Pk}		ϕ_{pia} (deg.)		B_p		B_d	
	M	F	M	F	M	F	M	F	M	F	M	F
1	**72**	**67**	0.39	0.39	0.52	0.52	80	81	−0.45	−0.50	**1.74**	**1.35**
2	**113**	**107**	0.32	0.32	0.63	0.63	111	113	−0.34	−0.31	0.71	0.72
3	**145**	**137**	0.34	0.34	0.60	0.59	**115**	**118**	−0.49	−0.48	0.34	0.40
4	**171**	**159**	0.32	0.32	0.53	0.53	**113**	**117**	−0.49	−0.48	−0.10	−0.05
5	**190**	**175**	0.31	0.32	0.48	0.49	**111**	**116**	−0.49	−0.50	−0.37	−0.37
6	**203**	**187**	**0.30**	**0.31**	0.44	0.45	**110**	**114**	−0.43	−0.48	**−0.54**	**−0.42**
7	**214**	**199**	0.29	0.30	0.40	0.40	108	110	−0.36	−0.42	**−0.30**	**−0.07**
8	**216**	**200**	0.31	0.31	0.37	0.37	103	105	**−0.35**	**−0.44**	**−0.27**	**−0.05**
9	**205**	**191**	0.35	0.36	0.37	0.36	**96**	**100**	−0.48	−0.56	**−0.19**	**0.08**
10	**190**	**175**	0.38	0.37	**0.33**	**0.32**	90	90	**−0.52**	**−0.64**	**−0.12**	**0.05**
11	**160**	**147**	0.39	0.39	**0.28**	**0.26**	81	84	**−0.56**	**−0.81**	0.46	0.73
12	**97**	**88**	0.38	0.39	0.18	0.17	61	59	−0.91	−1.18	1.00	0.88

making a difference of up to $18\,\mathrm{mm}$ for mid-level ribs. Significant shape differences by gender are also seen for a number of parameters at different regions of the rib cage ($p < 0.0001$). Females tend to have around $4°$ greater ϕ_{pia} rib angles at 3rd to 6th rib levels, along with higher B_d values from ribs 6–10. For ribs 9–11, females have lower Y_{Pk} values indicating slightly higher aspect ratios, along with higher values for B_p measurements.

2.4.2 Individual effect of parameters

The individual effect of each model parameter on overall rib shape is visualized in Figure 2.14. Here, the average female 6th rib parameters provide a baseline geometry (solid black line), and each parameter is then individually adjusted between ± 1.5 standard deviations from this mean. Figure 2.14 illustrates the primary roles of S_x, Y_{Pk}, and X_{Pk} in setting a rib's size, aspect ratio, and skewness, respectively. The remaining three parameters then control the local curvature at different locations on the rib, with ϕ_{pia} specifying the shape and angle of the proximal-most region, B_p controlling the curvature of the posteriorly curved region, and B_d controlling the shape and curvature of the distal rib portion.

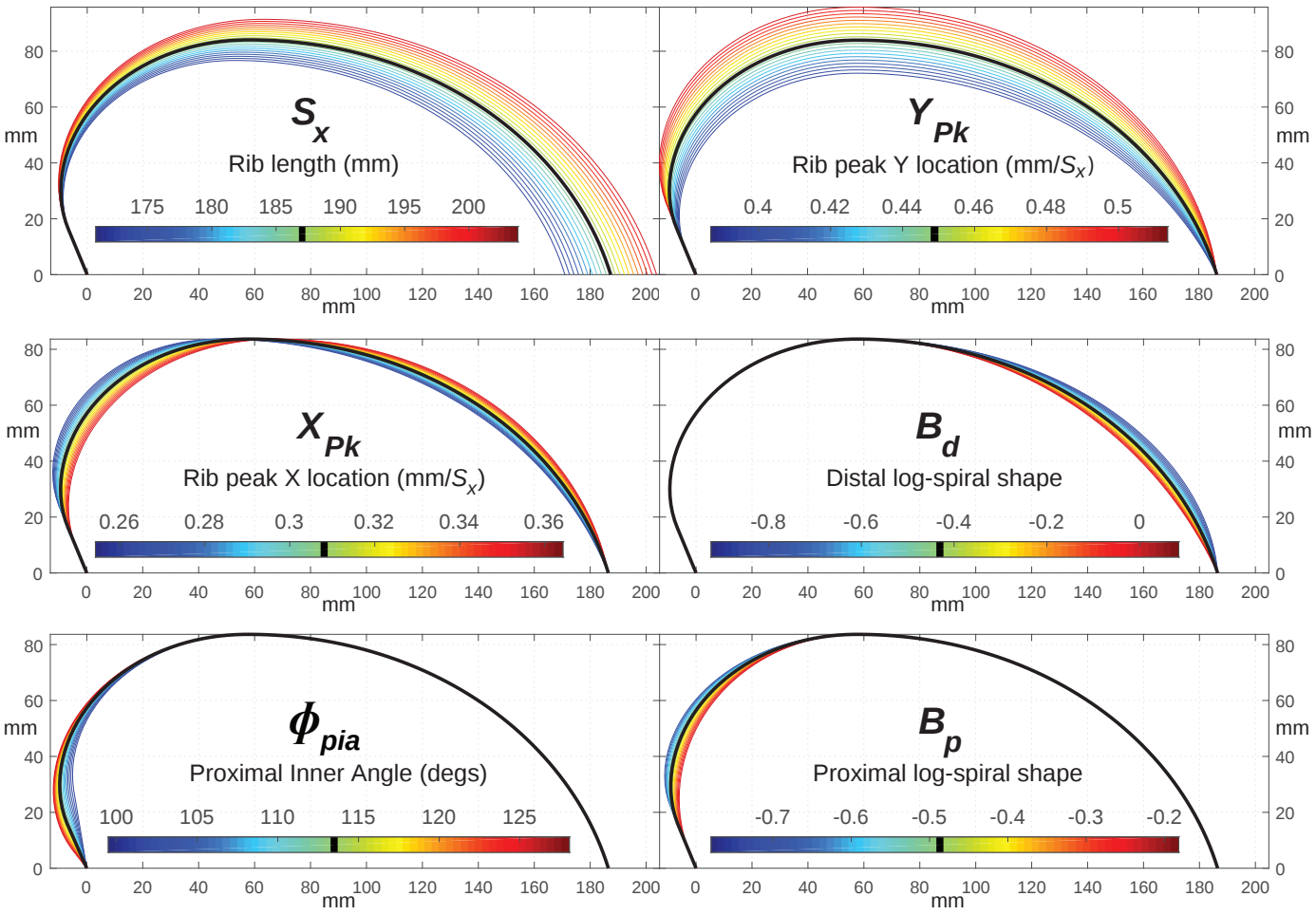

Figure 2.14: The individual effects of changing each model parameter on a typical 6th rib shape. The baseline shape (solid black line) is built from the average female parameter set, with each parameter separately varied within ± 1.5 standard deviations showing changes in size (S_x), aspect ratio (Y_{Pk}), skewness (X_{Pk}), distal curvature (B_d), proximal inner angle (ϕ_{pia}) and the amount of posterior protrusion in the proximal region (B_p).

2.4.3 FE simulated compression

A simple FE modeling system was set up in LS-DYNA (LSTC, Livermore, CA) based on the input of any 6-parameter rib shape. Rib geometry consisted of a 100-by-12 cylindrical mesh of quadrilateral elements at a radius of $5\,\mathrm{mm}$ around the centroidal path, with elastic material properties ($\rho = 2000\,\mathrm{kg/m^3}$, $E = 11\,\mathrm{GPa}$, $\nu = 0.3$), and a cortical shell thickness of $1\,\mathrm{mm}$, similar to those reported for rib cortical bone (Kemper et al., 2007; Granik and Stein, 1973; Li et al., 2010). Rib cross-section and material properties were kept constant along the rib and equivalent for all input so as to isolate the changes in mechanical behavior

driven directly by changes in overall rib shape. Ribs were quasi-statically loaded at the distal end while constraining both ends in all out of plane rotations, and allowing only translation of the distal end along the local x-axis as shown in Figure 2.15. The reaction force (F) and displacement (Δ) at the distal end is recorded, and the initial slope of the F/Δ relationship gives that rib's characteristic stiffness to axial loading.

Figure 2.15: FE simulation loading conditions. Out-of-plane rotations are constrained, with free x-displacement of the distal rib end.

All fitted rib shapes along with the statistically average male and female ribs underwent simulated compressive FE loading, and their resulting characteristic stiffness ($\mathrm{F/mm}$) was recorded. The shortest ribs showed highest stiffness (215 $\mathrm{N/mm}$ and 41 $\mathrm{N/mm}$ for the 12$^{\text{th}}$ and 1$^{\text{st}}$ ribs, respectively), with 5$^{\text{th}}$ ribs being least stiff as shown in Figure 2.16. Based on their in-plane geometry alone, female ribs were between $15\,\%$ (1$^{\text{st}}$ rib) and $35\,\%$ (10$^{\text{th}}$ rib) stiffer than male ribs ($p < 0.001$).

A more in-depth analysis of rib stiffness including the introduction of multiple loading configurations is provided in Chapter 4. The current results from the smaller female and male population in this chapter are presented as a way to assess the performance of the rib model in terms of representing aggregate mechanical properties from a collection of individuals.

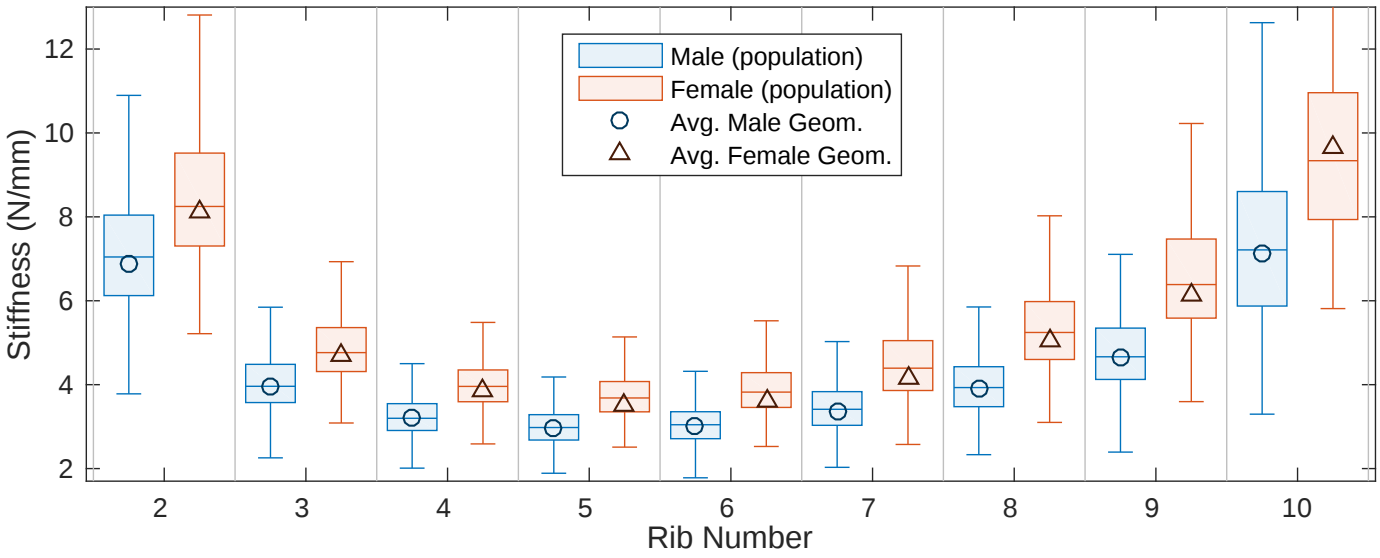

Figure 2.16: Rib stiffness ($\mathrm{N/mm}$) of all fitted ribs by level and gender showing stiffness overall range and interquartile range. Stiffnesses of statistically average ribs rebuilt from the male and female average parameter sets match well with the median stiffness within each population.

2.5 Discussion

2.5.1 Shape model considerations

In developing the rib shape model in this study, a number of desirable model properties were identified. Firstly, and in line with the model proposed by Kindig and Kent (2013), we aimed for a model whose parameters performed the dual roles of giving descriptive measures of rib shape while also allowing a full reconstruction of the centroidal path. Secondly, we aimed for model simplification in terms of its parameter space and underlying geometric makeup. The 7-parameter Kindig model is built from five patches (two primitives and three joins) whose interaction in some cases can produce similar rib shapes from different parameter sets; a possibility if changes in the primitives are largely offset by resulting changes in the position of joining patches. In the current model just three patches are used, and the two logarithmic spirals meet directly at the rib peak without any joining patches, effectively eliminating such interaction. The reduction to six model parameters coupled with a reduction in overall fit error indicates that the result is a simpler and more efficient

model of the rib centroidal path. Care has also been taken to select model parameters that are themselves direct geometric measures of overall shape. End-to-end size, aspect ratio, skewness, and inner angle at the proximal end are each clear geometric properties that can be measured directly from any rib shape without the need for mathematical fitting. In this way their interpretation is straightforward and intuitive to users of the model, and the average parameters from within a population produce valid rib geometry that has shape properties that are typical for that population. Finally, using logarithmic spirals as the shape primitive of choice gives the additional benefit of higher orders of curvature continuity than previous models (C^{∞} continuity compared to C^{1}), allowing for smoother and more predictable stress distributions when simulating mechanical loading of rib shapes.

2.5.2 Current results and rib shape comparisons

In this study both male and female rib shapes and sizes are reported. When comparing these results to past work, the average male rib spans (S_x) of all ribs matched within $2.2\,\%$ and $2.9\,\%$ to previous male-only 16-subject (Kindig and Kent, 2013) and 10-subject (Dansereau and Stokes, 1988) studies of rib geometry. In each case, differences in means between studies were within 0.4 standard deviations at all rib levels. Kindig and Kent (2013) also reported the normalized height of a semi-ellipse parameter that is similar in function and units to the aspect ratio (Y_{Pk}) reported here. While the two parameters do not represent identical aspects of rib shape, and indeed Y_{Pk} values are around $10\,\%$ larger than the semi-ellipse heights, the overall trends are found to match well with the 2$^{\text{nd}}$ rib having highest values followed by consistent reductions in each successive rib level.

Results from simulated compressive loading show that shape-dependent rib stiffness is influenced by rib size, with the smaller female ribs stiffer than the larger male ribs. Confidence in the shape model's utility is also gained from the fact that rib shapes that are rebuilt from the average male or female parameter sets also exhibit mechanical behavior that is typical for their representative population. Stiffness values for statistically average male

and female geometry was within 0.2 standard deviations of the mean population stiffnesses for rib levels 1–11, and within 0.1 standard deviations of the median population stiffness.

2.5.3 Limitations and applications

The shape model presented in this study focuses only on the parameterization of a rib's in-plane centroidal path, and other biomechanical factors such as out-of-plane deviation, cross-sectional geometry, or other changes in rib cortical surfaces and material properties are not included. As such, the simulated loading scenarios presented here are not direct models of real-world mechanical response and aim only to highlight the individual effect of overall shape on rib stiffness.

This results in this chapter also do not address interactions between rib parameters and other demographic variables such as age, stature, and weight when reporting average rib shapes for males and females. Indeed, subject stature is significantly correlated with rib S_x size ($p < 0.01$) for ribs 1–11, albeit with low r-squared values ($0.12 < R^2 < 0.32$). Elsewhere, rib arc length has also been found to be proportional to age (Bellemare et al., 2006; Kindig and Kent, 2013), and a number of demographics-based changes in overall rib cage shape have been identified (Gayzik et al., 2008; Shi et al., 2014; Weaver et al., 2014). Chapter 3 will apply the shape model proposed to a more broadly sampled population and explore the interaction between population demographics and the rib size and shape parameters.

Experimental studies of ribs under end-to-end loading show variability in resulting stiffness (Agnew et al., 2015; Beadle et al., 2015). Chapter 4 will expand the mechanical analysis – used here for testing model utility – to a larger population and to different loading conditions. This lets us explore how overall stiffness variation seen in the population through experimental studies might come from variation in rib shape. Importantly, this would shed light on the ability of computational models that are based on demographics alone to fully represent the breadth of variability seen in mechanical properties.

CHAPTER 3

Population trends in rib shape

This chapter takes the model for in-plane rib shape that was introduced in Chapter 2 and applies it to ribs sampled from a large population with broad demographics representative of adults in the US as a whole. Using four common demographic factors – namely age, height, weight, and sex – coupled with the rib shape parameters matching this large set of ribs, we can begin to understand the quantitative differences in rib size and shape that are present across the population.

In addition to investigating rib geometric shape we will also quantify the angle and orientation of ribs as they sit in the body. Doing so lets us compare the relative effect of changes in angle that come with age (previously understood to be a dominant aging effect) to the types and amount of age-related changes that we discover in rib shapes themselves. A final outcome of this chapter is a statistical model of overall rib shape that allows researchers to build representative rib geometry for any rib level and for any chosen subject demographic.

3.1 Methods

As described in the previous chapter (Section 2.2.1), rib centroidal geometry was extracted from CT scans and represented using curves and points in the 3D image volume space. To recap this process; points are manually placed at the end proximal to the spine (on the articulation point between rib and vertebral body) and the rib end distal to the spine (at the

apex of the cup-shaped costo-chondral junction). The centroidal path is then extracted by building an initial rib path between end points from an algorithm adapted from Staal et al. (2007), followed by iterative refinement of that path by taking cross-sectional slices through the CT volume and identifying the centroid of filled regions of segmented rib cortical bone.

3.1.1 Rib plane and orientation parameters

With rib path geometry represented by the sequence of centroids connecting adjacent cross-sections, a local rib coordinate system is then fitted having its origin at the rib's proximal end landmark, its local x-axis passing through the distal end landmark, and its local y-axis chosen so as to minimize the distance of all rib points from the local x-y plane. Using the orientation of this rib plane with respect to a fixed body reference allows us to quantify the 3D angle of ribs within the chest.

Three angles of inclination with respect to the anatomic planes are used; namely the rib's pump-handle angle (α_{PH}), lateral swing angle (α_{LS}), and bucket-handle angle (α_{BH}) (Margulies et al., 1989). These are illustrated in Figure 3.1 where α_{PH} determined by the angle between the rib local x-axis and the coronal plane, α_{LS} given by the angle between the rib local x-axis and the sagittal plane, and α_{BH} specified by rotation about the rib's local x-axis after the prior rotations are performed. Positive α_{BH} is defined as moving the lateral aspect of the rib superiorly, regardless of rib side.

The convention used allows an initial neutrally posed rib (on its correct side yet hanging directly inferiorly) to undergo successive rotations by α_{PH} (up from the sagittal plane), α_{LS} (away from the medial plane), then by α_{BH} (about the newly rotated x-axis, positive for left-sided ribs and negative for right-sided ribs), with the resulting rib being oriented correctly in the body habitus.

To compensate for any misalignment between the patient anatomical planes and the global scan coordinate system, a true ribcage lateral vector was created. It was specified as the normal direction to the best-fit-plane fitted through a point cloud consisting of:

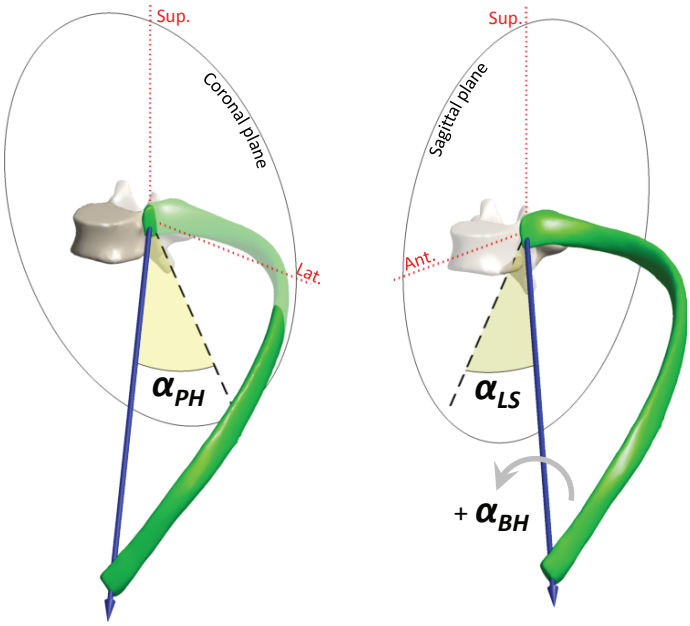

Figure 3.1: Rib plane parameterisation into pump-handle angle (α_{PH}), lateral swing angle off the mid-sagittal plane (α_{LS}), and bucket-handle angle. (α_{BH})

- Midpoints of all left and right posterior rib end pairs
- Points at the center of each thoracic vertebra
- Medial points placed along the sternum and *linea alba*

Rib plane rotation angles were then defined relative to orthogonal body coronal and sagittal planes derived from this body-lateral vector and the scanning bed.

3.1.2 Rib in-plane parametric shape model

Each set of 3D rib points are viewed “in-plane" with respect to the rib’s fitted local x- and y-axes, and the logarithmic spiral rib shape model first introduced in Chapter 2 is built using one parameter describing the rib size and five describing the rib shape as illustrated in Figure 3.2. To recap on the individual parameter effects, the S_x parameter controls the overall size of a rib by directly prescribing its end-to-end length. The rib’s peak is then given by the X-Y pair $[\mathrm{X_{Pk}}, \mathrm{Y_{Pk}}]$, expressed in coordinates normalized by S_x. Consequently, $1/\,\mathrm{Y_{Pk}}$ describes overall rib aspect ratio in terms of height in the local plane

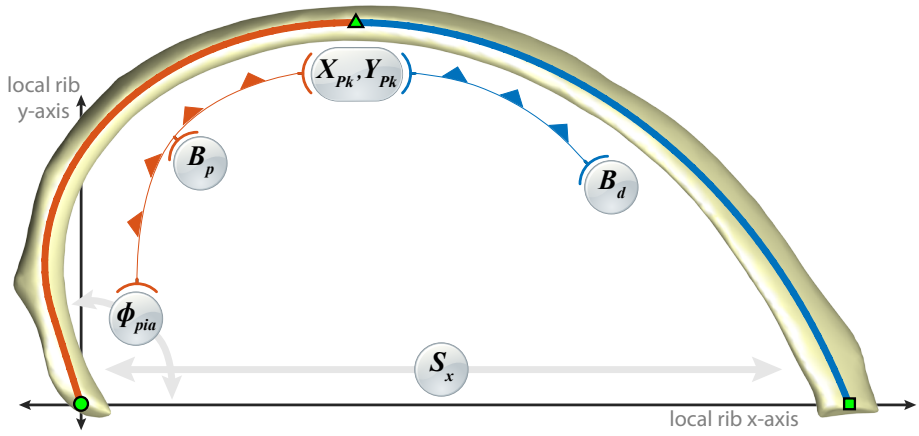

Figure 3.2: Six-parameter rib model with one size (S_x) and five shape parameters. The proximal (red) and distal (blue) spiral portions meet with zero slope at $[\mathrm{X_{Pk}}, \mathrm{Y_{Pk}}]$ in normalized rib coordinates, defining rib aspect ratio (Y_{Pk}) and skewness (X_{Pk}). ϕ_{pia} defines the inner angle between the proximal rib end and the local x-axis, while B_p and B_d are proximal and distal spiral constants, respectively.

versus S_x, while X_{Pk} describes "skewness" of the rib's shape independent of aspect ratio, with a low X_{Pk} moving the rib peak closer to the proximal end, while larger X_{Pk} values push this peak towards the distal end.

After aspect ratio and skewness are set, local curvature of the distal rib portion is controlled by B_d, with higher B_d producing a flatter shape and lower B_d resulting in the distal portion following a wider arc between the rib peak and its distal end. At the proximal end, the combination of ϕ_{pia} and B_p control local curvature, with with higher ϕ_{pia} and lower B_p resulting in a wider arc (with more posterior protrusion) from the rib peak towards the rib's proximal rib end. The ϕ_{pia} parameter directly controls the inner angle at the proximal rib end, and together both ϕ_{pia} and B_p control the length of a short straight segment protruding posteriorly at the direction specified by ϕ_{pia}. Anatomically, this straight segment occurs in a region associated with the neck of the rib, which is a flatter region that articulates with the transverse processes of the spine.

3.1.2.1 Derived shape properties

The shape model parameters include four direct geometric measures (size, aspect ratio, skewness, and proximal inner angle) as part of its parameterization. Additional geometric properties can be measured to further quantify aspects of the resulting rib shapes. Overall arc length in the local plane (L_{2d}), inner angle at the distal end (ϕ_{dia}), and local curvature at both the distal end (κ_{dist}) and posterior extension (κ_{post}) were chosen as additional derived measures, as illustrated in Figure 3.3.

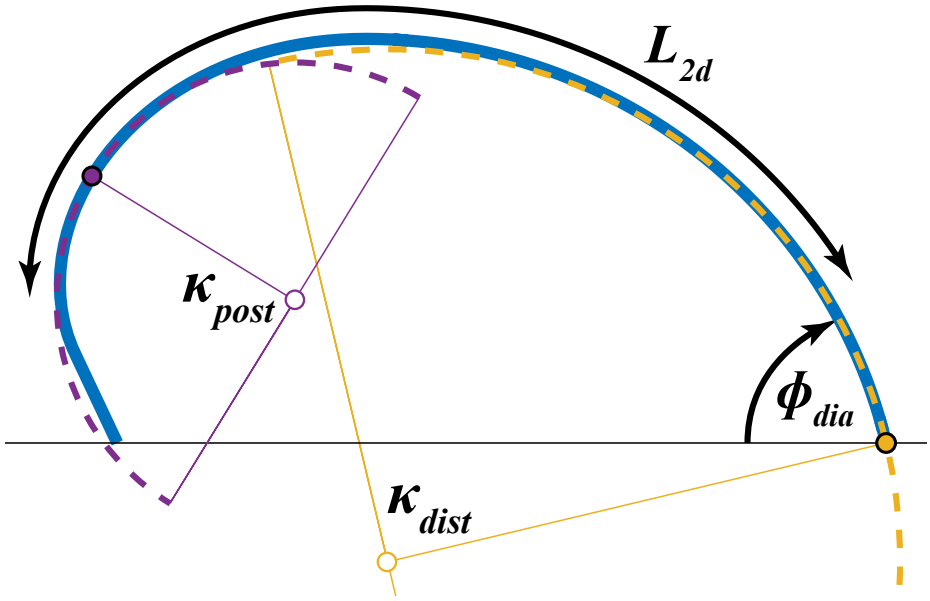

Figure 3.3: Derived geometric shape measurements of arc length (L_{2d}, mm), distal inner angle (ϕ_{dia}, deg) and local curvature at the rib posterior and distal end locations (κ_{post}, κ_{dist}, mm^{-1}).

The equation for the curvature κ at any given location θ of a logarithmic spiral has the basic form (Weisstein) given in Equation (3.1) below:

$$\kappa = \frac{\mathrm{e}^{-B\theta}}{a\sqrt{1+B^2}} \tag{3.1}$$

where B is the logarithmic constant (B_p for the proximal spiral and B_d for the distal spiral), and where a is the scale factor used to transform the unscaled spiral equations from their original $[x, y]$ space to the local rib plane. For the proximal spiral, $a = SF_p$ as defined

by Equation (2.15), and for the distal spiral, $a = SF_d$ as defined by Equation (2.6).

Substituting those factors along with either B_p or B_d into Equation (3.1) we can interrogate any proximal or distal rib location for its local curvature κ (or its radius of curvature which is $\frac{1}{\kappa}$).

The distal curvature is measured at the distal rib end rotational coordinate θ_{end} calculated in Equation (2.5). The proximal (posterior-most) curvature is measured at a new rotational coordinate position, θ_{post}. This position is given by the maximum y coordinate of the un-transformed proximal spiral as calculated in Equation (3.2), and corresponds to the position on the rib furthest away from a line joining the proximal rib end and the rib peak.

$$\theta_{post} = 2\arctan(\sqrt{\mathrm{B_p}^2 + 1} + \mathrm{B_p}) \tag{3.2}$$

3.1.3 Study population

Under IRB HUM00041441, 495 female and 505 male CT scans were collected from the ICAM scan database. Scans were from patients who entered a Level 1 trauma center and underwent abdomen and/or chest CT scanning as part of their normal course of diagnosis and treatment. This study reports only from an adult population ranging from 20 to 99 years of age, with overall population demographics shown by gender in Figure 3.4. Statistics from the study population are summarized in Table 3.1 alongside the CDC's anthropometric reference data for North American adults over 20 years of age from 2007–2010 (Fryar et al., 2012). Height and weight distributions from the study population followed the same trends as the comparison CDC reference group, with the study population in general slightly heavier and taller than the comparison cohort.

Male differences in weight between cohorts are less than $1.5\,\mathrm{kg}$ $(0.05\,\mathrm{SD})$ for the 5$^{\text{th}}$ through 90$^{\text{th}}$ percentile groups and height differences are below $2.6\,\mathrm{cm}$ $(0.18\,\mathrm{SD})$ in all except the 10$^{\text{th}}$ percentile group. The female study population is around $2.5\,\mathrm{kg}$ $(0.09\,\mathrm{SD})$

Table 3.1: Study demographics mean and percentiles (in bold), along with CDC reference population data in parentheses (Fryar et al., 2012).

Males (N = 505)	Mean	Std.	5th	10th	25th	50th	75th	90th	95th
Weight, kg	**89.6** (88.7)	**21.4** (33.8)	**63.0** (61.5)	**68.0** (66.5)	**75.0** (75.0)	**86.0** (86.1)	**100.0** (98.9)	**113.0** (114.4)	**130.6** (124.1)
Height, cm	**178.1** (175.9)	**7.7** (15.0)	**165.0** (163.2)	**169.8** (166.0)	**173.0** (170.9)	**178.0** (176.1)	**183.0** (180.9)	**188.0** (185.4)	**190.0** (188.2)
Females (N = 495)									
Weight, kg	**78.2** (75.4)	**22.5** (26.8)	**52.0** (50.2)	**55.0** (53.6)	**62.7** (61.1)	**73.0** (71.3)	**88.0** (85.5)	**109.0** (102.2)	**123.1** (113.8)
Height, cm	**163.6** (162.1)	**7.7** (10.8)	**152.0** (150.7)	**155.0** (153.1)	**159.0** (157.3)	**163.0** (162.1)	**168.0** (166.8)	**173.0** (170.9)	**177.8** (173.7)

heavier than the CDC cohort in the 5th through 75th percentile groups, with the heaviest groups differing by up to 10 kg. The heights of individuals in this study population are between 1 and 4 cm taller than those of the CDC cohort.

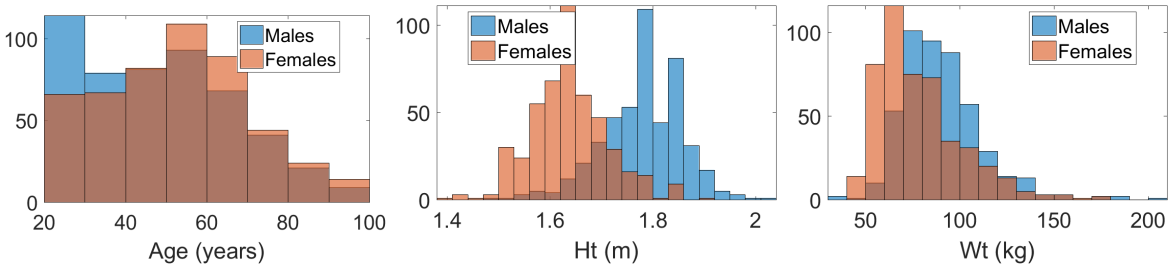

Figure 3.4: Population histograms showing the age, height and weight distributions for males and females within the studied population.

3.1.3.1 Individual ribs present in scan

From the 1000 adult CT scans in this study, a total of 22,692 individual ribs were analyzed. This is fewer than the maximum of 24 ribs per scan due to the fact that not all scans cover the entire chest region, and only ribs that were fully present within the scan window were included.

Furthermore, 239 of the 1000 adults had one or more rib fractures identified in their scan either through radiology reports associated with the CT image or visual inspection. All fractured ribs were excluded from this study leaving 21,124 included observations.

Figure 3.5 shows counts of included and excluded ribs at each rib level 1–12. Mid-level ribs were the most commonly fractured and therefore had a greater exclusion rate than other ribs. However, all levels from 2 through 12 retained at least 1500 uninjured ribs as observations. Rib 1 had fewest observations due to the fact that scan operators will usually scan only up to the apex of the lungs, whereas the first rib often extends above this apex.

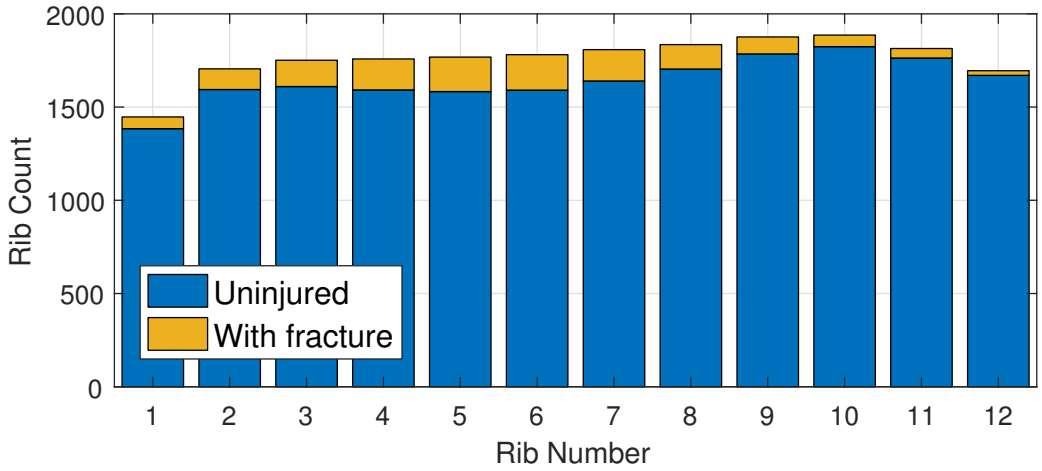

Figure 3.5: Counts of uninjured (included) and fractured (excluded) adult ribs present in study CT scans.

3.1.4 Statistical methods

As first described in Section 2.3.1, rib data was once again fit using non-linear optimization to obtain the shape model parameter sets corresponding to rib shapes closest to the underlying real rib data. This produced a large dataset of optimally fit rib parameters, with each rib corresponding to a person of known demographics (age, height, weight, and sex).

After exploring the suitability of the population-wide rib parameter values to regression analysis, two sets of regression analyses — performed in MATLAB — are reported in this study. The first set of analyses use univariate regression for each gender and rib to describe the overall trends in rib parameter values with increasing age.

The second set of analyses use multivariate regression of parameter values to the com-

bined demographic predictors of age, height, weight, and sex. Comparison of the explanatory power when predicting rib shape parameter values across the population is given between the univariate and multivariate regression models, and they are further compared to the potential explanatory power gained by adding interactive terms between demographic factors to the multivariate models.

3.2 Results

3.2.1 Rib shape fit and variation by level

The six-parameter rib shape model was fitted to $21{,}124$ uninjured adult ribs. For in-plane model fitting, the the mean squared error (MSE) between the parameterized model and points on the original geometry was $0.33\,\mathrm{mm}^2$, amounting to a mean absolute error (MAE) per rib location of $0.41\,\mathrm{mm}$.

Overall parameter trends by rib level matched closely to those reported from the smaller population of the previous chapter thus will not be discussed in detail here. Population means and standard deviations for all in-plane rib parameters along with the values found for rib orientation are given in Table 3.2.

3.2.1.1 Statistical properties of fitted data

Before building parameter regression models, inter- and intra-parameter correlations were investigated and the underlying assumption of normality in the population parameter distributions was checked. Distributions of parameter data showed normality at each rib level, with exemplar data including inter-parameter correlations from the 6$^{\text{th}}$ rib shown in Figure 3.6. Here it can be seen that most parameters' distributions are independent of one another, with the strongest correlations between S_x and Y_{Pk} (Pearson's $R = 0.64$) and Y_{Pk} and X_{Pk} ($R = 0.43$) showing that ribs with higher aspect ratio (designated by lower Y_{Pk}) tend to be longer and also have their peak slightly shifted towards the middle of the

Table 3.2: **Average** $\pm$ standard deviation in fitted in-plane parameters and rib orientation parameters for all rib levels.

Rib	N	S_x mm	X_{Pk} mm/S_x	Y_{Pk} mm/S_x	ϕ_{pia} deg	B_p -	B_d -	α_{PH} deg	α_{LS} deg	α_{BH} deg
1	1388	**70.8** $\pm$7.0	**0.385** $\pm$0.059	**0.520** $\pm$0.059	**81.7** $\pm$9.2	**-0.44** $\pm$0.59	**1.85** $\pm$1.16	**58.2** $\pm$9.8	**36.1** $\pm$7.0	**11.6** $\pm$7.4
2	1598	**110.8** $\pm$9.6	**0.318** $\pm$0.048	**0.621** $\pm$0.054	**112.0** $\pm$8.6	**-0.32** $\pm$0.23	**0.71** $\pm$0.56	**60.5** $\pm$9.6	**20.3** $\pm$4.7	**5.4** $\pm$6.9
3	1614	**141.6** $\pm$11.8	**0.344** $\pm$0.041	**0.587** $\pm$0.057	**117.1** $\pm$8.2	**-0.51** $\pm$0.15	**0.36** $\pm$0.43	**61.2** $\pm$9.1	**20.6** $\pm$3.9	**5.4** $\pm$7.1
4	1596	**166.7** $\pm$13.5	**0.321** $\pm$0.041	**0.527** $\pm$0.053	**115.7** $\pm$8.5	**-0.50** $\pm$0.16	**-0.05** $\pm$0.37	**60.4** $\pm$8.8	**22.8** $\pm$3.6	**6.8** $\pm$7.3
5	1587	**184.8** $\pm$15.1	**0.311** $\pm$0.041	**0.480** $\pm$0.049	**114.3** $\pm$8.7	**-0.51** $\pm$0.18	**-0.38** $\pm$0.35	**59.3** $\pm$8.7	**24.6** $\pm$3.4	**8.0** $\pm$7.4
6	1595	**197.3** $\pm$16.0	**0.297** $\pm$0.042	**0.439** $\pm$0.048	**112.5** $\pm$9.6	**-0.45** $\pm$0.21	**-0.52** $\pm$0.40	**57.7** $\pm$8.6	**27.9** $\pm$3.7	**10.5** $\pm$7.3
7	1644	**208.7** $\pm$16.1	**0.283** $\pm$0.043	**0.391** $\pm$0.045	**109.8** $\pm$11.0	**-0.35** $\pm$0.26	**-0.18** $\pm$0.66	**56.0** $\pm$8.3	**33.8** $\pm$4.3	**14.4** $\pm$7.1
8	1708	**209.0** $\pm$15.8	**0.296** $\pm$0.043	**0.364** $\pm$0.039	**105.3** $\pm$11.2	**-0.33** $\pm$0.29	**-0.22** $\pm$0.64	**53.8** $\pm$8.0	**39.8** $\pm$4.8	**16.4** $\pm$7.5
9	1789	**198.8** $\pm$15.2	**0.345** $\pm$0.041	**0.356** $\pm$0.036	**97.8** $\pm$11.3	**-0.51** $\pm$0.31	**-0.09** $\pm$0.59	**53.1** $\pm$7.7	**46.4** $\pm$5.3	**13.8** $\pm$7.6
10	1828	**183.5** $\pm$15.0	**0.371** $\pm$0.037	**0.329** $\pm$0.034	**90.4** $\pm$11.2	**-0.62** $\pm$0.35	**-0.09** $\pm$0.61	**51.5** $\pm$7.0	**56.0** $\pm$6.4	**11.1** $\pm$7.9
11	1767	**153.9** $\pm$17.3	**0.387** $\pm$0.037	**0.275** $\pm$0.036	**83.3** $\pm$12.8	**-0.70** $\pm$0.56	**0.61** $\pm$1.37	**49.5** $\pm$5.9	**69.9** $\pm$7.7	**10.2** $\pm$8.9
12	1674	**95.6** $\pm$29.0	**0.388** $\pm$0.099	**0.175** $\pm$0.044	**62.0** $\pm$25.6	**-1.29** $\pm$1.67	**1.36** $\pm$2.17	**53.2** $\pm$8.4	**94.0** $\pm$12.1	**14.3** $\pm$17.5

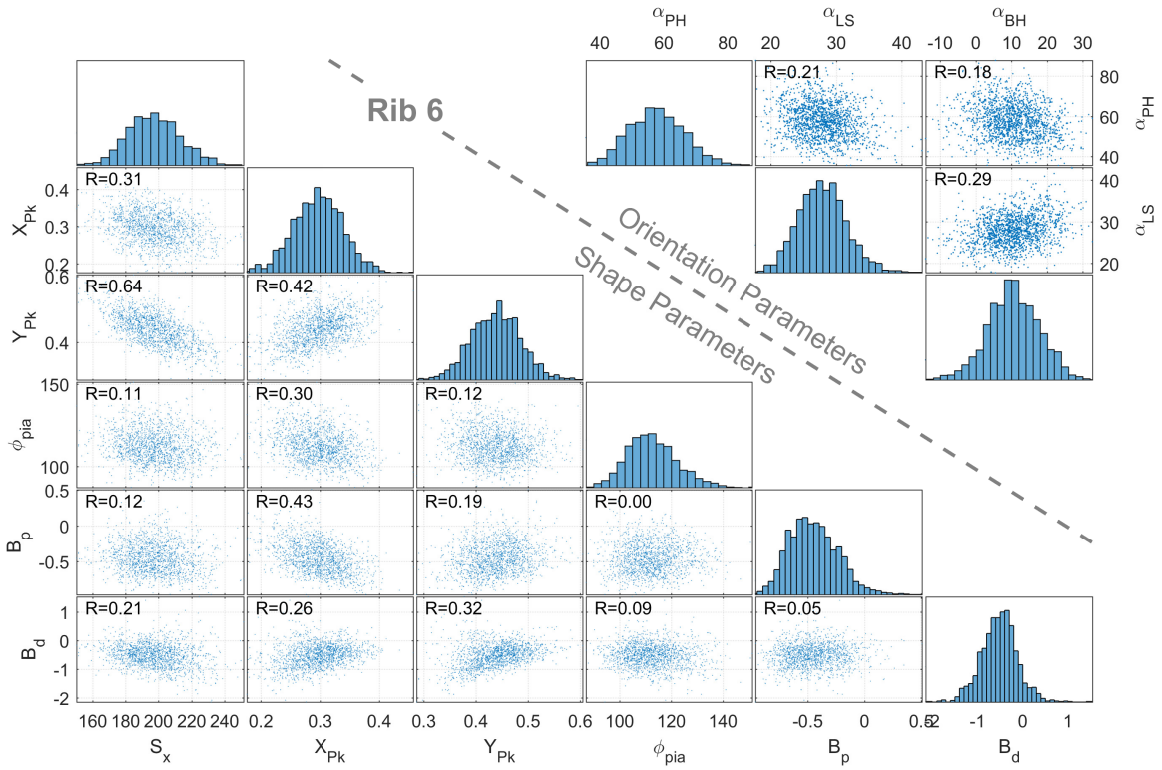

Figure 3.6: Individual parameter histograms (main diagonal) and inter-parameter correlation plots for the 6th ribs. Histograms show parameter distributions in the population to be largely normal. Inter-parameter correlations are low for most parameter combinations, with the strongest between rib size (S_x) and aspect ratio (Y_{Pk}).

rib (lower skewness). Across the rib cage these correlations were strongest in longer ribs (levels 4–7) and relatively small for other rib levels.

Pairs of left and right uninjured ribs from the same individual and rib level were collected and the correlation between their respective parameter sets calculated in Table 3.3. Results show highest symmetry in the length of ribs (S_x), Pearson coefficient up to 0.94 for mid-level ribs), aspect ratio (Y_{Pk}, up to 0.91), and skewness (X_{Pk}, up to 0.78). Less symmetry is seen between sides in terms of properties that affect local curvature patterns (ϕ_{pia}, B_d, and B_p), however given the goal of describing population trends in overall rib shape we chose to pool left and right sided ribs for subsequent analyses.

Table 3.3: Pearson's correlation coefficient between the fitted parameters of pairs of left and right sided ribs from the same individuals.

Rib	Pairs	S_x	X_{Pk}	Y_{Pk}	ϕ_{pia}	B_p	B_d
1	639	0.85	0.44	0.79	0.53	0.08	0.27
2	756	0.91	0.65	0.84	0.60	0.55	0.42
3	765	0.92	0.69	0.88	0.46	0.58	0.49
4	751	0.93	0.72	0.89	0.46	0.62	0.52
5	739	0.94	0.74	0.91	0.53	0.61	0.62
6	745	0.94	0.76	0.90	0.53	0.62	0.59
7	769	0.93	0.78	0.91	0.59	0.62	0.61
8	804	0.92	0.77	0.88	0.64	0.66	0.55
9	858	0.92	0.75	0.85	0.62	0.62	0.55
10	885	0.91	0.69	0.84	0.56	0.55	0.50
11	855	0.91	0.56	0.84	0.41	0.57	0.64
12	804	0.90	0.52	0.75	0.49	0.40	0.30

3.2.2 Univariate trends with age

Linear regression to age was performed on the male and female population results for each parameter and at each rib level. These results are shown in Figure 3.7 (size and shape parameters) and Figure 3.8 (rib orientation parameters) in the form of scattered data with the fitted regression lines for males and females, along with the explanatory power (r-squared) of the regression to age.

The first row of plots in Figure 3.7 show that there is indeed a trend in rib end-to-end span (S_x) with age with both male and female rib ends tending to separate over time. The slope for both genders at the 6$^{\text{th}}$ rib level is approximately $2.5\,\mathrm{mm/decade}$, with an r-squared value of $8\,\%$ for females and $7\,\%$ for males. A similar and significant trend is seen for rib levels 1 through 11 ($p < 0.001$). The second row of scattered data in Figure 3.7 shows that increasing age is correlated with a decrease in the Y_{Pk} parameter (i.e., increase in aspect ratio, $p < 0.001$ for ribs 1–11). Age alone explains around $20\,\%$ of the aspect ratio variation at mid-level ribs in females and $16\,\%$ in males. Rib skewness (X_{Pk}) also shows strong trends with age, particularly for lower-level ribs (5–11). As individuals age, rib skewness in these areas tends to increase, with age capable of explaining around $9\,\%$ of the population variance in both genders for the 7$^{\text{th}}$ rib level. Other rib shape parameters

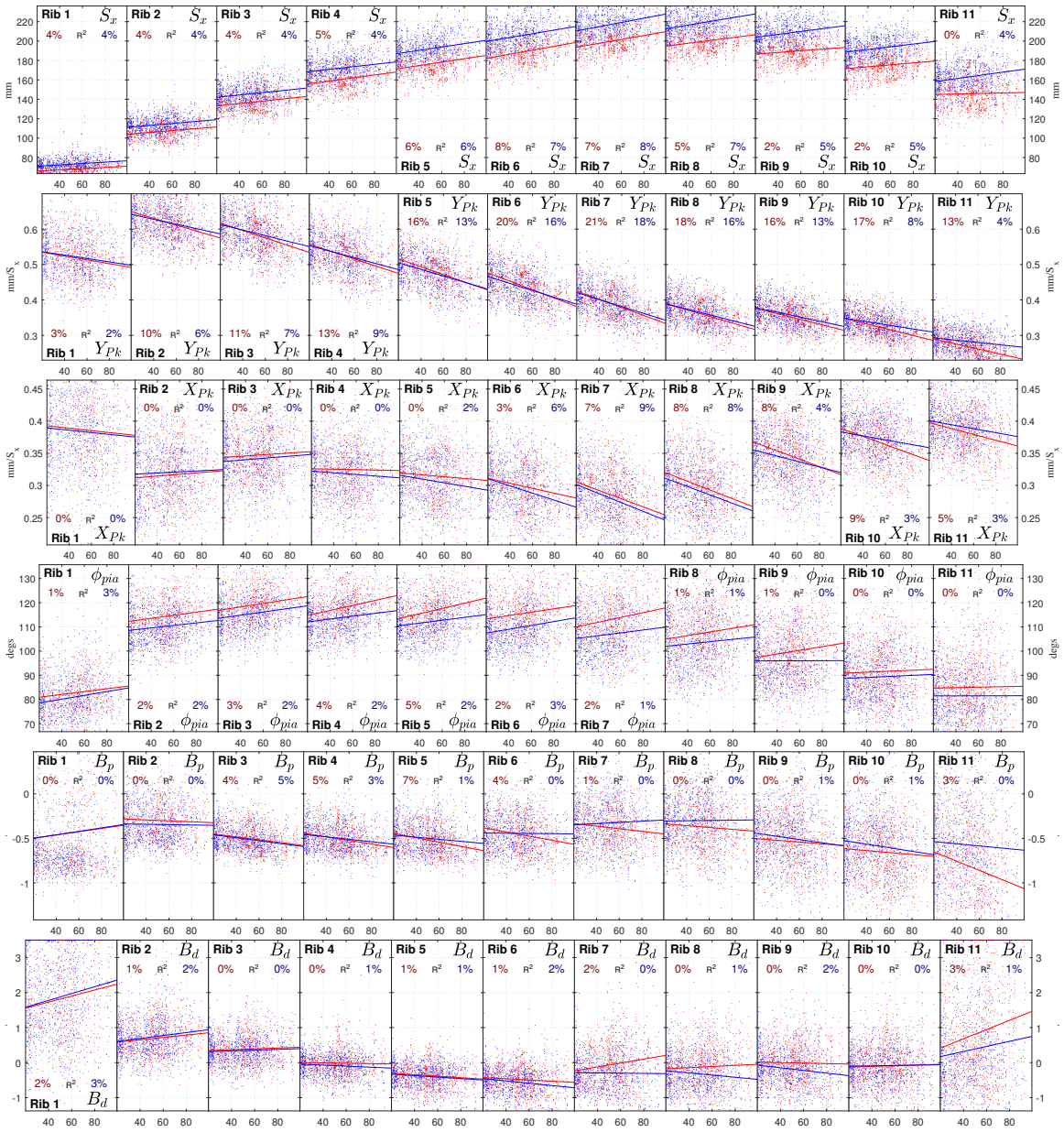

Figure 3.7: Data point cloud showing all fitted in-plane parameters between ages 20 and 90 years for males (blue) and females (red). Linear regression lines are shown along with their explanatory power (r-squared). Strongest trends with age are seen for rib aspect ratio (Y_{Pk}), rib end-to-end length (S_x), and rib skewness (X_{Pk}) in mid- and lower-level ribs.

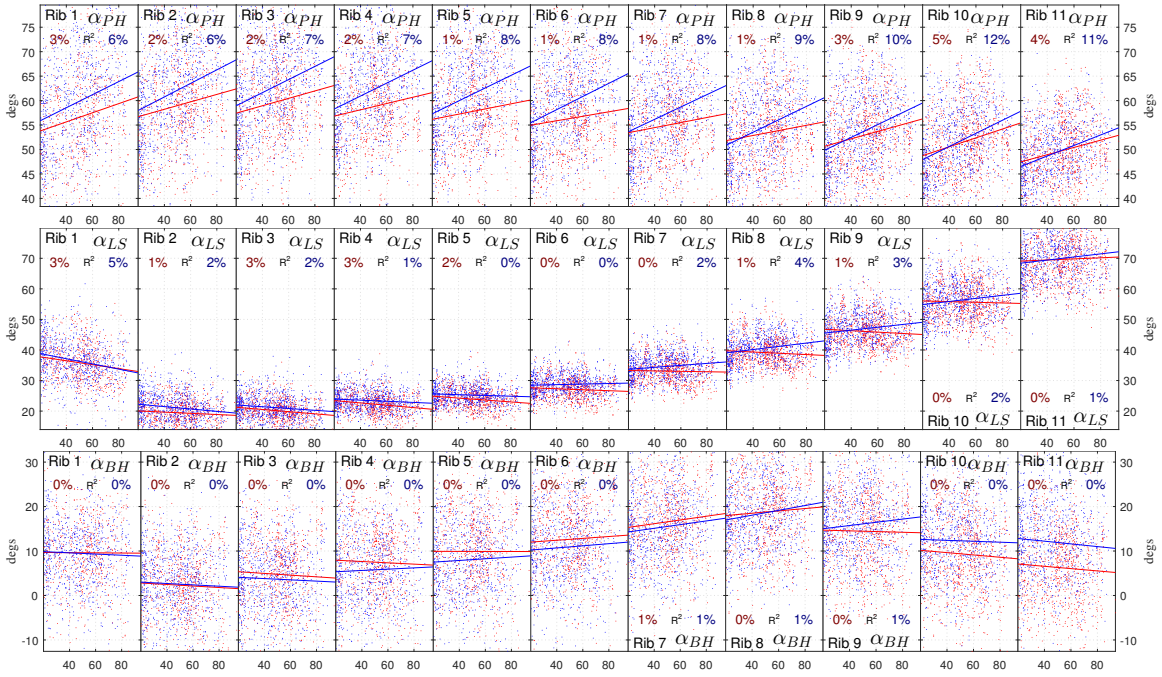

Figure 3.8: Data point cloud showing all rib pump-handle (α_{PH}), lateral swing (α_{LS}), and bucket-handle (α_{BH}) angle parameters between ages 20 and 90 years for males (blue) and females (red). Linear regression lines are included along with their explanatory power (r-squared).

show only marginal univariate trends with age, with a slight increase in ϕ_{pia} and decrease in B_p seen primarily in upper rib levels.

Rib pump-handle α_{PH} angles are given in Figure 3.8, with most ribs oriented between $40°$ (more vertically hanging, "narrow-chested") and $80°$ (closer to horizontal, "barrel-chested"). Age associations with α_{PH} are seen for both genders ($p < 0.001$, all ribs). However, the rate of change ($1.43°$ per decade for males at the 6$^{\text{th}}$ ribs, $0.43°$ for females) and the percentage of population variation explained by age alone ($8\,\%$ within males, $1\,\%$ within females) differ considerably.

The lateral swing α_{LS} parameter shows clear differences by rib level since different ribs extend closer to the sternum (α_{LS} near $20°$) in ribs 2 and 3, and finish more laterally with each successive rib level. In general only minor univariate trends with age are seen, with increased age associated with slight increases in α_{LS} angle for lower ribs in males. Similarly small univariate aging effects are seen in bucket-handle α_{BH} angles, with age

alone unable to explain more than $1\,\%$ of the overall population variance within either gender.

3.2.3 Multivariate regression models

The univariate analyses shown in Figures 3.7 and 3.8 highlight clear trends in a number of the model parameters with age, however they are not necessarily independent of confounding demographic variables such as height and weight which will also affect rib geometry. Multivariate linear regression was therefore performed for each rib and parameter using demographic variables of age, height, weight, and sex as predictors. Full model regression coefficients for all parameters are supplied in Table 3.4, while Table 3.5 gives the proportion of population variation within each parameter that is explained by the demographics predictors in each regression model.

Regression results show, for example, that a person's height is the most strongly correlated demographic with rib length (S_x), and that 6$^{\text{th}}$ rib length increases at a rate of $0.56\,\mathrm{mm}$ for each gained cm in stature ($p \ll 0.001$). Similarly, males will have 6$^{\text{th}}$ ribs S_x span $10.2\,\mathrm{mm}$ longer than females of equivalent demographics, and the isolated age effect on S_x is an elongation of $2.6\,\mathrm{mm}$ per decade ($p \ll 0.001$).

Aspect ratio, on the other hand, is most strongly related to an increase with age, with the peak of the 6$^{\text{th}}$ rib (Y_{Pk}) moving down towards the x-axis in the local rib plane at a rate of 0.01 normalized rib units per decade ($p \ll 0.001$). Sex and height have negligible influence on Y_{Pk} values for most ribs, while the independent effect of weight is to increase aspect ratio at a rate of 0.036 normalized rib units per $10\,\mathrm{kg}$ gained ($p \ll 0.001$).

Rib skewness is primarily influenced by age and height, with a movement of the 6$^{\text{th}}$ rib X_{Pk} coordinate towards the proximal end by about 0.005 normalized rib units per decade and 0.0005 units per cm gained in stature ($p \ll 0.001$). ϕ_{pia} differs significantly by gender, with female 6$^{\text{th}}$ ribs pointing initially $5.6°$ more posteriorly than male ribs. A less strong independent age and weight effect also exists whereby ribs increase in ϕ_{pia} by around $0.7°$

Table 3.4: In-plane rib shape model with parameter coefficients predicted by demographics. Age (A) is in years, sex (S) is 0 for males and 1 for females, height (H) is in meters, weight (W) is in kilograms, along with the regression intercept (I). Subscript denotes scale factor. For example, $W_{E\text{-}3}$ indicates weight in kg scaled by 1×10^{-3}. Coefficients significantly different from zero at the $p < 0.01$ level are shown in bold.

	S_x					X_{Pk}					Y_{Pk}				
#	I	$A_{E\text{-}3}$	$S_{E\text{-}1}$	$H_{E\text{-}1}$	$W_{E\text{-}3}$	$I_{E\text{-}3}$	$A_{E\text{-}5}$	$S_{E\text{-}3}$	$H_{E\text{-}3}$	$W_{E\text{-}5}$	$I_{E\text{-}2}$	$A_{E\text{-}5}$	$S_{E\text{-}3}$	$H_{E\text{-}3}$	$W_{E\text{-}5}$
1	**32**	**92**	**-23**	**189**	**38**	**408**	-21	3	-12	7	**63**	**-60**	-10	-38	-8
2	**56**	**124**	**-33**	**285**	13	**306**	15	-4	18	**-27**	**65**	**-80**	1	10	-9
3	**68**	**159**	**-38**	**398**	-15	**285**	**18**	**8**	**47**	**-40**	**60**	**-88**	-0	10	13
4	**82**	**187**	**-59**	**467**	-26	**337**	-6	4	4	**-27**	**55**	**-92**	2	1	**24**
5	**91**	**231**	**-91**	**519**	-23	**392**	**-24**	2	-38	-7	**52**	**-102**	8	-9	**28**
6	**97**	**260**	**-102**	**557**	**-42**	**399**	**-47**	-0	**-49**	7	**48**	**-109**	6	-15	**36**
7	**105**	**274**	**-102**	**572**	**-41**	**431**	**-69**	-3	**-73**	**16**	**43**	**-107**	1	-13	**39**
8	**93**	**236**	**-104**	**651**	-21	**470**	**-72**	-2	**-90**	**21**	**44**	**-89**	-5	**-37**	**35**
9	**83**	**184**	**-102**	**652**	4	**471**	**-62**	1	**-65**	**19**	**41**	**-77**	-4	-20	**29**
10	**66**	**178**	**-89**	**639**	**43**	**456**	**-51**	**-7**	**-36**	7	**38**	**-67**	**-10**	-12	**12**
11	**36**	**160**	**-80**	**646**	**53**	**521**	**-47**	**-15**	**-61**	1	**32**	**-55**	**-16**	-8	6
12	4	32	**-89**	**492**	**126**	**425**	**-45**	**-28**	-14	28	**10**	-7	-6	39	**18**

	ϕ_{pia}					B_p					B_d				
#	I	$A_{E\text{-}3}$	$S_{E\text{-}1}$	$H_{E\text{-}1}$	$W_{E\text{-}3}$	$I_{E\text{-}2}$	$A_{E\text{-}4}$	$S_{E\text{-}2}$	$H_{E\text{-}2}$	$W_{E\text{-}4}$	$I_{E\text{-}2}$	$A_{E\text{-}4}$	$S_{E\text{-}2}$	$H_{E\text{-}2}$	$W_{E\text{-}4}$
1	**82**	**66**	12	-12	-27	-73	19	2	16	-11	157	**93**	-4	-24	27
2	**119**	**58**	**30**	-52	**-28**	**-58**	-3	**6**	14	-1	12	**39**	-2	31	-15
3	**117**	**69**	**29**	-15	-21	**-30**	**-17**	1	-12	**10**	-24	13	6	37	**-15**
4	**112**	**78**	**37**	-4	-19	**-28**	**-18**	-1	-13	**12**	45	-9	2	-20	**-13**
5	**103**	**81**	**45**	47	**-34**	**-35**	**-17**	-2	-5	4	19	**-20**	-1	-28	1
6	**102**	**72**	**56**	55	**-57**	-22	**-13**	-2	-8	-1	10	**-27**	4	-28	-4
7	**100**	**69**	**60**	56	**-73**	**-46**	-4	-4	11	-5	-22	21	**19**	9	**-36**
8	**87**	**65**	**44**	**118**	**-88**	**-74**	-3	-4	**29**	-6	7	-3	**16**	1	**-43**
9	**82**	39	**42**	**113**	**-86**	**-60**	**-12**	-4	10	-0	56	**-28**	**13**	-15	**-39**
10	**72**	20	**27**	**142**	**-98**	0	**-18**	**-10**	**-38**	**21**	18	4	-3	-12	-9
11	**67**	11	**39**	**122**	**-80**	-52	**-30**	**-22**	-13	**34**	**224**	**87**	**27**	**-146**	35
12	**42**	-53	-16	132	12	-120	**63**	25	-23	-15	153	11	21	-45	52

	α_{PH}					α_{LS}					α_{BH}				
#	$I_{E\text{-}1}$	$A_{E\text{-}3}$	$S_{E\text{-}2}$	$H_{E\text{-}1}$	$W_{E\text{-}3}$	I	$A_{E\text{-}3}$	$S_{E\text{-}2}$	$H_{E\text{-}1}$	$W_{E\text{-}3}$	$I_{E\text{-}1}$	$A_{E\text{-}3}$	$S_{E\text{-}1}$	$H_{E\text{-}1}$	$W_{E\text{-}3}$
1	**767**	**98**	**-378**	**-240**	**230**	**30**	**-70**	-32	**100**	**-93**	89	-17	-2	**73**	**-106**
2	**781**	**99**	**-371**	**-244**	**252**	**16**	**-31**	**-134**	**64**	**-49**	100	-6	**-13**	-11	-21
3	**780**	**93**	**-367**	**-243**	**262**	**19**	**-32**	**-83**	**44**	**-44**	66	0	-1	8	**-29**
4	**763**	**88**	**-372**	**-236**	**263**	**24**	**-28**	**-117**	22	**-37**	97	11	2	0	**-41**
5	**749**	**86**	**-368**	**-236**	**268**	**29**	**-24**	**-156**	-3	**-25**	88	14	5	14	**-48**
6	**711**	**87**	**-323**	**-229**	**275**	**35**	-6	**-199**	-25	**-14**	106	**30**	5	23	**-66**
7	**713**	**87**	**-274**	**-237**	**266**	**40**	10	**-198**	-32	-6	85	**49**	2	63	**-86**
8	**669**	**85**	**-182**	**-221**	**254**	**45**	16	**-193**	-33	1	86	**55**	-7	**89**	**-115**
9	**670**	**92**	**-133**	**-220**	**235**	**56**	10	**-155**	**-62**	15	66	**30**	**-22**	**104**	**-129**
10	**603**	**104**	-87	**-181**	**205**	**69**	10	**-113**	**-97**	**44**	67	-14	**-30**	**102**	**-129**
11	**546**	**80**	-25	**-132**	**160**	**83**	24	-67	**-100**	**38**	42	-30	**-46**	**116**	**-120**
12	**632**	**54**	-121	**-118**	**95**	**116**	32	-72	**-118**	**-41**	142	-9	**-72**	102	**-161**

Table 3.5: Percentage of overall population variation per parameter explained (r-squared) by regression models to age, height, weight, gender.

#	S_x	X_{Pk}	Y_{Pk}	ϕ_{pia}	B_p	B_d	α_{PH}	α_{LS}	α_{BH}
1	23	0	4	3	0	2	30	12	9
2	22	2	7	8	1	2	36	10	1
3	22	5	9	8	6	1	41	10	0
4	27	2	11	9	6	1	43	9	2
5	35	2	16	11	3	1	47	8	2
6	38	4	20	12	1	2	50	5	5
7	39	9	23	11	1	5	50	3	8
8	46	10	21	7	2	5	48	3	12
9	50	8	19	6	1	5	48	1	16
10	49	7	16	4	3	-0	47	3	17
11	35	7	14	3	8	5	40	2	17
12	12	3	4	1	1	0	7	2	8

per decade and decrease by $0.6°$ per added $10\,\mathrm{kg}$.

Using the full model parameters presented in Table 3.4 we can predict the expected set of six shape parameters per rib for a person of a known demographic. With those parameters we then apply them back to the parametric shape model to generate that demographic's expected rib geometry. For example, Figure 3.9 shows the expected geometric rib shapes determined by the regressed model parameters that are typical for three females and three males of 50 years of age with heights and weights equal to the 5$^{\text{th}}$, 50$^{\text{th}}$, and 95$^{\text{th}}$ percentile height and weight for their respective genders.

This same approach is used to illustrate the aging effect on rib shapes in Figure 3.10. Here, just one stature demographic is held constant (50$^{\text{th}}$ percentile female) and person age is varied from 20 to 90 years at 5-year increments. From this figure it is clear to see the effect of elongation of the rib span (with the 6$^{\text{th}}$ rib S_x progressing from $179\,\mathrm{mm}$ to $197\,\mathrm{mm}$) coupled with an increase in overall aspect ratio (Y_{Pk} shifting from 0.31 to 0.28 in normalized rib coordinates).

Similarly, Figure 3.11 shows the expected change in rib shapes due to weight. A 50-year-old, $162\,\mathrm{cm}$ tall female baseline is used, and weight is varied from $40\,\mathrm{kg}$ to $175\,\mathrm{kg}$. The results show that rib shape changes primarily in the mid-to-lower ribs, with expansion

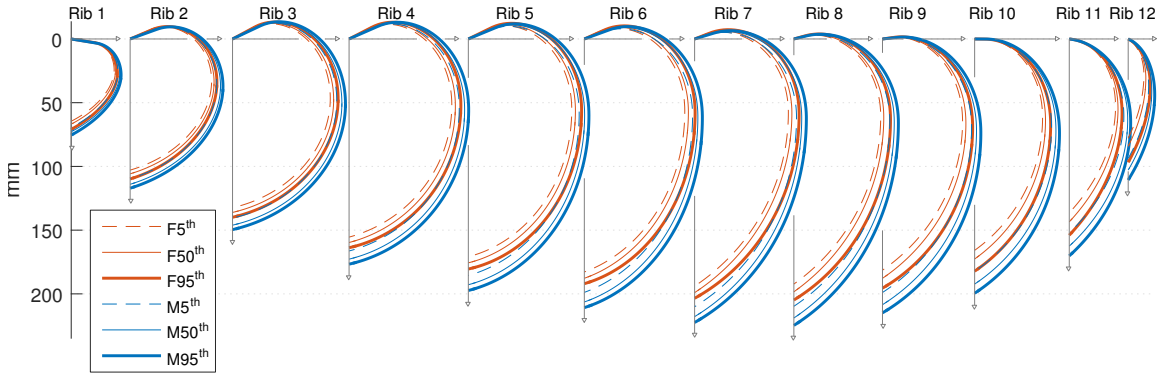

Figure 3.9: Predicted in-plane rib shapes by demographic for small, medium, and large (5^{th}, 50^{th}, and 95^{th} percentile weight and stature) males and females, all at 50 years of age.

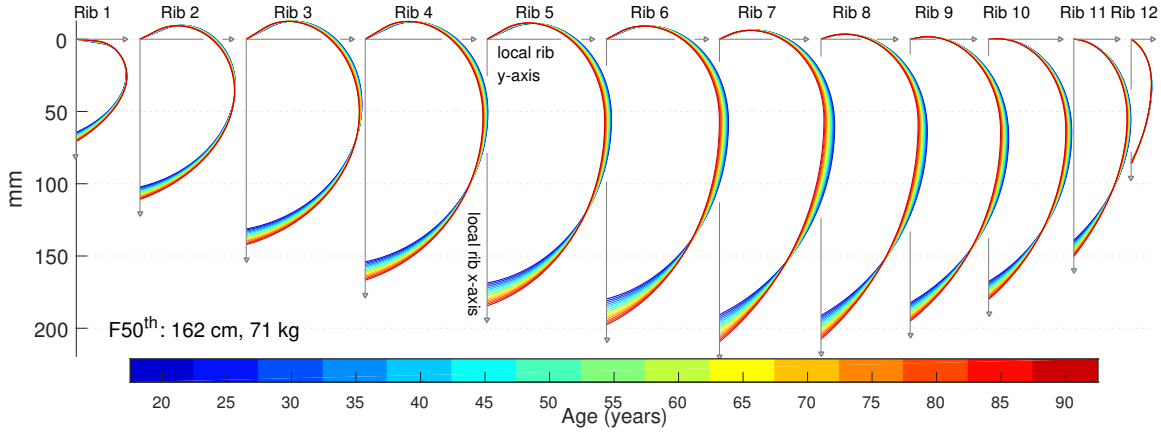

Figure 3.10: Predicted in-plane rib shapes by age. Baseline demographic is the 50^{th} percentile female with specific age represented by line color. Ribs become more elongated and increase in aspect ratio with age.

of the lateral rib aspects as weight is gained. The maximum physical separation between the expected rib shapes for the $40\,\mathrm{kg}$ and $175\,\mathrm{kg}$ individual in this figure occurs at the antero-lateral region of the 8^{th} rib, where the rib paths differ by up to $9\,\mathrm{mm}$ in the local rib plane. Figure 3.12 illustrates the height effect using again a 50-year-old female baseline ($71\,\mathrm{kg}$), with her height adjusted along the range seen throughout the female population. Here the expected effect of increasing height is, understandably, to increase overall rib size as each incremental rib in Figure 3.12 shows clearly.

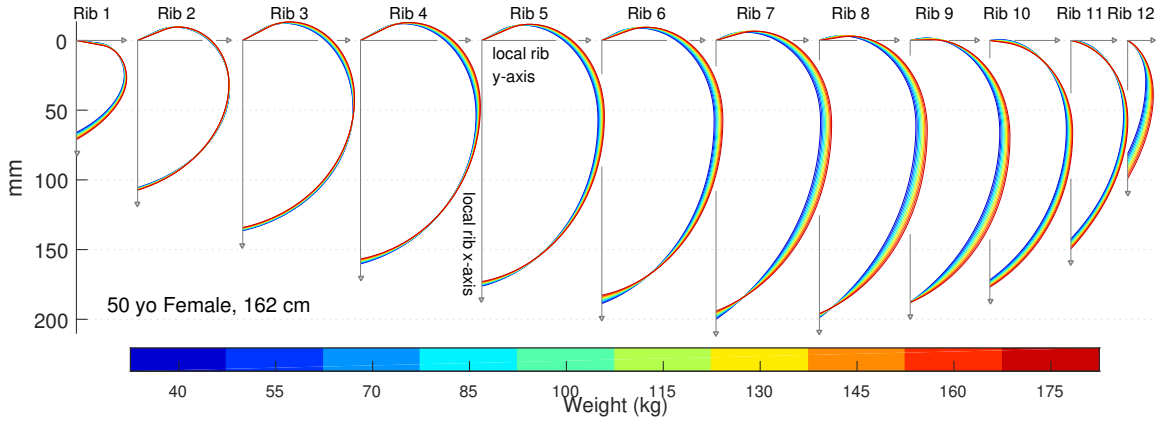

Figure 3.11: Predicted in-plane rib shapes by weight. Baseline demographic is a 50-years female of $162\,\mathrm{cm}$ stature, with specific weight represented by line color. Ribs in heavier individuals are rounder, having lower aspect ratio (higher Y_{Pk}).

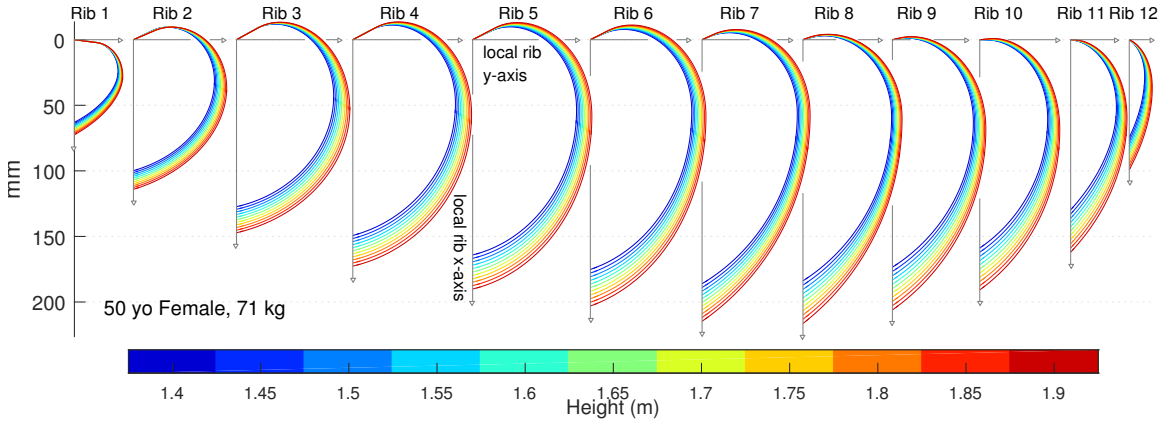

Figure 3.12: Predicted in-plane rib shapes by height. Baseline demographic is a 50-years female of $71\,\mathrm{kg}$ weight, with specific height represented by line color. A clear size effect is seen whereby S_x increases with person height.

3.2.3.1 Testing model accuracy via indirect parameters

The results seen in Figure 3.10 show the changes in rib shapes built from sets of shape model parameters that are themselves predicted by regressions to specific demographics (in this case females of 50^{th} percentile height and weight and of various ages). In that sense, all regressed parameters including the direct geometric measures of rib size (S_x), aspect ratio (Y_{Pk}), skewness (X_{Pk}), and proximal inner angle (ϕ_{pia}) match the estimated central value for the supplied demographic, at least to the accuracy of the regression models.

However, this does not guarantee that any derived measures of shape (i.e., those not

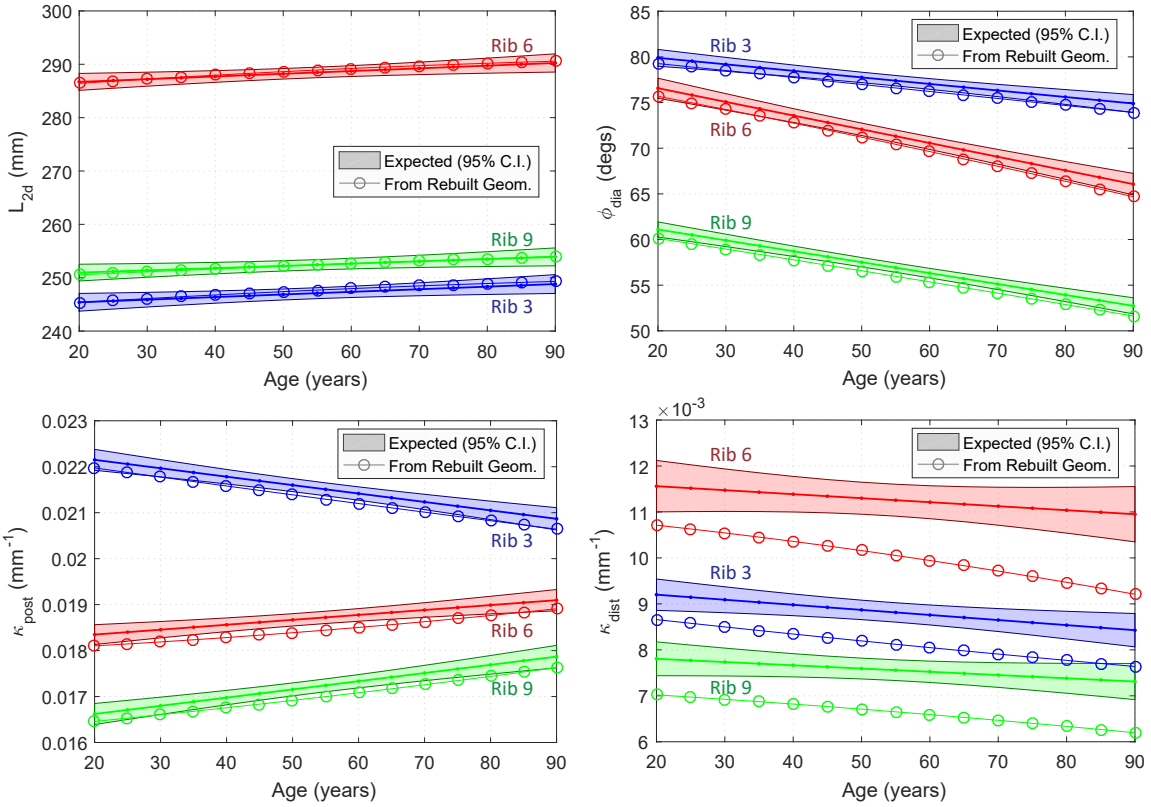

Figure 3.13: Expected values for rib arc length (L_{2d}), inner angle at the distal end (ϕ_{dia}), and local curvature at posterior (κ_{post}) and distal (κ_{dist}) locations, along with values from rebuilt ribs matching that demographic. Regression models fitted to the values measured directly in the population are used to query for the expected values (with $95\,\%$ confidence interval) for 50^{th} percentile females of varying ages.

explicitly regressed to as model parameters) will also reflect the typical values for a given demographic. For example, the inner angle at the distal end (ϕ_{dia}) is a rib shape measure which, when measured directly from all ribs in the population, is seen to decrease with age ($p < 0.001$ for all rib levels). The extent to which reconstructed rib shapes reflect such trends seen in indirect parameters – when using ribs that are rebuilt by sets of predicted parameters with different ages as input to regression – serves to test the suitability of the model presented here to produce geometry that truly reflects overall population trends.

This comparison is illustrated in Figure 3.13, which shows both expected values (via regression to demographics of the values measured directly from ribs in the population) and obtained values (via rebuilt ribs using predicted parameter values for that demographic) for

each of the four indirect shape measures. The displayed demographic series is from 50th percentile females, with each observation matching one rib shape from the series of F50 ribs that were shown in Figure 3.10. Corresponding figures for results from small female and large male baseline demographics (F05, M95) are given in Figures 3.14 to 3.17 on the following pages.

Results in Figure 3.13 show that the reconstructed ribs have equivalent length (L_{2d}) to the expected rib length seen in the population. Trends in inner angle at the distal end (ϕ_{dia}) and rib curvature at the posterior region (κ_{post}) also match well to the expected population values, with only marginally lower values in reconstructed ribs than expected based on measures from the given population. Rib curvature at the distal end shows the largest divergence from population results, with reconstructed ribs having around $10\,\%$ lower curvature at this distal extremity than is expected, particularly at the 6th rib level in an older population.

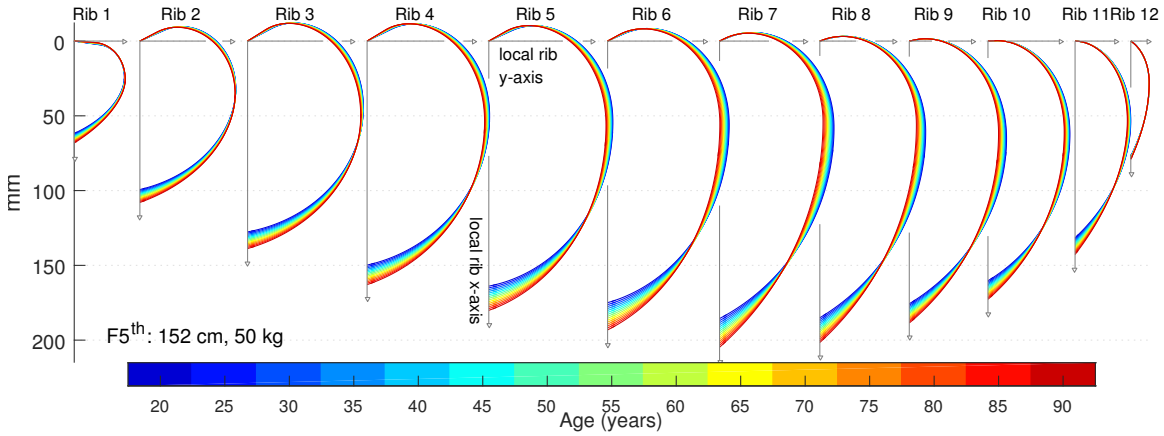

Figure 3.14: Predicted in-plane rib shapes by age. Baseline demographic is the 5th percentile female with specific age represented by line color. Ribs become more elongated and increase in aspect ratio with age.

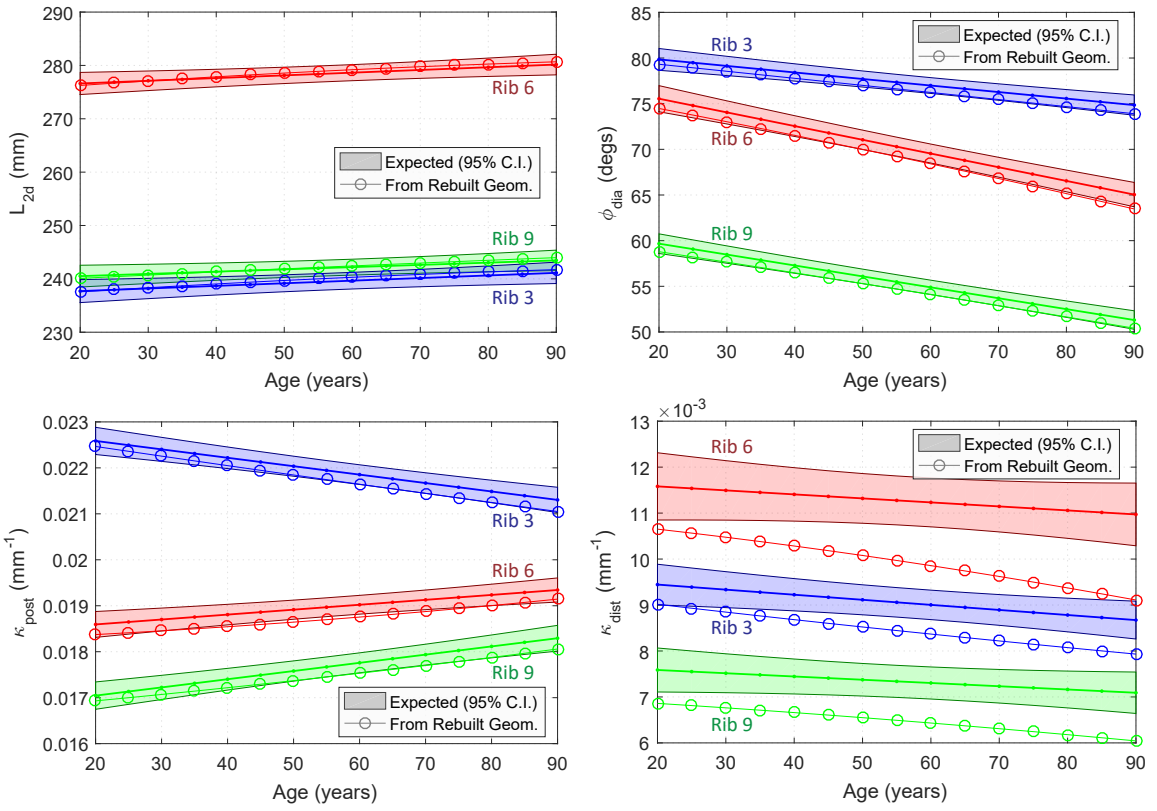

Figure 3.15: Expected values for rib arc length (L_{2d}), inner angle at the distal end (ϕ_{dia}), and local curvature at posterior (κ_{post}) and distal (κ_{dist}) locations, along with values from rebuilt ribs matching that demographic. Regression models fitted to the values measured directly in the population are used to query for the expected values (with 95 % confidence interval) for 5th percentile females of varying ages.

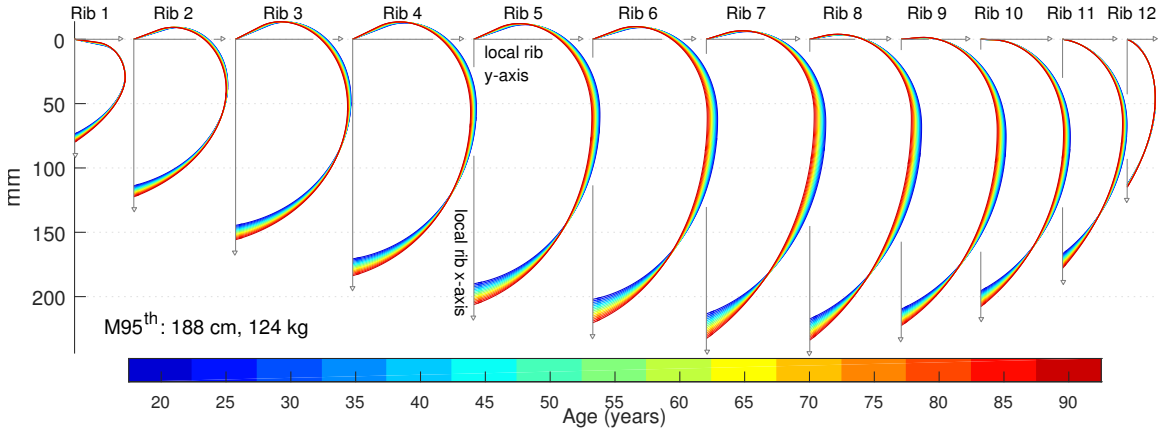

Figure 3.16: Predicted in-plane rib shapes by age. Baseline demographic is the 95th percentile male with specific age represented by line color. Ribs become more elongated and increase in aspect ratio with age.

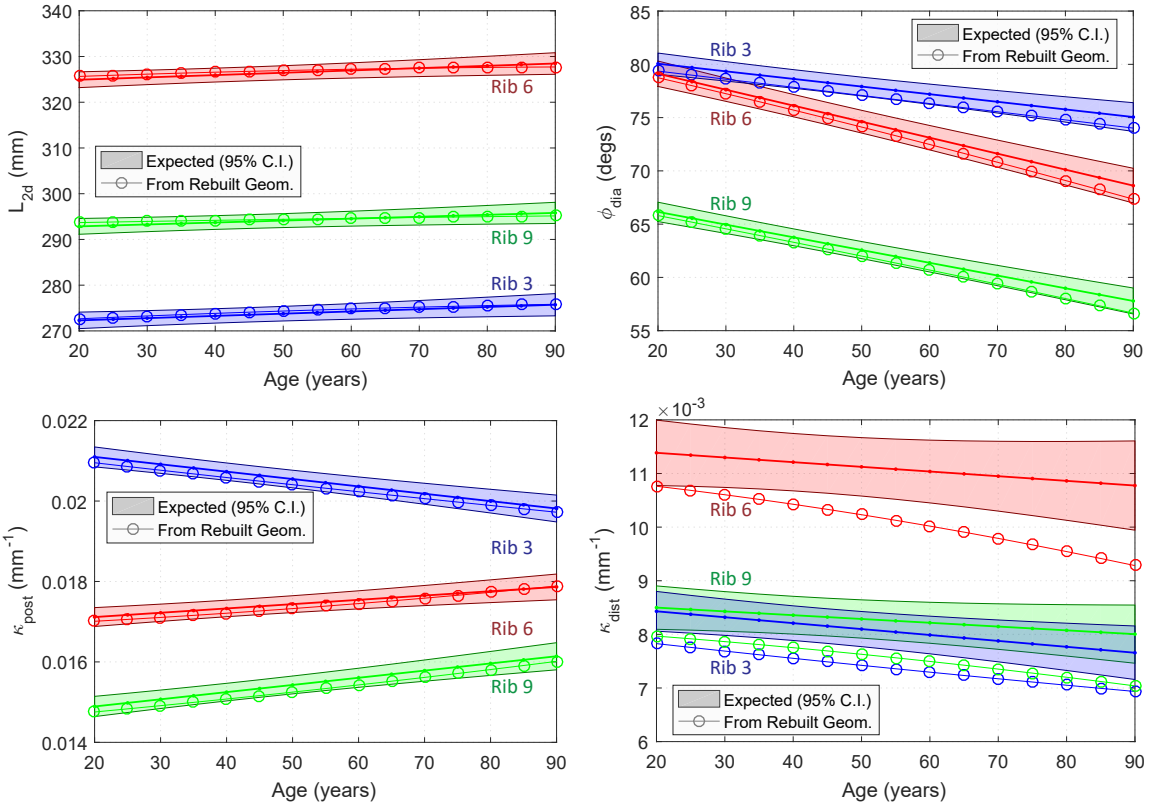

Figure 3.17: Expected values for rib arc length (L_{2d}), inner angle at the distal end (ϕ_{dia}), and local curvature at posterior (κ_{post}) and distal (κ_{dist}) locations, along with values from rebuilt ribs matching that demographic. Regression models fitted to the values measured directly in the population are used to query for the expected values (with 95 % confidence interval) for 95th percentile males of varying ages.

3.3 Discussion

This study has applied a parsimonious model of in-plane rib shape and rib orientation measures to a large adult population to quantify its variation and, in particular, investigate the changes in rib anatomy that occur with age. Univariate (age) and multivariate (age, height, weight, sex) regression models for parameters are compared in terms of their explanatory power and the multivariate models are used to produce typical or expected rib shapes for particular demographics.

3.3.1 Rib shape model considerations

A feature of the shape model introduced in Chapter 2 and Holcombe et al. (2016) is that four of its six parameters are themselves inherent geometric measures of rib geometry. This provides an advantage over other generalized methods of rib cage shape analysis such as GPA or PCA – which parameterize the position of a large cloud of points – by ensuring that the shape model's regression coefficients for demographic factors are themselves directly meaningful and easily understood. For example, the negative coefficients for age in the Y_{Pk} parameter of Table 3.4 give clear evidence of increasing aspect ratios in ribs throughout adulthood. The shape model also provides a more concise set of parameters than would otherwise be obtained using point cloud data, and results show that these parameters have low inter-dependence and are normally distributed across the population, lending validity to subsequent regression analyses.

Another important aspect of the shape model is its accuracy in representing the underlying geometric rib data. The mean absolute error (MAE) between a target rib point and its fitted shape model was $0.41\,\mathrm{mm}$. For comparison to past literature, Kindig's 7-parameter geometric model based on a circle and a semi-ellipse (Kindig and Kent, 2013) reported an MAE of $0.78\,\mathrm{mm}$ indicating that, on average, the spiral model used here reduces geometric fitting error by approximately $40\,\%$.

Measures of curvature using the shape model from this study showed strong agreement with previously published results. Mohr et al. (2007) reported average curvature of $0.017\,\mathrm{mm}^{-1}$ at the posterior regions of mid-level ribs while Dansereau and Stokes (1988) reported maximum curvature along the whole rib between $0.018\,\mathrm{mm}^{-1}$ and $0.033\,\mathrm{mm}^{-1}$. In this study the average κ_{post} values for ribs 3–9 fell between $0.017\,\mathrm{mm}^{-1}$ and $0.021\,\mathrm{mm}^{-1}$. At the distal end of the ribs, average κ_{dist} values in this study ranged from $0.007\,\mathrm{mm}^{-1}$ to $0.011\,\mathrm{mm}^{-1}$, which is similar to the range of $0.006\,\mathrm{mm}^{-1}$ to $0.008\,\mathrm{mm}^{-1}$ reported by Mohr et al. (2007).

3.3.2 Rib changes by demographics

This study attempts to identify specific effects of age on overall rib shape and orientation. Increases in rib pump-handle α_{PH} angle have previously been noted as an aging effect (Gayzik et al., 2008; Kent et al., 2005b), and results from this study do confirm that association. However, results also describe novel and significant changes in rib shape. The sections below will discuss the relative sensitivity of these two effects to age and other demographic factors.

3.3.2.1 Rib orientation with age and weight

When considering rib orientation, univariate regression by gender of α_{PH} angle to age shows a stronger relationship in males than in females, with both the rate of change and the proportion of population variance that age can explain ($8\,\%$ at rib 6 compared to $1\,\%$) being larger. When all demographic variables are used in multivariate regression the explanatory power increases substantially to around $50\,\%$ of the overall population variance for mid-level ribs. Notably, the inclusion of one-way interaction terms to the regression analysis offered little additional predictive power (less than $1\,\%$ for all ribs), indicating that after accounting for weight and stature in the multivariate analyses, gender-dependent age effects (such as were present in univariate analyses) were minimal. The relative contributions of

age and weight on α_{PH} angle can be investigated through the model coefficients reported in Table 3.4. In general older individuals, heavier individuals, shorter individuals, and males can be expected to have more "barrel-chested" rib angles than their counterparts ($p < 0.001$ in all ribs for age, height, weight, and $p < 0.01$ in ribs 2–8 for gender). The average population α_{PH} angle at the 6$^{\text{th}}$ rib is $57.8°$ and its standard deviation is $8.6°$. Comparatively, the expected change in α_{PH} across the whole age spectrum (i.e., between a 20-year-old and 90-year-old) is $6.9°$, or $0.8\,\text{SD}$ from population measures of α_{PH}. That same $6.9°$ change brought about by a 70-year age differential is also brought about by a $25\,\text{kg}$ increase in weight (equal to around $1\,\text{SD}$). In other words, the difference in α_{PH} seen two between adults at opposite ends of the age spectrum (but with other demographics similar) will be much smaller than the difference in α_{PH} between a light person and a heavier person of similar age.

3.3.2.2 Rib shape with age

A more direct aging effect is highlighted in Figure 3.10 whereby older ribs elongate in end-to-end span and adopt a shallower overall curvature. These changes are reflected in the age coefficients for the S_x and Y_{Pk} parameters of Table 3.4. The independent effect of age is to increase rib S_x span by up to $2.7\,\text{mm}$ (7$^{\text{th}}$ rib, $p < 0.001$ for ribs 1–10) for every added decade. As a result, across a 70-year adult lifetime an individual of average stature is likely to see the separation between ends of their longest ribs expand by $2.7\,\text{cm}$, or approximately $13\,\%$. This elongation is coupled with increases in rib aspect ratio, with Y_{Pk} being significantly associated with age for ribs 1–11 ($p < 0.001$ in ribs 1–10). The result of this association is that the rib peak moves progressively closer to the x-axis of the local rib plane at a rate of between 0.006 (ribs 1 and 10) and 0.010 (mid-level ribs) normalized rib units per decade. For perspective on these primary aging effects, a 70-year age difference reflects 6$^{\text{th}}$ rib changes in Y_{Pk} that amount to $1.5\,\text{SD}$ from population distributions in Y_{Pk}, and changes in S_x that amount to $1.1\,\text{SD}$ from population distributions in S_x. Each of

these shape effects are more strongly associated with age than the $0.8\,\mathrm{SD}$ changes seen in α_{PH}. The relative sensitivity of each of these parameters to age is presented graphically in Figure 3.18.

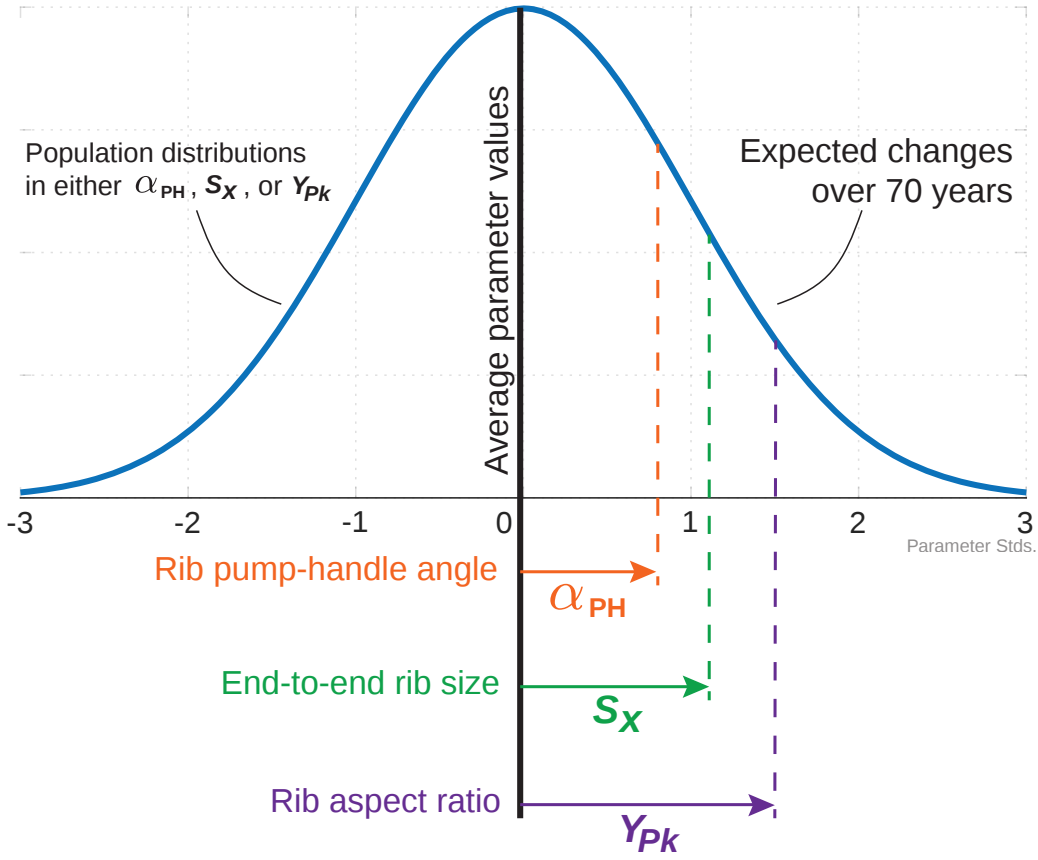

Figure 3.18: The relative sensitivity of 6th rib angle (α_{PH}) and rib shape parameters (S_x,Y_{Pk}) to age. Shape parameters are seen to be more strongly linked to the independent effect of age.

Other independent associations with age tend to be less strong and affect a more limited region of the rib cage. For instance, an age effect on rib skewness is most prominent at mid to lower level ribs (reductions in X_{Pk} of between 0.002 and 0.007 units per decade), whereas age influences ϕ_{pia} angle more prominently in mid to upper level ribs (increasing by around $0.7°$ per decade). In the case of ϕ_{pia} there is also a clear gender effect, with females having higher ϕ_{pia} angles than males of equivalent demographics by up to $6.0°$ ($p < 0.001$). Gender differences are most clearly distinguished by overall rib size, with S_x

is seen to be between $2.3\,\mathrm{mm}$ (1^{st} rib) and $10.4\,\mathrm{mm}$ (8^{th} rib) longer in males than females of equivalent demographics. Person height is also strongly correlated with S_x, with each additional $1\,\mathrm{cm}$ in stature corresponding to $0.2\,\mathrm{mm}$–$0.6\,\mathrm{mm}$ extension of S_x at each rib ($p < 0.001$). Weight is the only demographic variable other than age that is independently associated with aspect ratio, whereby a small increase is seen in Y_{Pk} for ribs 4–10 of 0.001 to 0.004 normalized rib units per each added $10\,\mathrm{kg}$. In general there are few trends that are both statistically significant and consistent across series of rib levels when considering the B_p and B_d spiral constants. Only in B_d do we see decreasing values for ribs 2–11, however these are only marginally significant ($0.03 < p < 0.05$) for ribs 3–6 and 9–11.

Overall, each of the differences that are seen in Table 3.4 have an accumulated effect to influence rib shape in multiple ways across demographics as depicted by Figures 3.9 to 3.11. The particular aging effect of elongation coupled with increased aspect ratio is consistent with Shi et al. (2014) who reported an increase in the whole rib cage AP depth with age that was associated with a decrease in rib cage width especially in the middle of the rib cage. To the best of our knowledge this is the first study to directly identify these effects as shape changes to the ribs that are independent of other thoracic changes, and the first to quantify both the shape changes themselves and also the ability of demographics-based regression to represent the overall population variability. For context regarding the question of whether the changes identified in this chapter actually serve to increase overall rib length with age (i.e., new bone modeling after supposed skeletal maturity) rather than simply reshaping bone that is already present, the reader is directed to Chapter 5 where analysis of the corresponding out-of-plane deviation is presented.

3.3.3 Limitations

The resolution of the CT scans used in any medical imaging study poses a limitation on accuracy when extracting underlying geometry. The majority of CT scans in this study had a slice spacing of $1.25\,\mathrm{mm}$ with an overall range from $0.625\,\mathrm{mm}$ to $5\,\mathrm{mm}$. In-plane scan

resolutions were between $0.54\,\mathrm{mm}$ and $0.98\,\mathrm{mm}$ with a median of $0.70\,\mathrm{mm}$.

The shape model investigated here is focused on the central axis of the rib and does not capture cross-sectional geometry or other changes in rib cortical surfaces that may vary across the population. This is itself a limitation in terms of the results that are reported in this study, however it also serves to alleviate problems with scan resolution since overall rib cross-sections (from which the central axis is derived) are structures many times larger than pixel sizes in even the lowest resolution scans.

The population itself is large compared to previous studies of rib and rib cage shape and carries data from 1000 live subjects. While study demographics match well to the general US population, it should be noted that subjects are sampled from one region of North America and individual ethnicity was not considered. Therefore care should be taken when extending results to different regional populations.

The CT scans were taken under a trauma protocol having the patients hold their breath during the image capturing sequence meaning results reported here are for a condition of maximal lung inspiration. It is expected that some patients may have difficulty adhering fully to this protocol, particularly those with chest injuries. This could lead to variations in measured rib angle from an otherwise healthy population due to expected differences throughout a respiratory cycle (Bellemare et al., 2001, 2003).

Rib pump-handle α_{PH} angles are reported with respect to the scan coronal plane or scanning bed. However, spine posture varies throughout the population. Since ribs articulate directly with the spine, kyphosis seen in some portions of the elderly population (Bartynski et al., 2005) would serve to lower α_{PH} angles in those individuals. This difference should be accounted for when comparing the current results to measures of independent orientation of ribs with respect to a curved spine, rather than the fixed reference plane used here.

The inner organs and other internal anatomy of the chest is asymmetrical, which would in turn lead to some degree of asymmetry between left and right sided rib anatomy. Small

but statistically significant differences in X_{Pk} and ϕ_{pia} parameters across sides were observed, indicating some nominal difference in skewness between ribs on the left and right sides of the body. With the goal of this study being to describe the more substantial variations seen across demographics however, ribs from left and right sides were pooled and results reported by rib level only.

Finally, the comparison of live population trends to the trends seen in rebuilt ribs shows that care should be taken when using the demographics-based regression model in applications that are strongly dependent on the local curvature at the distal end of the rib (κ_{dist}). The regression models for each direct parameter (size, aspect ratio, skewness, inner angle at the proximal end) ensure a central estimate is obtained for a given demographic, and results also show that indirect measures of rib length, distal inner angle, and posterior rib curvature are very well represented when recreating ribs from these regressed parameters. However, the indirect property of distal rib curvature (κ_{dist}) is seen to be slightly underestimated by recreated rib shapes when compared to the true curvature seen directly in the population.

3.3.4 Conclusions

A statistical model of the human rib shape and orientation in the body was developed that accounts for variations by age, height, weight, and sex. The size and shape of ribs were represented using the six-parameter shape model which was applied to 1000 subjects and multivariate regression was used for a predictive model of typical rib geometry based on demographic factors. All demographic factors had statistically significant effects on rib shape and orientation, with height and gender being most strongly associated with rib size and weight being most strongly associated with rib pump-handle angle. The primary effect of age was on a unique aspect of rib shape, with older ribs being more elongated and having flatter overall curvature than younger ribs. Study results include a statistical rib shape model that gives the geometric basis for building ribs that are typical for any specific

demographics group. This can be used to enhance computational modeling of the thoracic rib cage by improving the fidelity of rib geometry, particularly when that geometry is being designed or modified to match particular demographic groups.

CHAPTER 4

The influence of shape on mechanical properties

In this chapter we expand our focus beyond just geometric shape changes and begin investigating the mechanical consequences of those changes. Chapter 2 introduced a rib new shape model, and Chapter 3 applied it to a large adult population showing the expected changes in shape with age and other demographics. Here we use that information to simulate idealized loading of FE rib models from both the original live population, and also from representative ribs that have been rebuilt based on the demographics-driven regression models. The key features of interest for each rib in this chapter are its stiffness (i.e., its ability to resist deformation) and the distribution of stress that occurs along its length during loading. The primary aim of the chapter is to address the question of whether the shape changes that have been associated with aging will have have mechanical implications that change their response to loading. We also consider the more general question of which rib shapes are stiffest and softest under various loading conditions, and look to convey that information in a way that is useful to researchers performing physical testing.

4.1 Mechanical modeling and simulation

4.1.1 Simulated rib geometry sets

Three sets of rib geometries are utilized in this chapter, with each set built using rib shape model parameters either fitted directly to real rib data, or artificially generated using

the linear regression models (to age, height, weight, gender) presented in Chapter 3.

The first set of geometries came directly from the same 1000 adults (22,692 individual ribs) that comprised the study population introduced in Chapter 3. The second set of geometries are related to these same 1000 individuals, but instead of using their original rib shapes we will use shapes that are rebuilt via regression (from coefficients in Table 3.4 of Section 3.2.3) to those individuals' demographic factors. This second set is used only briefly in this chapter in order to test how well the regression models to demographics can predict the mechanical responses seen from the original rib geometries. The third set of rib geometries match no specific individuals. Instead, they are rebuilt from demographics-based regression (again, Section 3.2.3) using specific body heights, weights, and genders. The demographic specifications come from six series – a series each for small, medium, and large males and females – who have their ages varied from 20 to 90 years at 5-year increments. Specifically, each series will be designated by its gender and its height and weight percentile, such as F05 (small female series from young to old), M95 (large male series), and so on. The baseline demographic factors for each series were chosen to match CDC population percentiles, and are reproduced for convenience in Table 4.1.

Table 4.1: Demographics of representatives for each series of recreated rib shapes.

Representative	$\%_{\text{ile}}$	Sex	Height (cm)	Weight (kg)
F05	5^{th}	F	152	50
F50	50^{th}	F	162	71
F95	95^{th}	F	174	114
M05	5^{th}	M	163	62
M50	50^{th}	M	176	86
M95	95^{th}	M	188	124

4.1.2 Simulation setup

As was first presented in Section 2.4.3, FE models of ribs were created from overall rib shapes and simulations of their mechanical properties were performed using LS-DYNA

(Livermore Software Technology Corporation). Simulated conditions include those similar to a number of experimental studies of isolated ribs subjected to external loading. It should be made clear at the outset that the simulations used here are not designed to optimally model the overall mechanics of those experiments. Instead, they are intended only as a tool for exposing the relative changes in mechanical properties that come as a result of variations in overall rib shape. For a more detailed model aimed at replicating experimental results, the reader is recommended to refer to Li et al. (2010).

4.1.2.1 Rib geometric meshing and materials

Using in-plane rib geometry as the centroidal axis, each tested rib was modeled using 2-D shells forming a cylindrical mesh of constant $5\,\mathrm{mm}$ radius around the central axis. A custom MATLAB function was built to produce rib geometry consisting of 100 equally sized shell elements along its length and 12 elements around its circumference as depicted in Figure 4.1.

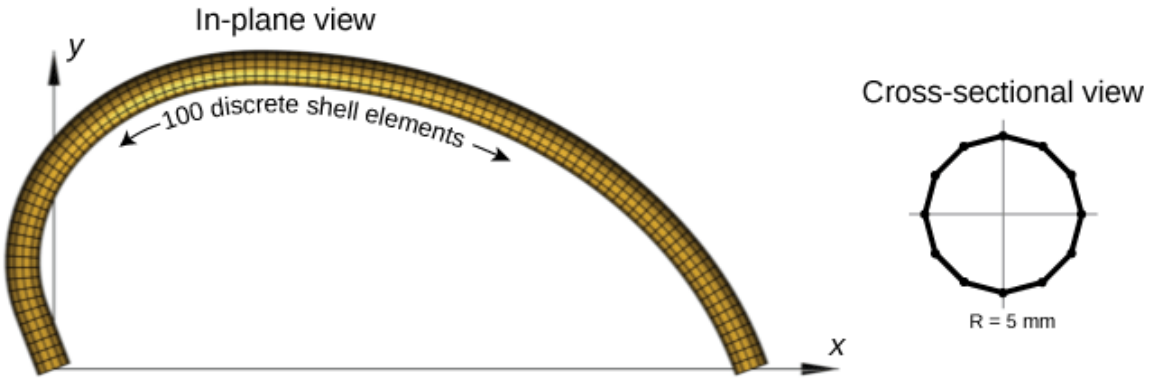

Figure 4.1: Simulation geometry and mesh overview showing the cylindrical shell mesh around a rib's centroidal path.

A simple linear elastic material model was used as first described in Section 2.4.3, with material properties shown below in Table 4.2.

Table 4.2: Elastic material and shell element properties used in all rib simulations.

ρ (kg/m^3)	E (GPa)	ν	Shell thick. (mm)
2000	11	0.3	1.0

4.1.2.2 Boundary conditions and load cases

With a cylindrical rib mesh in place, a `NODAL_RIGID_BODY` was formed using the ring of nodes at each end of the rib allowing point constraints to be placed on the center of mass of these rigid bodies to be transferred smoothly to the rib's deformable shell elements.

In all loading cases the proximal end was constrained against translation in all 3 directions and against rotation around the local rib x- and y- axes, allowing only a single degree of rotational freedom about the out-of-plane z-axis. The distal end was similarly constrained in rotation, but an additional degree of translational freedom was allowed in certain loading conditions (see below) along the local x-axis.

Simulations were performed under each of four separate loading conditions as illustrated in Table 4.3, which identifies loading directions and reaction force measurements. The first loading condition (referred to henceforth as axial compression) represents uniaxial loading along an axis passing through the rib ends. In a frontal motor vehicle crash, this loading orientation is similar to that experienced as the chest is restrained by a seatbelt. This condition is also functionally similar to a number of physical experiments performed testing individual ribs (Charpail et al., 2005; Daegling et al., 2008; Kindig et al., 2011; Kindig and Kent, 2013; Agnew et al., 2015).

A second loading condition (constrained axial compression) places an additional constraint via a rigid wall above the rib in its in-plane orientation. This condition is chosen to represent some form of lateral constraint to a body (from, say, contact with the vehicle door) while body-anterior loading is experienced. The third loading condition (lateral compression) represents loading to the body from a lateral direction, whereby the isolated rib is loaded along the y-axis of its local rib plane. Finally, a constrained lateral loading

condition was chosen to represent a combination of body-anterior and body-lateral loading.

It is clear that the real-world loading conditions within MVCs are more complex than these four idealized representations. It is also understood that even controlled laboratory testing cannot fully reproduce these conditions as they often require potting of rib ends or other forms of fixation. Nevertheless, these idealized conditions are chosen to represent some of basic modes of deformation that ribs may experience during loading to the body, and to do so as simply as possible in order to retain sensitivity of the model setup only to overall shape.

Loading in all cases was applied in a quasi-static fashion over a $150\,\mathrm{ms}$ simulation time. To help remove any dynamic effects, nodal velocity was prescribed using a velocity ramp curve which provided gradual displacement as illustrated in Figure 4.2. Resulting force measures were checked for inertial artifacts such as ringing or settling time (via test simulations with abruptly ceased displacements) and were found to be consistent with the intended condition of quasi-static loading.

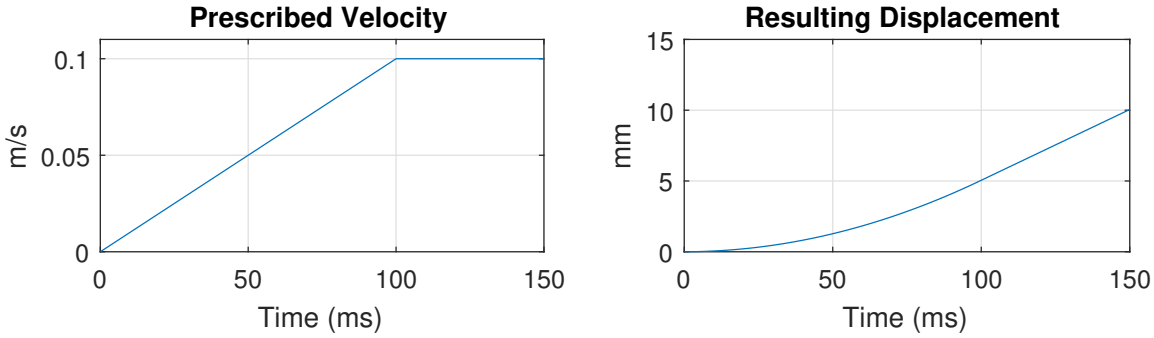

Figure 4.2: Simulation loading curves showing specified boundary conditions at the loaded rib location.

Stiffness to any given loading condition was determined by the initial slope of the force vs. displacement relationship. To calculate this, a best-fit line was applied to these measures taken between absolute displacements of $0.15\,\mathrm{mm}$ and $6\,\mathrm{mm}$ for axial compression, and $0.1\,\mathrm{mm}$ and $4\,\mathrm{mm}$ for axial compression.

Table 4.3: Simulation loading and boundary conditions.

	**Axial compression** Rib fixed at proximal end by pivot joint, and at distal end by sliding pivot joint. Linear displacement along x-axis applied to distal end. Reaction force measured at distal end.
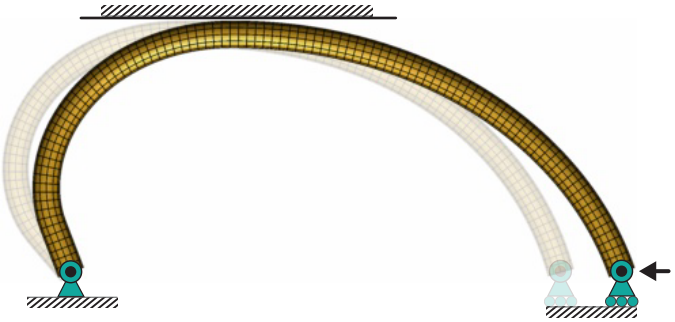	**Constrained axial compression** In addition to axial compression conditions, a frictionless rigid wall is placed immediately above the rib constraining vertical displacement during axial compression. Reaction force measured at distal end.
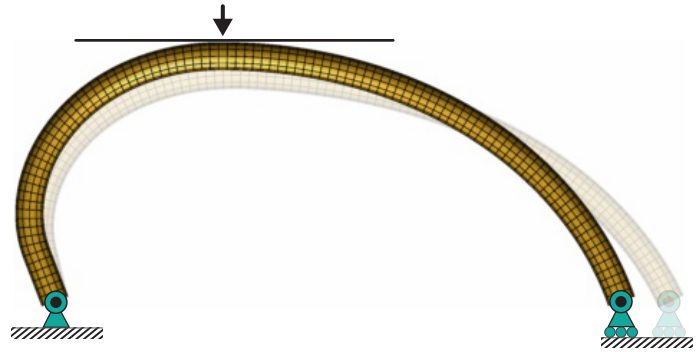	**Lateral compression** A moving flat rigid wall applies vertical displacement from above. Rib fixed at the proximal end by a pivot joint, and at distal end by a sliding pivot joint. Reaction force measured at wall.
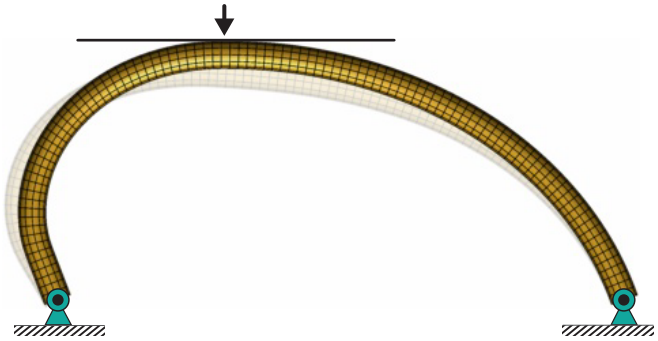	**Constrained lateral compression** Both rib ends constrained by pivot joints, with moving rigid wall contacting rib shape from above. Reaction force measured at wall.

4.2 Results

All individuals' ribs were subjected to each of the four simulated loading conditions. Stiffness to each loading type was recorded, along with the position and value of maximum von-mises stress along each rib during deformation.

4.2.1 Population stiffness results

Stiffness results by age and sex for all loading conditions are shown for ribs 2 to 9 in Figure 4.3. Here, scattered outcome data is plotted against age for each rib, and the univariate trend with age shown by a regression line each for males and females. The proportion of overall variation in stiffness that is explained by linear regression to age alone is included for each rib.

In axial compression (K_{ax}), there is a consistent trend across all ribs whereby stiffness increases due to the shape changes that come from age ($p < 0.001$). This trend is clearest (r-squared = $14\,\%$ for females, $9\,\%$ for males) at the 7$^{\text{th}}$ rib level. The added frictionless wall at the apex of ribs in constrained axial compression (K_{axCon}) leads to a stiffer overall response, with an average increase of 3.4 times the stiffness seen in simple axial compression. Similar trends with age are seen whereby stiffness increases significantly for males and females ($p < 0.001$). The explanatory power of age alone, however, is relatively weak with up to $7\,\%$ of variation in females explained by age, and up to $4\,\%$ in males.

Under lateral loading conditions, no clear trend is seen with age for mid-level ribs (4 through 9), however a small decrease in stiffness is seen with age for higher rib levels. Constrained lateral loading provides the stiffest response of the four conditions, with vertical deflection occurring at over $100\,\mathrm{N/mm}$ for most ribs. Univariate trends in stiffness with age are generally small, with the increases in stiffness with age at mid-level ribs explaining under $3\,\%$ of overall variation.

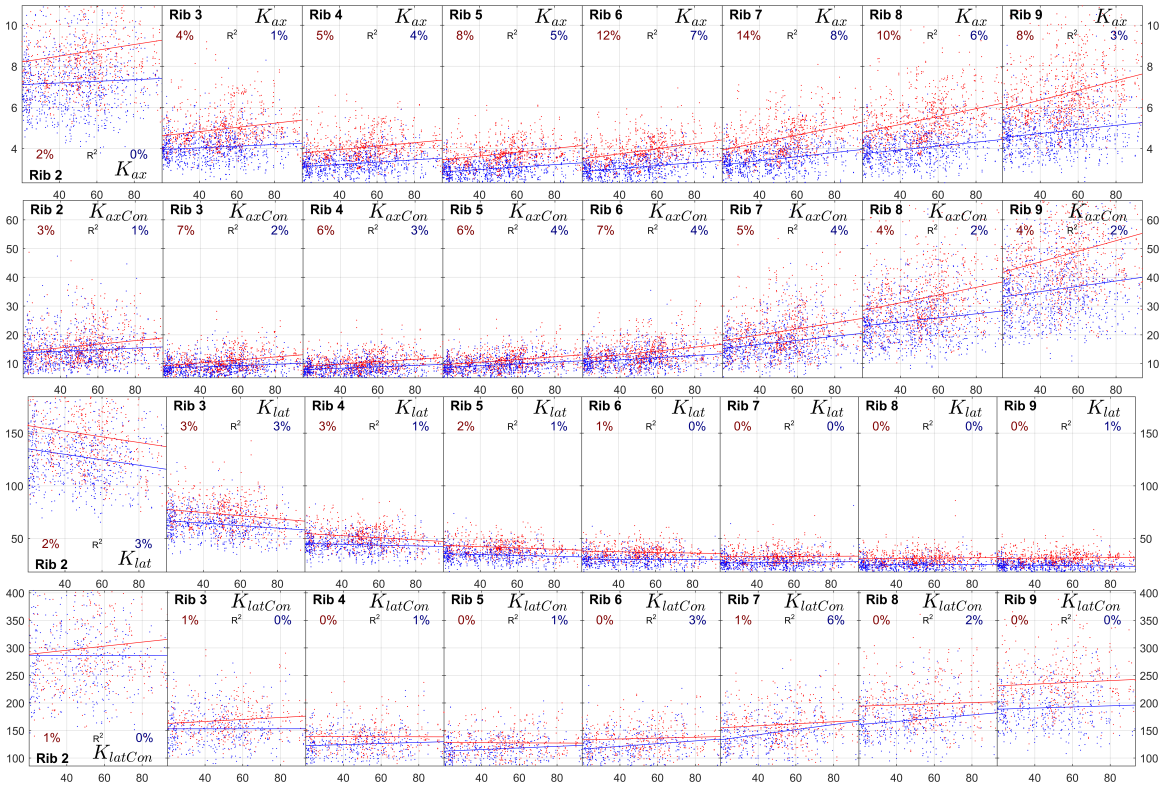

Figure 4.3: Characteristic rib stiffness to multiple loading conditions by age and gender, ribs 2 to 9. Rows show (from top to bottom) stiffness under axial loading (K_{ax}), constrained axial loading (K_{axCon}), lateral loading (K_{lat}), and constrained lateral loading (K_{latCon}). Best fit lines are given for males and females along with the explanatory power (r-squared) of age as a predictor of stiffness.

4.2.1.1 Predictive power of regression

In addition to the main population of rib shapes extracted from CT scans of the live subjects, we also created a corresponding set of rib shapes; this time by passing those individuals' demographic factors to the shape-by-regression model developed in Chapter 3. By doing this we can compare the ability of ribs from this regression model to accurately reflect the stiffness results that were obtained from their original, directly fitted, counterparts. Using 6$^{\text{th}}$ rib level ribs for this comparison, results are summarized in Table 4.4. They show that rebuilt ribs were better able to predict stiffness measures under simple axial compression than any other loading condition. Specifically, $62\,\%$ of the variation in axial stiffness (K_{ax}) that was seen in the original population could be reflected by using the regression model of rib shape driven by demographics.

Table 4.4: Predictive power (r-squared) of ribs rebuilt using the demographics regression model to reflect rib stiffness as measured from the original real geometries.

Loading condition	r-squared
Free axial	0.62
Constrained axial	0.27
Free lateral	0.25
Constrained lateral	0.23

4.2.2 Rib shape by stiffness

Ribs from all subjects were stratified by their stiffness under each loading condition, and separated into groups from least to most stiff. Averages for each of the six rib shape parameters were calculated from within groups, and are provided in Tables 4.5 to 4.8 to quantify the softest shapes (below 10$^{\text{th}}$ percentile in stiffness), average (45$^{\text{th}}$ to 55$^{\text{th}}$ percentile), and stiffest rib shapes (above 90$^{\text{th}}$ percentile) under a given loading condition. These data are then passed directly to the rib shape model to produce typical rib shapes matching those same categories from softest to stiffest under each loading condition as

shown in Figures 4.4 to 4.7.

In axial loading (Figure 4.4 and Table 4.5), stiffer ribs tend to have shorter end-to-end spans (lower S_x parameter), and greater aspect ratio (lower Y_{Pk}). Stiffer ribs also had marginally greater inner angles at the vertebral end (ϕ_{pia}), making them initially extend more posteriorly at the vertebral end. Overall it is clear that size and arc length tend to control the stiffness response under axial loading.

Table 4.5: Rib shape parameters by stiffness (K_{ax}) in axial loading (5th, 50th, and 95th percentile stiffness across the population).

#	S_x (mm)			X_{Pk} (mm/S_x)			Y_{Pk} (mm/S_x)			ϕ_{pia} (deg.)			B_p			B_d		
	5th	50th	95th	5th	50th	95th	5th	50th	95th	5th	50th	95th	5th	50th	95th	5th	50th	95th
1	73	71	65	0.40	0.40	0.41	0.60	0.52	0.47	82	80	78	-0.44	-0.48	-0.54	1.62	1.50	1.57
2	121	111	101	0.32	0.31	0.34	0.66	0.62	0.58	113	112	111	-0.28	-0.29	-0.40	0.72	0.65	0.92
3	150	142	132	0.34	0.34	0.35	0.63	0.59	0.54	114	117	121	-0.47	-0.50	-0.56	0.36	0.35	0.40
4	174	166	157	0.32	0.32	0.32	0.57	0.53	0.48	113	116	119	-0.44	-0.48	-0.56	-0.02	-0.10	0.02
5	194	185	176	0.32	0.31	0.31	0.52	0.48	0.44	111	115	117	-0.47	-0.51	-0.58	-0.28	-0.39	-0.43
6	205	199	190	0.31	0.30	0.28	0.48	0.43	0.39	109	114	116	-0.43	-0.45	-0.48	-0.46	-0.50	-0.51
7	217	207	201	0.30	0.29	0.27	0.44	0.40	0.34	106	111	114	-0.35	-0.36	-0.41	-0.34	-0.17	0.11
8	221	208	196	0.31	0.31	0.29	0.40	0.37	0.32	104	105	106	-0.32	-0.39	-0.43	-0.27	-0.22	-0.11
9	212	198	183	0.35	0.35	0.34	0.40	0.36	0.32	96	98	100	-0.47	-0.51	-0.65	-0.17	-0.06	0.00
10	200	182	165	0.38	0.37	0.37	0.38	0.33	0.29	88	88	85	-0.45	-0.54	-0.66	-0.07	-0.11	-0.15
11	180	154	132	0.39	0.39	0.41	0.32	0.28	0.23	85	82	77	-0.36	-0.58	-1.21	0.13	0.46	1.77
12	134	99	46	0.44	0.42	0.31	0.24	0.18	0.12	84	62	35	-1.29	-1.66	0.41	1.47	0.71	1.48

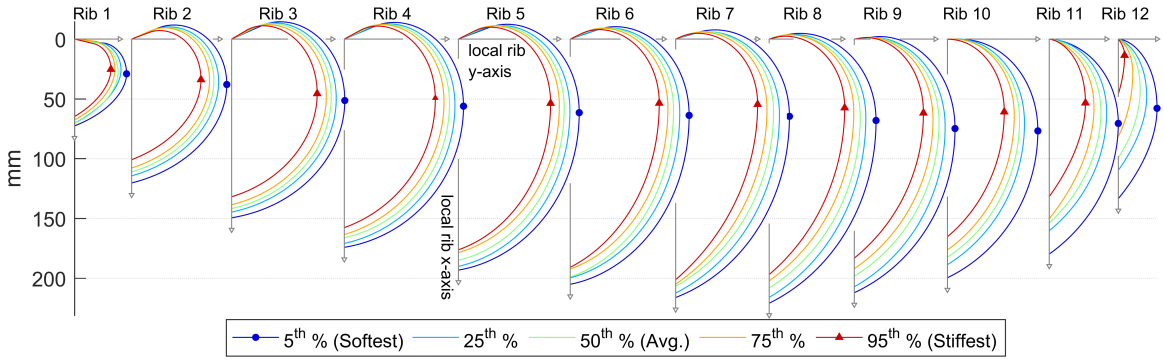

Figure 4.4: Typical rib shapes exhibiting low, medium, and high stiffness under axial compression. Stiffer ribs had lower S_x and Y_{Pk} values.

Under constrained axial loading (Figure 4.5 and Table 4.6) size (S_x) no longer plays such an important role, particularly in mid-to-lower levels where ribs of varying stiffness were all of approximately equal length. Instead, parameters which dictated rib arc

length independent of S_x were most closely related to overall stiffness. Ribs that are initially directed more anteriorly (lower ϕ_{pia}), have less skewness whereby their peak (X_{Pk}) is shifted towards the middle of the rib, and have lower Y_{Pk} values all produced stiffer responses to constrained axial loading.

Table 4.6: Rib shape parameters by stiffness (K_{axCon}) in constrained axial loading (5th, 50th, and 95th percentile stiffness across the population).

#	S_x (mm)			X_{Pk} (mm/S_x)			Y_{Pk} (mm/S_x)			ϕ_{pia} (deg.)			B_p			B_d		
	5th	50th	95th	5th	50th	95th	5th	50th	95th	5th	50th	95th	5th	50th	95th	5th	50th	95th
1	69	71	69	0.37	0.40	0.40	0.59	0.52	0.45	93	81	69	-0.51	-0.44	-0.45	2.24	1.63	1.95
2	113	110	108	0.27	0.32	0.37	0.68	0.62	0.56	118	112	105	-0.22	-0.29	-0.43	0.65	0.68	0.92
3	140	141	141	0.30	0.35	0.37	0.65	0.59	0.52	120	117	115	-0.41	-0.49	-0.61	0.36	0.38	0.47
4	164	167	166	0.29	0.32	0.35	0.58	0.53	0.48	119	115	113	-0.42	-0.50	-0.58	-0.04	-0.05	0.00
5	181	185	185	0.28	0.32	0.33	0.54	0.48	0.43	118	114	111	-0.42	-0.51	-0.56	-0.30	-0.37	-0.37
6	195	198	197	0.28	0.30	0.31	0.49	0.44	0.39	116	113	109	-0.41	-0.47	-0.46	-0.46	-0.51	-0.45
7	205	208	207	0.27	0.29	0.30	0.45	0.39	0.34	115	111	103	-0.35	-0.40	-0.34	-0.36	-0.22	0.21
8	211	207	204	0.29	0.31	0.31	0.41	0.36	0.32	109	107	97	-0.38	-0.41	-0.36	-0.35	-0.22	-0.09
9	206	199	190	0.34	0.35	0.35	0.40	0.35	0.31	103	99	92	-0.51	-0.56	-0.56	-0.23	-0.07	0.06
10	191	180	168	0.38	0.37	0.39	0.37	0.32	0.29	95	94	80	-0.67	-0.70	-0.55	0.07	-0.09	-0.10
11	173	149	134	0.39	0.38	0.39	0.31	0.27	0.23	96	83	73	-0.70	-0.69	-0.94	0.22	0.16	1.42
12	113	108	105	0.39	0.39	0.41	0.21	0.20	0.16	76	71	60	-0.66	-1.76	-2.00	2.50	0.97	0.58

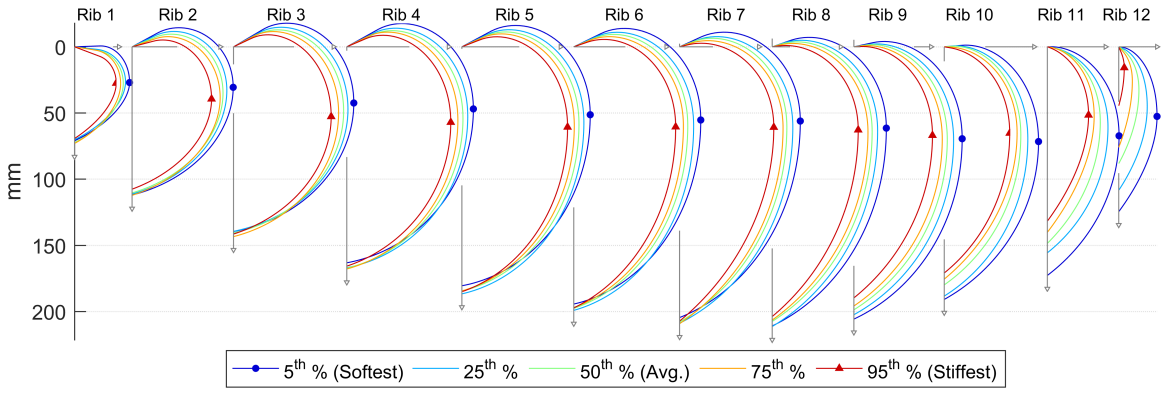

Figure 4.5: Typical rib shapes exhibiting low, medium, and high stiffness under constrained axial compression. Stiffer ribs had lower Y_{Pk} and ϕ_{pia} values and higher X_{Pk} values.

Figure 4.6 shows the stiffest and softest rib shapes under lateral loading, while Figure 4.7 shows constrained lateral loading. In both lateral loading conditions rib span (S_x) is a primary factor driving stiffness. However, in constrained lateral loading other factors that serve to reduce the overall arc length of a rib tend to produce the stiffest response.

Table 4.7: Rib shape parameters by stiffness (K_{lat}) in lateral loading (5th, 50th, and 95th percentile stiffness across the population).

#	S_x (mm)			X_{Pk} (mm/S_x)			Y_{Pk} (mm/S_x)			ϕ_{pia} (deg.)			B_p			B_d		
	5th	50th	95th	5th	50th	95th	5th	50th	95th	5th	50th	95th	5th	50th	95th	5th	50th	95th
1	80	70	63	0.41	0.38	0.28	0.52	0.51	0.51	76	79	92	-0.21	-0.39	-0.30	2.21	1.40	0.90
2	126	110	98	0.35	0.32	0.27	0.58	0.62	0.65	111	113	114	-0.44	-0.30	-0.14	0.98	0.71	0.49
3	162	141	125	0.36	0.34	0.32	0.53	0.59	0.63	117	117	119	-0.62	-0.49	-0.41	0.39	0.37	0.26
4	189	166	149	0.34	0.32	0.30	0.48	0.53	0.56	115	116	120	-0.63	-0.49	-0.41	-0.11	-0.04	-0.09
5	210	184	167	0.32	0.31	0.28	0.43	0.48	0.51	112	114	117	-0.66	-0.48	-0.38	-0.48	-0.39	-0.38
6	221	196	180	0.32	0.30	0.26	0.40	0.44	0.46	109	113	119	-0.64	-0.45	-0.28	-0.56	-0.53	-0.57
7	231	208	191	0.31	0.29	0.25	0.37	0.39	0.40	105	110	117	-0.58	-0.39	-0.27	-0.27	-0.24	-0.25
8	232	208	192	0.33	0.31	0.27	0.35	0.37	0.36	102	105	112	-0.56	-0.38	-0.28	-0.36	-0.17	-0.28
9	224	198	177	0.36	0.36	0.32	0.34	0.36	0.36	94	98	104	-0.65	-0.54	-0.48	-0.14	-0.06	-0.07
10	204	182	159	0.40	0.38	0.35	0.34	0.32	0.32	91	91	88	-0.77	-0.65	-0.39	-0.10	-0.21	-0.39
11	180	156	130	0.40	0.39	0.38	0.29	0.26	0.26	90	84	85	-0.63	-0.75	-0.84	-0.27	0.45	1.89
12	141	107	67	0.48	0.39	0.31	0.22	0.20	0.16	80	66	59	-1.74	-1.25	-0.50	2.40	0.30	1.25

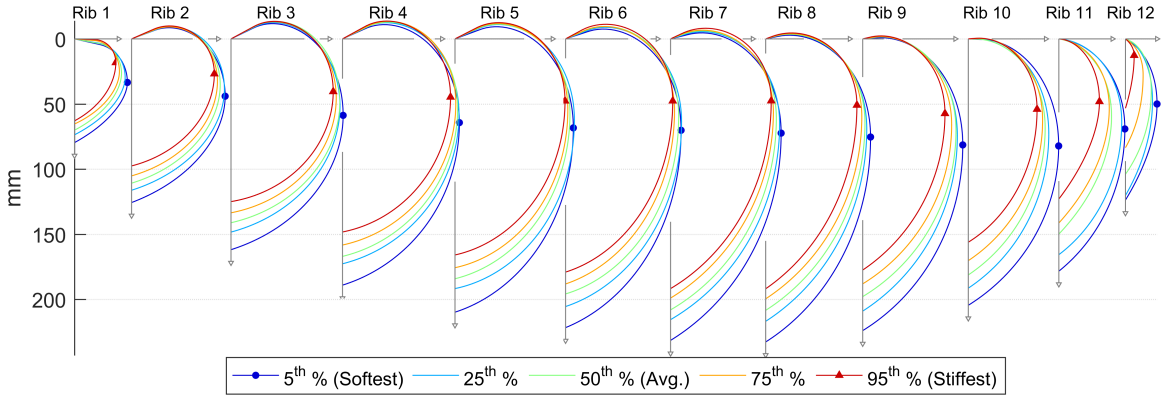

Figure 4.6: Typical rib shapes exhibiting low, medium, and high stiffness under lateral compression. Stiffer ribs had lower $S_x$and X_{Pk} values and higher Y_{Pk} and ϕ_{pia} values.

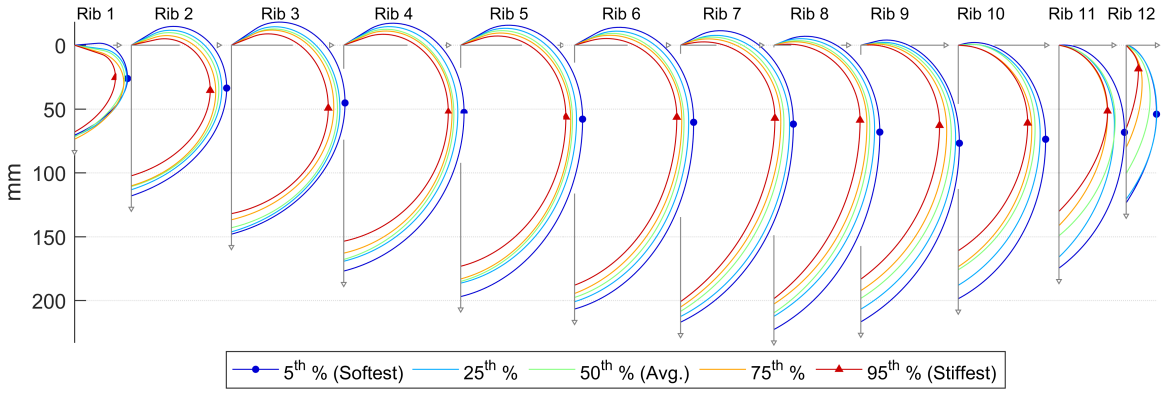

Figure 4.7: Typical rib shapes exhibiting low, medium, and high stiffness under constrained lateral compression. Stiffer ribs had lower S_x, Y_{Pk}, and ϕ_{pia} values.

Table 4.8: Rib shape parameters by stiffness (K_{latCon}) in constrained lateral loading (5th, 50th, and 95th percentile stiffness across the population).

#	S_x (mm)			X_{Pk} (mm/S_x)			Y_{Pk} (mm/S_x)			ϕ_{pia} (deg.)			B_p			B_d		
	5th	50th	95th	5th	50th	95th	5th	50th	95th	5th	50th	95th	5th	50th	95th	5th	50th	95th
1	71	77	72	0.43	0.33	0.44	0.60	0.51	0.59	86	78	72	-0.71	-0.24	0.43	2.50	2.50	0.86
2	117	111	103	0.28	0.32	0.35	0.64	0.63	0.59	121	113	103	-0.32	-0.30	-0.28	0.66	0.61	0.65
3	147	143	131	0.31	0.35	0.37	0.61	0.59	0.58	124	116	112	-0.48	-0.53	-0.49	0.38	0.38	0.31
4	177	167	154	0.30	0.33	0.34	0.54	0.52	0.52	121	117	110	-0.52	-0.52	-0.44	-0.07	0.03	-0.01
5	194	185	174	0.30	0.32	0.32	0.50	0.48	0.47	118	115	109	-0.56	-0.54	-0.41	-0.39	-0.31	-0.36
6	204	199	188	0.30	0.31	0.30	0.46	0.43	0.42	121	112	108	-0.57	-0.51	-0.26	-0.53	-0.56	-0.58
7	214	209	202	0.29	0.29	0.28	0.41	0.39	0.37	119	110	101	-0.60	-0.38	-0.16	-0.43	-0.12	0.01
8	222	208	197	0.31	0.31	0.30	0.37	0.36	0.34	112	105	96	-0.62	-0.39	-0.15	-0.47	-0.17	-0.12
9	215	197	182	0.36	0.35	0.34	0.36	0.36	0.34	105	97	92	-0.80	-0.55	-0.39	-0.35	-0.03	-0.01
10	197	179	167	0.35	0.37	0.37	0.31	0.33	0.34	91	91	78	-0.87	-0.50	-0.03	-0.19	-0.23	0.04
11	167	146	140	0.38	0.38	0.37	0.27	0.29	0.28	87	81	73	-0.97	-0.70	-0.05	-0.77	0.76	1.46
12	117	88	66	0.41	0.47	0.24	0.19	0.16	0.15	63	45	48	-1.88	-1.00	-0.17	0.98	1.28	2.50

4.2.3 Age series results

The six series of rib shapes that were rebuilt using the demographics-based predictive model (from Chapter 3) each represent ribs from an individual of a particular demographic (F05, F50, M95, etc.), and of age ranging from 20 to 90 years. The 6th ribs from across each series were subjected to the four loading conditions, and their stiffness calculated in each instance. Results under axial loading are presented in Figure 4.8 with values normalized by the stiffness of the 20-year-old ribs in each series. In both axial loading and constrained axial loading, rib stiffness was seen to increase with age. In all demographics stiffness to axial loading increased by 12 %–17 % as age transitioned from 20 to 90. In constrained axial loading this increase in stiffness was between 17 % and 31 %. Lateral loading results (Figure 4.9) were mixed, with larger individuals (M95, M50) showing little to no stiffness change with age while others showed a decrease in stiffness of between 8 % and 17 %. In constrained lateral loading this pattern continued, however only the smallest individuals (F05, F50) showed a decrease in stiffness of around 9 % while others showed no clear change with age.

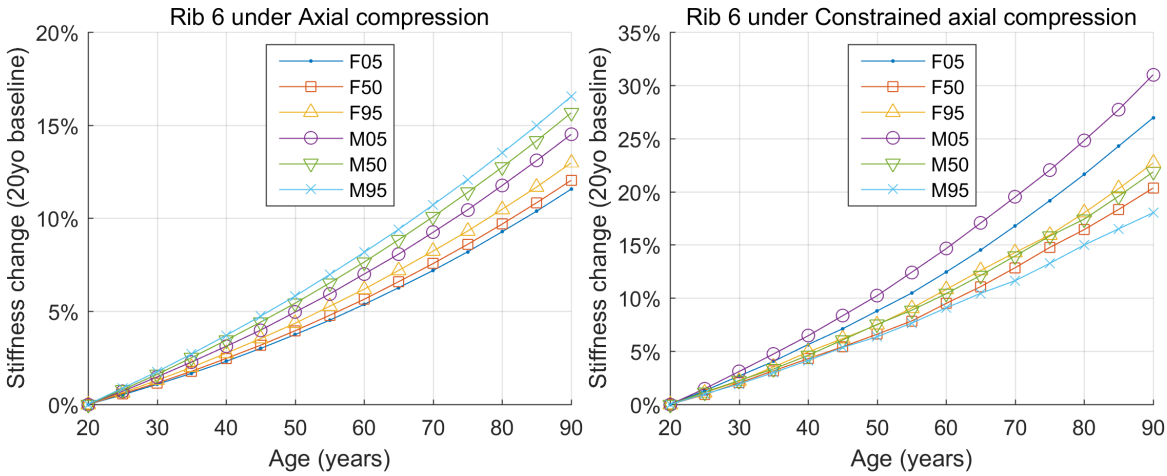

Figure 4.8: Rib stiffness in free and constrained axial compression using demographics-based series of aged ribs. As age advances from a 20-year-old baseline, the stiffness due to in-plane shape in each condition increases.

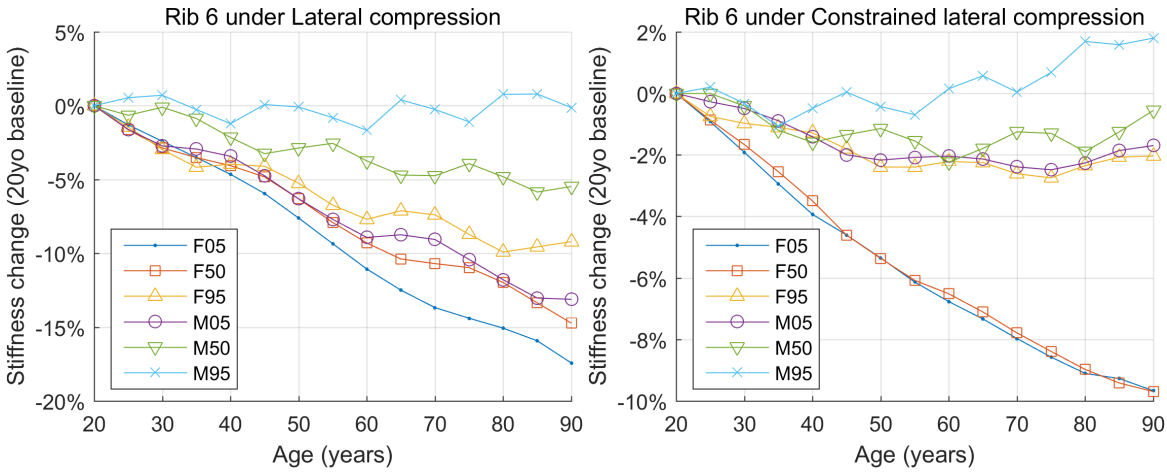

Figure 4.9: Rib stiffness in free and constrained lateral compression using demographics-based series of aged ribs.

4.2.4 Stress distribution by loading

Exemplar von-mises stress distributions at $5\,\%$ compression in each of the loading conditions are shown in Figure 4.10. For loading configurations with a rigid wall contact, the local stress concentration at the contact site was ignored when tracking the maximum stress location, and only local maxima at other regions of the rib were considered (see Figures 4.10 and 4.11).

Figure 4.11 gives the stress profiles along the length of 6^{th} ribs in the F50 age series at a

displacement of $4\,\mathrm{mm}$. In this figure the maximum von-mises stress at any of the elements around the rib is shown, resulting in 100 discrete element locations arranged from the proximal or vertebral end ($0\,\%$ along the rib arc length) to the distal end ($100\,\%$ along the arc length).

Across the full population the maximum stress location under axial loading was invariably within a short distance ($2\,\%$ of overall rib length) from the apex of the rib. Due to the differing shapes at each rib level, this was between $40\,\%$–$50\,\%$ of the arc length for ribs 2 and 3, and occurred progressively earlier for successive rib levels up to the 8th rib, which had its apex located between $35\,\%$–$45\,\%$ along its length. This location of maximum stress in axial loading was correlated with age at mid-level ribs ($p < 0.001$ for ribs 4 to 9), with this position shifting posteriorly by $0.5\,\%$ of the rib's arc length per decade. Age was not seen to alter the offset between the position of maximum stress and the apex of the rib ($p > 0.05$ at all rib levels). Under constrained axial loading the location of maximal stress ranged from $20\,\%$–$26\,\%$ along the rib's length (rib 2) to $16\,\%$–$19\,\%$ along the rib's length (rib 9). This location was again seen to move closer to the proximal rib end with age ($p < 0.001$ for ribs 2 to 11) at a rate of approximately $0.2\,\%$ of the rib's arc length per decade (ribs 3 to 9). Constrained lateral loading produced stress distributions similar to those seen in constrained axial loading, with a concentration due to contact under the loading wall, and a maximum stress location towards the posteriorly extending rib region. Free lateral loading stress was dominated by the region in contact with the moving wall.

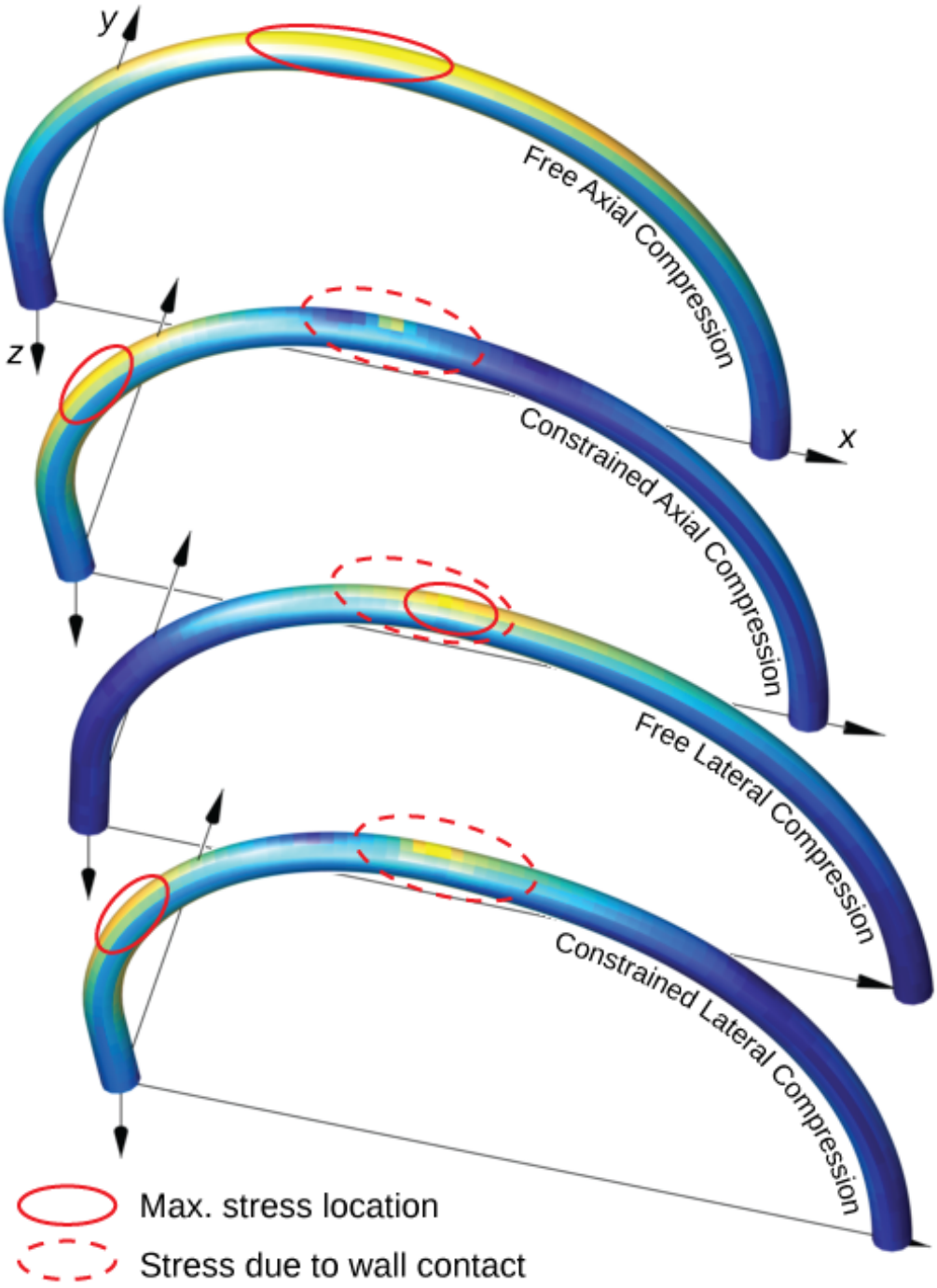

Figure 4.10: Von-mises stress distribution at $4\,\mathrm{mm}$ compression in each condition for typical 6^{th} ribs. Wall contact produced a local stress concentration, so maximum stress locations were considered only in non-contact regions.

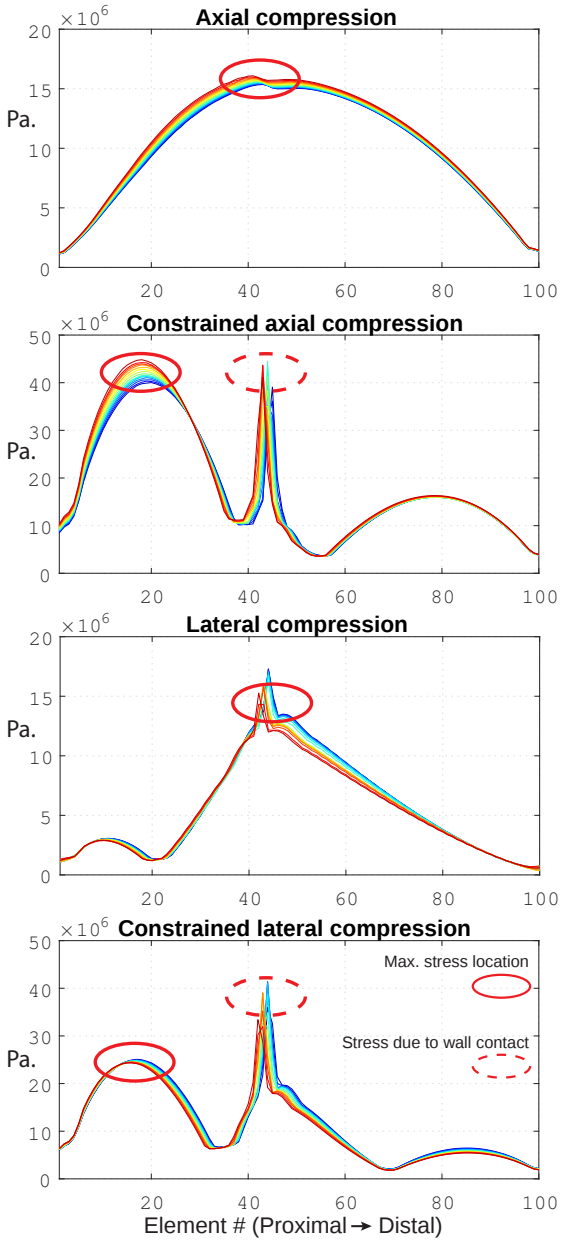

Figure 4.11: Von-mises stress profiles as a function of rib position for 6th ribs from F50 individuals of 20 to 90 years of age. Stress profiles differ by loading condition, and peak stress locations shift marginally with age.

4.3 Discussion of mechanical loading results

Shape and mechanical response was simulated using models from a large population of ribs extracted from CT image data. The subject group was chosen so as to adequately represent the breadth of demographics seen throughout the population. An efficient parametric model produced a simplified representation of the overall rib shape, and mechanical loading was simulated for each rib. Results in terms of stiffness to loading were collected in multiple loading conditions. Results showed an increase in rib stiffness with age when loaded in a largely body-anterior direction, and stiffness results were mixed when loading in largely body-lateral directions. The specific rib shapes that are stiffest or softest under different loading conditions were also quantified, with results showing significant reliance on loading conditions when assessing stiffness due to shape.

4.3.1 Loading conditions

The axial loading condition used in this study was chosen to match the framework set forth by Charpail et al. (2005) which has since been adopted in multiple experimental studies (Kindig et al., 2011; Kindig and Kent, 2013; Agnew et al., 2015). This framework aims to model the forces that may be applied to ribs during frontal impact loading.

Since rib fractures also occur in other impact scenarios, three additional loading setups were considered that approximate loading that may also be experienced by ribs in lateral or offset frontal impacts. The constrained axial loading represents a primarily body-anterior load with a lateral component sufficient to prevent lateral displacement of ribs during deformation. The constrained lateral loading condition represents a primarily lateral load to the body, but with a sufficient anterior component to prevent anterior rib displacement. The free lateral loading setup is less likely to be experienced *in vivo* due to the presence of costal cartilage and the sternum, but it tests a rib that is loaded from a lateral direction but experiences no resistance to displacement its sternal end. In each case, an attempt was made

to present a simple loading condition that may potentially be reproduced experimentally.

4.3.2 Stress location variation

Results from this study suggest that overall shape does influence the position of maximum stress as a function of overall arc length. However, this position varies across the population by around $10\,\%$–$15\,\%$ of the rib's length, and primarily tracks key locations such as the rib peak. In free axial loading, stress is distributed more evenly over a large portion of the rib than in the two constrained conditions where a localized stress concentration is present near the posterior arch. For context, Agnew et al. (2015) specified rib positions categorically as posterior, lateral, and anterior, and found fractures after axial compression to occur in each zone (but with the anterior and lateral locations most common). This makes fracture distribution in physical experiments far more variable than is seen in the maximum stress locations here. These results suggest that the actual fracture site may be more dependent on local factors such as regional material or cortical thickness properties than it is on overall rib shape.

4.3.3 Stiffness variation due to age and shape

Previous work had identified a clear aging effect on the overall shape of ribs, with older ribs having longer spans between ends yet passing through an overall shallower curvature between those ends. This study has confirmed that in a number of loading conditions this change in shape indeed has an effect on the rib's ability to resist loading. In both forms of axial loading univariate analysis showed that older mid-level ribs were significantly stiffer than younger ribs, with stiffness increasing at around $0.15\,\mathrm{N/mm}$ per decade. This increase was confirmed when tracking the stiffness of ribs for all demographic series. As each individual was aged from 20 to 90 years, 6$^{\text{th}}$ level ribs showed an increase in stiffness of up to $30\,\%$.

The increased stiffness with age reported here is contrary to changes seen in experimen-

tal studies (Agnew et al., 2015) which, by their nature, incorporate all variables affecting rib mechanics rather than just rib shape as has been isolated here. In Agnew et al. (2015) ribs in axial loading showed a decrease in stiffness at a rate of around $-0.33\,\mathrm{N/mm}$ per decade, albeit with considerable variation around this trend (pseudo r-squared value of stiffness predicted by age of $13.8\,\%$). Despite having opposing directions of change with age, these two results are not incompatible. Instead, they suggest that while overall rib shape may change to produce stiffer ribs with age, the aggregation of other age-related changes (such as material properties that are known to degrade) serve to reduce stiffness on the whole. Such contrasting effects are not unheard of, and are indeed seen again in the chest at different scales. In particular, overall chest stiffness is seen to increase with age (Kent et al., 2003b) in contrast with isolated ribs (Agnew et al., 2015), which are in turn in contrast to the changes described in the current study showing a stiffening of ribs due to the isolated effect of shape. Overall, these results point to the importance of addressing potential sources of variation independently when creating biomechanical models that will aggregate to predict a mechanical outcome.

CHAPTER 5

Ribs in the context of the thoracic skeleton

The previous chapters have dealt primarily with details of the overall size, shape, and curvature of ribs, along with their orientation within the body. This has consequently involved only analysis of isolated ribs in their local rib plane (or an analysis of the orientation of that plane). In this chapter we will apply similar parameterization techniques to other parts of the thoracic skeleton in order to build a body scaffold, and to place the ribs in their true context in relation to the rest of the thoracic skeleton. The aim here is to showcase the methodology whereby a limited set of parameters can be used to represent the geometry of a body part in a local setting, and then to have the accumulation of those body part geometries make a coherent body. This modular approach is illustrated in Figure 5.1, which highlights the three main anatomic models to be described in this chapter – namely, the spine, ribs, and sternum – alongside further parametric models of the spatial relationships between those pieces of anatomy. The following sections will deal with each individual anatomic model with its local parameters separately, and we will conclude the chapter by combining these modules to produce an overall thoracic skeleton model that can flexibly represent the typical rib cage of any chosen demographic population.

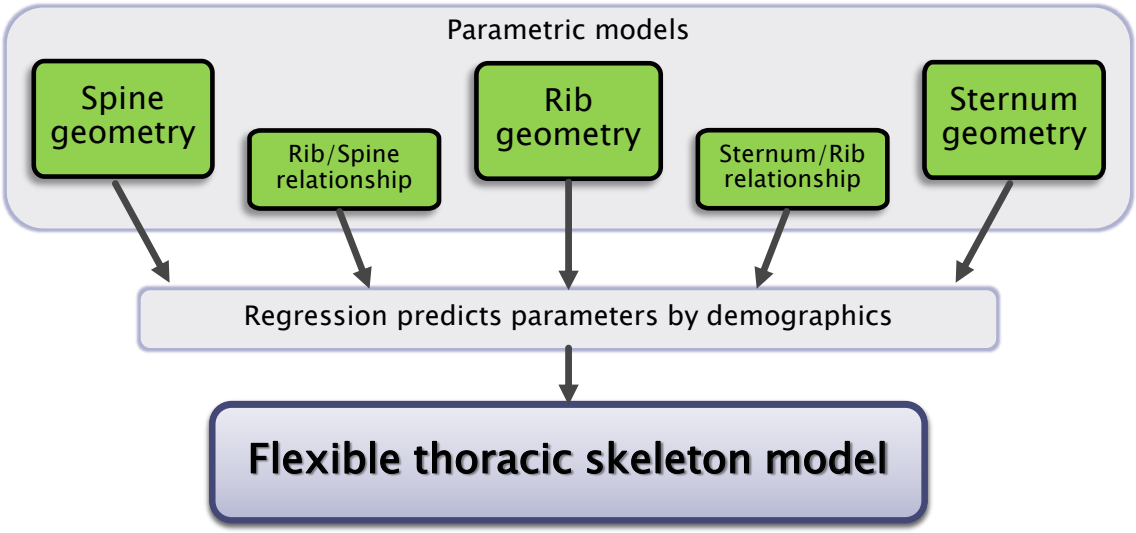

Figure 5.1: Overview of the modular parametric modeling approach.

5.1 Spine parameterization

The geometry of the spine provides a basis for the placement of ribs and the rest of the thoracic skeleton. While the spine itself contains highly detailed and specialized geometry, we wish simply to describe its position and curvature in a quantitative fashion. This can be done by taking "a curve through the center of the spinal canal" as the desired shape to be modeled. In order to produce this geometrically, we can treat the spinal canal as being formed by a series of vertebral segments and then choose a finite set of parameters to represent each segment using:

- The height of each vertebral segment
- The angle of each vertebral segment with respect to its inferior neighbor
- The position and angle of the lowest vertebral segment with respect to the body

These quantities can then be measured from CT scans. In Section 1.5.1 we saw that the first piece of geometry processed for scans in the ICAM database is the spine, and that the spine is represented by 3D landmarks placed in the spinal canal at each vertebral level. Using those same spine landmarks, Figure 5.2 depicts the measurement of vertebral

segment size and vertebral segment angle for an example L4 vertebra.

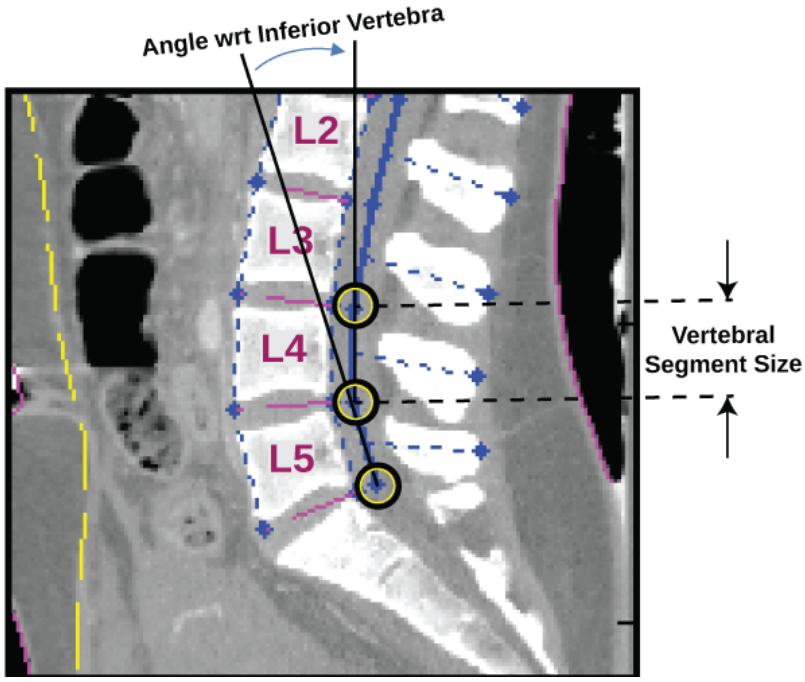

Figure 5.2: Spine landmark placement with vertebral height and vertebral angle. Landmarks in the spinal canal at the inferior aspect of three consecutive vertebral bodies allow for the inner angle to be calculated between two adjacent vertebrae. Vertebral segment height is parameterized as the straight line distance between consecutive vertebral landmarks.

Using the population of adult trauma scans (in supine position) from the ICAM morphomics database, these measurements were collected across a wide group of individuals and trends with demographics assessed once again using multivariate regression. For example, scattered data for the adjusted vertebral angle measurements by age for a series of vertebrae (L4, T12, T8, T4) is shown in Figure 5.3, along with regression corridors indicating the expected angles by age. The variation within the population is substantial compared to the age effects seen; however, those effects nevertheless reflect clear and highly significant trends with demographics ($p < 0.001$) at all vertebral levels. The magnitude of vertebral angles is highest in L4 (which forms an over $-15°$ angle with L5 in most individuals), whereas the clearest age trends are seen near T4, which shows an increasing angle (or kyphotic curvature) with age. The multivariate regression coefficients (for age,

height, weight, and sex) for the vertebral segment parameters (identified as $VBSEG_{\alpha}$ and $VBSEG_{Sz}$) are provided in Table 5.1.

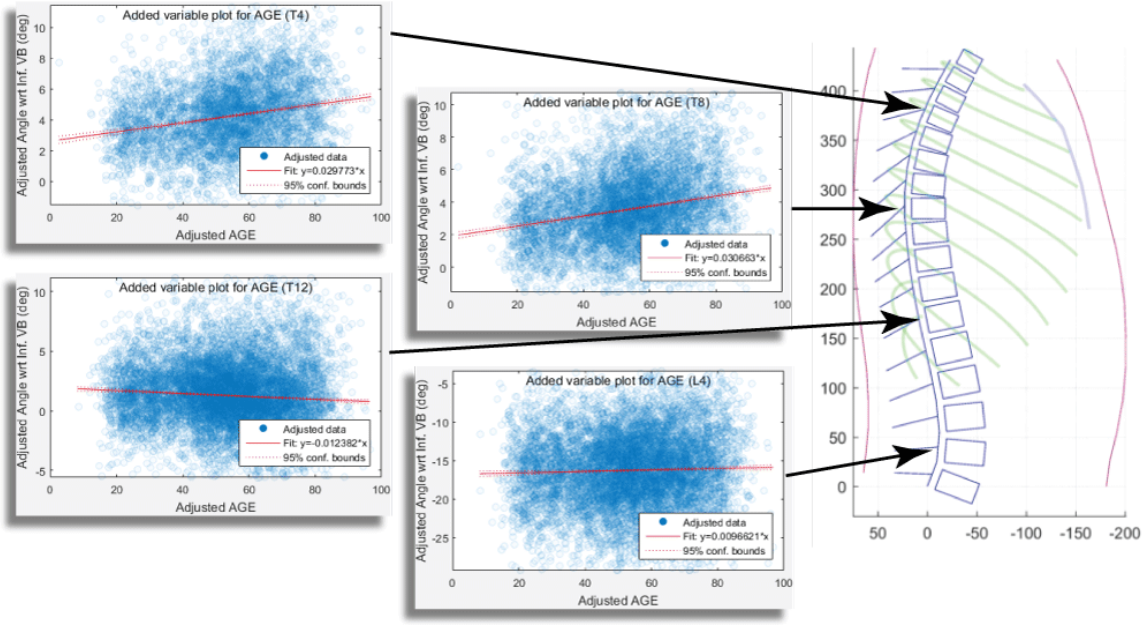

Figure 5.3: Scatter of adjusted vertebral angle (with respect to the inferior vertebral orientation, in degrees) for exemplar vertebral levels. Results show relatively little correlation between lumbar angle and age at L4, compared with the effect on thoracic vertebrae which serve to increase spine kyphosis with age.

Finally, in order to place the lowest vertebra (L5) at an appropriate orientation, its angle ($L5_{pitch}$) in the sagittal plane with respect to the global z-axis is chosen. That $L5_{pitch}$ parameter was measured at L5 across all scans, and the resulting coefficients providing the angle as a function of demographics are found in Equation (5.1). Here again, age (Y) is in years, sex (S) is 0 for males and 1 for females, height (H) is in meters, and weight (W) is in kilograms. All coefficients were highly significant ($p < 0.001$) indicating that the initial angle of the L5 vertebra is strongly dependent on demographics.

$$L5_{pitch} = -43.3 - 0.0535A + 1.734S + 16.169H - 0.0222W \tag{5.1}$$

The results of Equation (5.1) and Table 5.1 provide all that is needed to generate a curve comprised of single-vertebra segments that runs along the center of the spinal canal. That

Table 5.1: Vertebral body segment angle and size parameters. Age (A) is in years, sex (S) is 0 for males and 1 for females, height (H) is in meters, weight (W) is in kilograms, along with the regression intercept (I). Subscript denotes scale factor. For example, $W_{E\text{-}3}$ indicates weight in kg scaled by 1×10^{-3}. Coefficients significantly different from zero at the $p < 0.05$ level are shown in bold.

	$VBSEG_{\alpha}$ (deg)					$VBSEG_{Sz}$ (mm)				
#	$I_{E\text{-}1}$	$A_{E\text{-}3}$	$S_{E\text{-}2}$	$H_{E\text{-}1}$	$W_{E\text{-}3}$	$I_{E\text{-}1}$	$A_{E\text{-}3}$	$S_{E\text{-}2}$	$H_{E\text{-}1}$	$W_{E\text{-}4}$
T1	12	**14**	**-61**	**-23**	**7**	**76**	2	**-109**	**68**	**38**
T2	**-23**	**13**	**-42**	**18**	-1	**70**	**5**	**-114**	**78**	**63**
T3	1	**23**	7	**17**	**-13**	**47**	**9**	**-79**	**96**	**54**
T4	**41**	**30**	4	-3	**-13**	**44**	**13**	**-68**	**103**	4
T5	**30**	**42**	**35**	5	**-12**	**43**	**14**	**-82**	**110**	-13
T6	**26**	**42**	**47**	9	**-12**	**53**	**17**	**-91**	**110**	**-27**
T7	**25**	**39**	**28**	9	**-13**	**53**	**12**	**-84**	**114**	-14
T8	**21**	**31**	4	1	**-4**	**61**	**7**	**-83**	**112**	-11
T9	**29**	**17**	9	**-12**	**3**	**63**	**5**	**-68**	**113**	14
T10	**19**	**4**	12	-0	-1	**55**	**9**	**-54**	**125**	16
T11	**20**	-3	6	6	**-5**	**51**	**14**	**-46**	**140**	-6
T12	15	**-12**	-3	5	**-6**	**65**	**7**	**-51**	**145**	23
L1	**-34**	**-31**	-1	**33**	**-13**	**66**	**-7**	**-62**	**159**	18
L2	**-143**	**-38**	**24**	**77**	**-21**	**77**	**-29**	**-35**	**164**	-1
L3	**-210**	**-36**	1	**82**	**-19**	**40**	**-40**	-5	**181**	-2
L4	**-222**	**10**	21	**36**	**-11**	**40**	**-42**	-2	**169**	**-48**
L5	-59	-21	-69	-64	-7	**71**	**-8**	**44**	**116**	21

shape is shown in Figure 5.4 for four separately aged males. For ease of visualization, vertebral bodies and a line denoting the spinous process have been added. Further discussion of curvature changes with age and a comparison to past literature is provided below in Section 5.5.3.

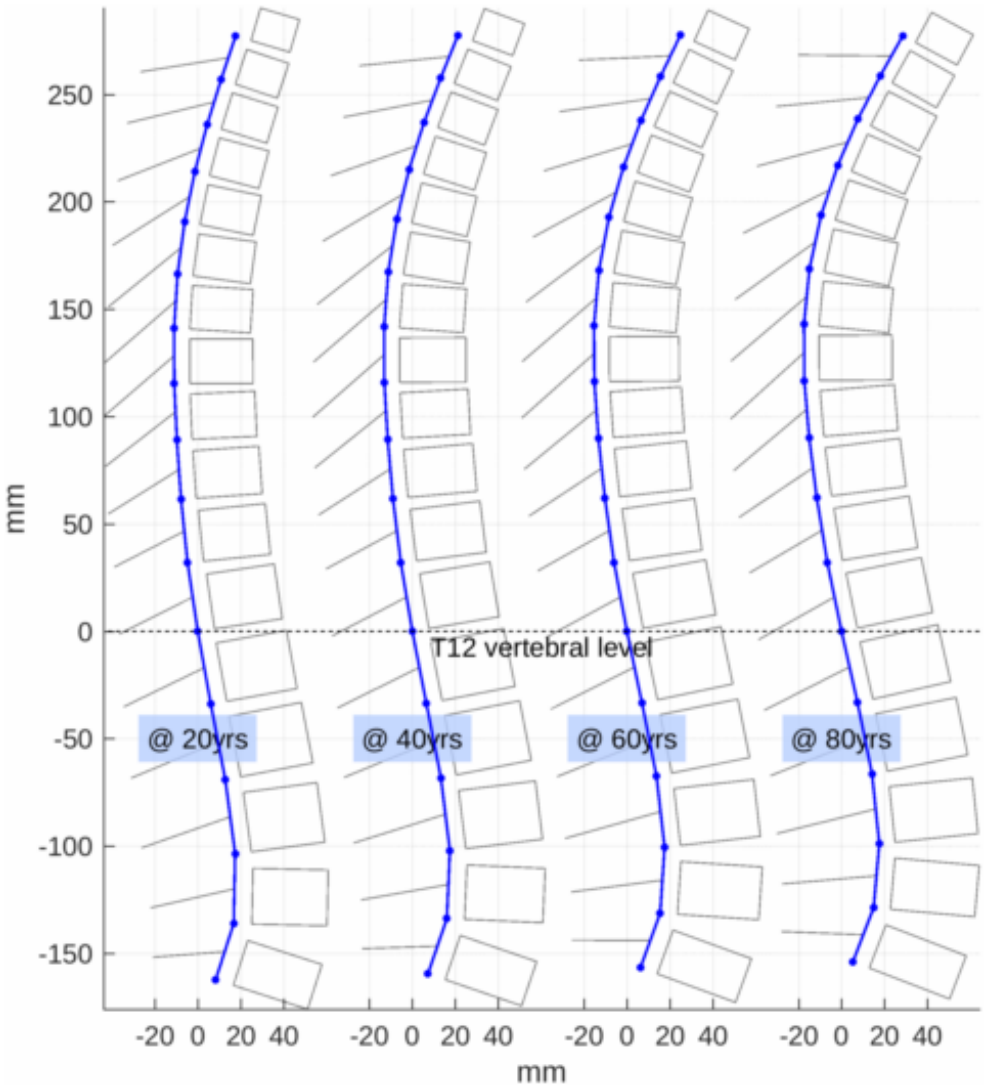

Figure 5.4: Regression predictions used to rebuild average spine shapes of 20, 40, 60, and 80 years individuals. Results reflect greater degrees of kyphosis with age.

5.2 Rib path completion

5.2.1 Rib out-of-plane shape

In Chapter 2 we developed a new method for parameterizing the in-plane shape of ribs, and in Chapter 3 we described how those in-plane shapes change with demographics. Recall from the Introduction the definition of the rib coordinate system (shown again in Figure 5.5), and consider the further aspect of overall shape that is given by the out-of-plane deviation of ribs as they sweep from their proximal to distal ends.

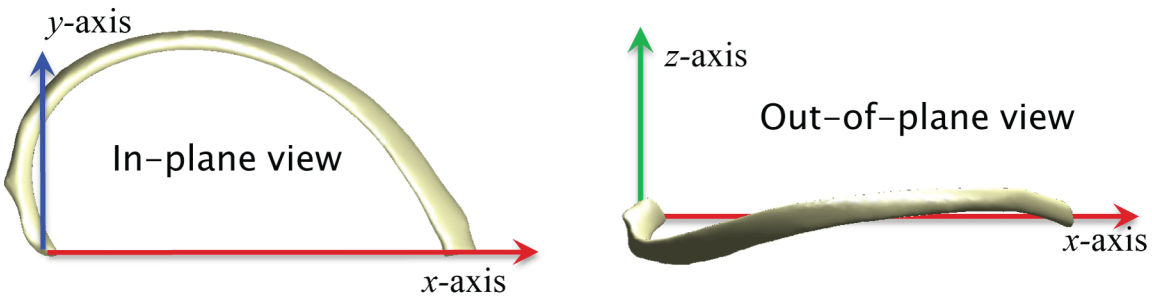

Figure 5.5: In-plane view and out-of-plane view of a single rib.

We model the out-of-plane deviation independently to the in-plane shape, and do so as a function of the overall rib arc length. Rib out-of-plane shape tends to follow a consistent pattern as depicted in Figure 5.6, which gives this out-of-plane deviation as a function of proportional distance along the rib length. To ensure equivalent directions of deviation between left and right rib local coordinate systems, the z-deviation of right-sided ribs was reversed. Within this convention the neck of the rib generally extends below the rib plane before passing back above the plane at around mid-shaft. The distal portion of the rib rises before eventually returning to the plane (at $z = 0$) at its distal end.

A cubic Bezier curve was used to fit the out-of-plane deviation signal, with the restriction that the ends of the fitted curve were constrained to the origin (0,0) and rib anterior end (1,0) as illustrated in Figure 5.6. The mathematical bases for this Bezier curve are Bernstein polynomials of degree 3, $3\ell(1-\ell)^2$ and $3\ell^2(1-\ell)$, where ℓ ranges from 0 to 1.

Therefore, the fitted curve can be determined by regression coefficients corresponding to these two bases, Z_A and Z_B as given in Equation (5.2).

$$E(\text{Deviation} \mid \ell) = Z_A(3\ell(1-\ell)^2) + Z_B(3\ell^2(1-\ell)) \tag{5.2}$$

5.2.1.1 Out-of-plane shape parameters by demographics

In a similar fashion to the regression to demographics that were performed for the in-plane shape parameters for each rib, regression analyses were performed for the two

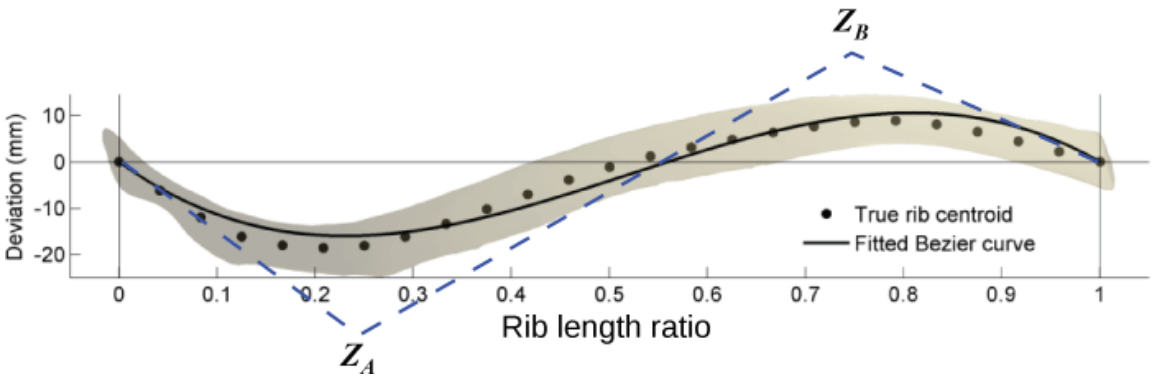

Figure 5.6: Rib out-of-plane deviation. Original centroidal deviation is shown as a function of relative rib centroidal length ℓ, with Bezier curve from fitted Z_A and Z_B parameters.

out-of-plane parameters Z_A and Z_B. Their resulting coefficients to age, height, weight, and sex are shown in Table 5.2.

Table 5.2: Rib out-of-plane parameters by demographics.

	Z_A (mm)					Z_B (mm)				
#	$I_{E\text{-}1}$	$A_{E\text{-}3}$	$S_{E\text{-}1}$	$H_{E\text{-}1}$	$W_{E\text{-}3}$	$I_{E\text{-}1}$	$A_{E\text{-}3}$	$S_{E\text{-}1}$	$H_{E\text{-}1}$	$W_{E\text{-}3}$
1	22	7	**-15**	20	-3	-19	-6	**14**	-26	4
2	-57	**119**	**-21**	-47	**41**	49	**-124**	**24**	41	**-38**
3	**-185**	**137**	13	-9	**44**	**187**	**-149**	-7	6	**-49**
4	**-270**	**159**	**16**	-2	**44**	**266**	**-166**	-8	5	**-53**
5	**-239**	**199**	-10	-36	**27**	**238**	**-202**	**17**	42	**-37**
6	**-300**	**177**	**-33**	-44	**49**	**304**	**-179**	**37**	49	**-59**
7	**-200**	**104**	**-40**	**-134**	**69**	**197**	**-103**	**44**	**144**	**-78**
8	**-154**	**52**	**-30**	**-186**	**105**	**148**	**-47**	**33**	**200**	**-113**
9	-64	**33**	**-14**	**-197**	**110**	55	**-29**	**14**	**210**	**-116**
10	-4	**29**	4	**-137**	**72**	5	**-24**	-5	**138**	**-77**
11	**82**	8	**10**	**-67**	14	**-81**	-2	**-12**	**65**	**-18**
12	1	**-23**	**9**	1	**14**	-1	**25**	**-10**	-2	**-18**

As can be seen in Table 5.2, age has a significant effect on the out-of-plane parameters, particularly for ribs 2 through 9. Increasing age serves both to increase the Z_A parameter and to decrease the Z_B parameter, with both Z_A and Z_B moving towards zero with increasing age. It can be seen that in this way a further flattening of the overall rib shape is present with age, as elderly ribs are found to be more planar (i.e., have less overall out-of-plane deviation) than younger ribs.

A similar effect is seen with added weight, whereby heavier individuals are associated with significantly less out-of-plane deviation (zA increases, Z_B decreases). Other changes with demographics include a clear gender difference whereby females tend to have significantly more out-of-plane deviation than males, at least in mid-level ribs 5 to 9.

5.2.2 Rib placement

In Chapter 3 we identified three orientation parameters (α_{PH}, α_{LS}, α_{BH}) which describe the pose of ribs within the body, and built regression models that can predict these angles based on demographic factors. However, these angles alone do not allow us to place the ribs in their correct 3D position with respect to the spine. Here, we will identify a further three parameters per rib to describe the x-, y-, and z-coordinate of that rib's proximal end as an offset from the center of the spinal canal at their corresponding vertebral level. The precise location on the spine from which rib ends are offset is chosen to be along the spinal canal at the inferior aspect of the vertebral body. For example, the position of the proximal end of a given person's 6$^{\text{th}}$ ribs might lie $12\,\mathrm{mm}$ lateral ($RIBOFF_x$ parameter) from the midline their T6 vertebra, $3\,\mathrm{mm}$ posterior ($RIBOFF_y$) to the center of the spinal canal at T6, and $6\,\mathrm{mm}$ superior ($RIBOFF_z$) to the inferior aspect of T6.

Regression coefficients to demographic predictors of these three offsets from the spine are provided in Table 5.3.

Results show that there are indeed significant – albeit small in magnitude – differences across demographics in the position of ribs relative to the spinal canal. Older individuals, males, and taller individuals each have the lateral position of ribs further from the body mid-line sagittal plane. Similarly, females have their ribs positioned around $1.3\,\mathrm{mm}$ more anterior relative to the spinal canal than males.

It is expected that some of these differences are actually describing differences in vertebral size. In the limited representation of the vertebral bodies used here there is no explicit width of vertebrae or size of the transverse processes extending from the vertebral bodies.

Table 5.3: Rib positional offsets from the spinal canal as parameters by demographics.

	$RIBOFF_x$ (mm)					$RIBOFF_y$ (mm)					$RIBOFF_z$ (mm)				
#	I_{E-1}	A_{E-4}	S_{E-2}	H_{E-2}	W_{E-4}	I_{E-1}	A_{E-3}	S_{E-2}	H_{E-1}	W_{E-3}	I_{E-1}	A_{E-3}	S_{E-2}	H_{E-1}	W_{E-3}
1	**75**	**133**	**-106**	**449**	**77**	**94**	**40**	**-222**	**65**	**-17**	**-75**	**45**	45	13	**-60**
2	**87**	**171**	**-114**	**404**	17	**73**	**41**	**-163**	**66**	**-22**	**-74**	**59**	14	-23	**-42**
3	**95**	**159**	**-132**	**329**	46	**47**	**44**	**-130**	**52**	**-11**	**-63**	**38**	-7	**-36**	**-30**
4	**84**	**151**	**-122**	**366**	29	32	**48**	**-125**	**50**	**-16**	**-55**	**29**	-27	**-48**	**-25**
5	**77**	**154**	**-115**	**402**	29	19	**38**	**-121**	**52**	**-17**	-46	**13**	-13	**-62**	**-17**
6	**83**	**149**	**-113**	**374**	**51**	7	**25**	**-132**	**52**	**-14**	**-50**	7	14	**-73**	-5
7	**84**	**166**	**-128**	**386**	**59**	-14	**16**	**-117**	**52**	-7	**-72**	7	53	**-71**	-5
8	**77**	**221**	**-131**	**443**	**62**	3	3	**-118**	**33**	-5	**-102**	10	**112**	**-65**	-4
9	**93**	**227**	**-137**	**381**	**83**	17	-7	**-102**	20	-4	**-83**	**13**	**127**	**-83**	-2
10	**93**	**207**	**-122**	**458**	**69**	13	-8	**-83**	17	-3	**-110**	4	**187**	**-66**	-7
11	**96**	**246**	**-155**	**540**	**76**	9	0	**-83**	7	-1	**-72**	**-15**	**187**	**-75**	1
12	**117**	**297**	**-174**	**485**	51	-3	-5	**-49**	7	2	**-73**	**-23**	**75**	**-55**	8

As such, that information is embedded in the offsets reported in Table 5.3, however this representation is still deemed adequate for its purpose of placing ribs in an anatomically correct position within the thorax.

5.3 Sternal parameterization

The sternum is a unique bone in the body, actually made up from a number of smaller sternal bodies that ossify during early development and childhood, and fuse later in adolescence. Specifically, the sternum in a fully grown adult consists of a *manubrium*, a sternal body, and a xyphoid process as shown in Figure 5.7 Sobotta (1911).

In order to describe an outline of the sternum in its local plane, we place landmarks in the center of every notch between the sternum and its connecting costal cartilage. This was done using a custom interface written in MATLAB which provides reformatted views through the curved surface of the chest wall in which the rib notches are easily visualized as shown in Figure 5.8. Each notch can then be parameterized by its position with respect to a local sternum coordinate system or plane, which is set up as follows:

- The origin sits at the sternal angle – specified as the mid-point of the two 2nd rib

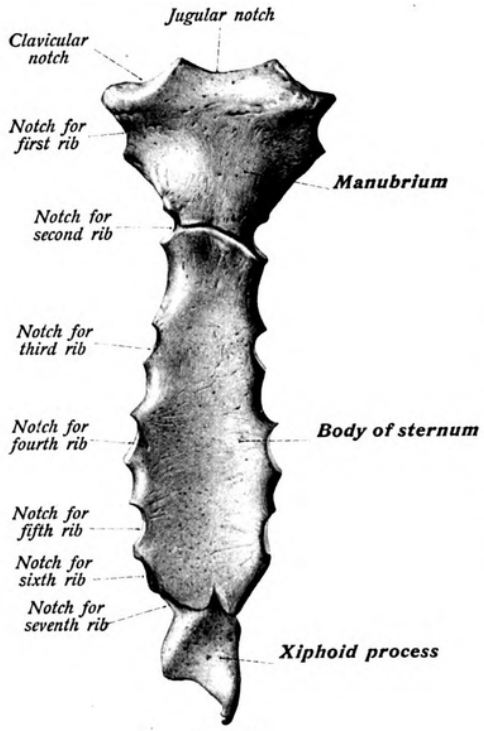

Figure 5.7: Sternum anatomy showing notch locations (Sobotta, 1911).

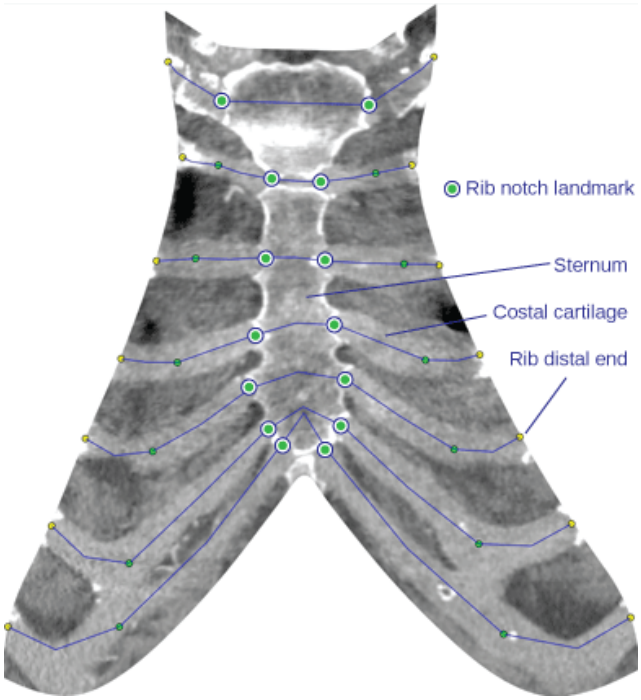

Figure 5.8: Landmark placement for rib notches on sternum.

sternal notches

- The plane z-axis extends from the origin through the mid-point of the two 7th rib sternal notches

- The lateral x-axis is perpendicular to the primary axis, pointing in the average left to right direction specified by each left-right pair of notch landmarks 1 through 7

Evaluated with respect to this plane, each notch location (for ribs 1–7, left and right) has a local x-, y-, and z-component. Data for the left and right sides were averaged such that only one set of 7 rib levels is used (i.e., lateral symmetry is assumed), and the x-coordinate is specified as a positive lateral offset from the midline of the sternum. The resulting demographics-based regression coefficients for each of these local plane coordinates are given in Table 5.4.

Table 5.4: Sternal notch position parameters with respect to the local sternal plane.

	$STNOTCH_x$ (mm)					$STNOTCH_y$ (mm)					$STNOTCH_z$ (mm)				
#	I_{E-1}	A_{E-3}	S_{E-2}	H_{E-1}	W_{E-3}	I_{E-1}	A_{E-3}	S_{E-2}	H_{E-1}	W_{E-4}	I_{E0}	A_{E-3}	S_{E-1}	H_{E-1}	W_{E-4}
1	**187**	-17	**-238**	**66**	-6	-2	25	28	68	55	13	-14	-11	**116**	-105
2	-16	19	-24	75	2	0	0	-0	-0	-0	0	0	-0	-0	-0
3	84	-8	-123	43	-8	51	1	-112	-37	-113	**-20**	1	**30**	-69	23
4	55	-9	-46	73	-12	38	-12	-125	-33	-117	**-35**	1	**52**	**-141**	78
5	73	-14	-102	64	-5	22	-13	-49	-17	-146	**-57**	15	**81**	-143	25
6	-48	22	-1	87	9	**76**	-4	**-98**	**-43**	-78	**-71**	7	**93**	-146	47
7	-69	18	33	61	**26**	0	0	-0	-0	-0	**-71**	-21	**101**	-189	-34

5.3.1 Sternal plane position and orientation

With the outline of a sternum within its own local plane provided by the parameters $STNOTCH_{[x|y|z]}$, it is now necessary to place and orient the sternum appropriately in the body. Its position can be described with reference to nearby anatomical landmarks. For example, the offset between the sternum and the spine could be measured, and the sternum plane placed based on that parameterization. We chose instead to use the ribs themselves

as a reference geometry, and parameterized the position of the sternal angle with respect to the distal ends of the 2nd ribs as shown in Figure 5.9. Descriptions of the three parameters required for this scheme are below, and results for demographic coefficients predicting these parameters are given in Table 5.5.

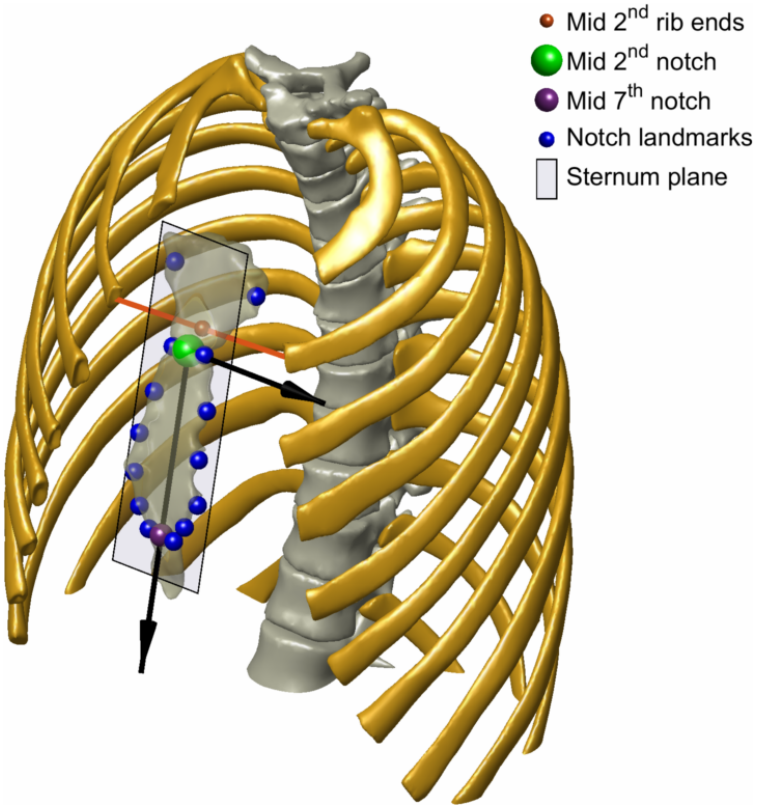

Figure 5.9: Sternum plane placement and orientation. The plane origin (largest sphere marker) is parameterized by its offset ($STNM_{[y|z]Offset}$) from the midpoint between 2nd rib distal ends (smallest sphere marker). The sternum plane pitch ($STNM_{pitch}$) is measured against the vertical axis in the sagittal view.

***STNM*$_{pitch}$** is the pitch angle (deg) that the sternum plane makes with the scan Z-axis. Lower $STNM_{pitch}$ angles result in more vertically oriented sternum. Symmetry is assumed, so other angles (roll or twist left/right) remain zeroed.

***STNM*$_{yOffset}$, *STNM*$_{zOffset}$** specify the offset distances (mm) from the midpoint between the distal ends of the left and right 2nd ribs to the origin of the sternum plane in global Y (anterior) and Z (superior) directions.

Table 5.5: Sternum plane parameters describing the position and orientation of the sternum with respect to the 2nd rib ends.

$STNM_{pitch}$ (deg)					$STNM_{yOffset}$ (mm)					$STNM_{zOffset}$ (mm)				
$I_{E\text{-}1}$	$A_{E\text{-}4}$	$S_{E\text{-}2}$	H_{E0}	$W_{E\text{-}2}$	$I_{E\text{-}1}$	$A_{E\text{-}3}$	$S_{E\text{-}3}$	$H_{E\text{-}1}$	$W_{E\text{-}4}$	$I_{E\text{-}1}$	$A_{E\text{-}4}$	$S_{E\text{-}2}$	$H_{E\text{-}3}$	$W_{E\text{-}4}$
347	**-971**	-439	-17	**22**	118	34	748	-104	-297	-89	-239	216	941	238

5.4 Full thoracic skeleton results

Using each of the parameterized geometries described above along with their regression coefficients to age, height, weight, and sex (which allow us to predict those parameters for a given demographic), we can collect results into a parametric model of the thoracic skeleton and rib cage.

Each individual piece of geometry can be developed in an isolated fashion based on parameters defining that geometry, and then the pieces can be combined by further parameters defining their relationships. For example, the ribs as defined by Chapters 2 and 3 form a coherent model of isolated ribs, and can subsequently be combined with the structure for a spine by specifying their relationship (i.e., positional offset and angle) from that spine. This modular approach is outlined in Figure 5.10 which shows the process for building and combining each piece of geometry.

Using the process outlined in Figure 5.10, along with the various sets of regression coefficients for the parameters needed to make geometries within that process, we can begin to build a full thoracic skeleton which, similarly to the ribs from previous chapters, can show the changes in geometry that are seen across demographics. Figures 5.11 and 5.12 shows these changes across each of the four demographic factors by taking a baseline geometry built from a young mid-size male (20 years, 175 cm, 76 kg), and then varying each of age or sex (Figure 5.11) or height or weight (Figure 5.12).

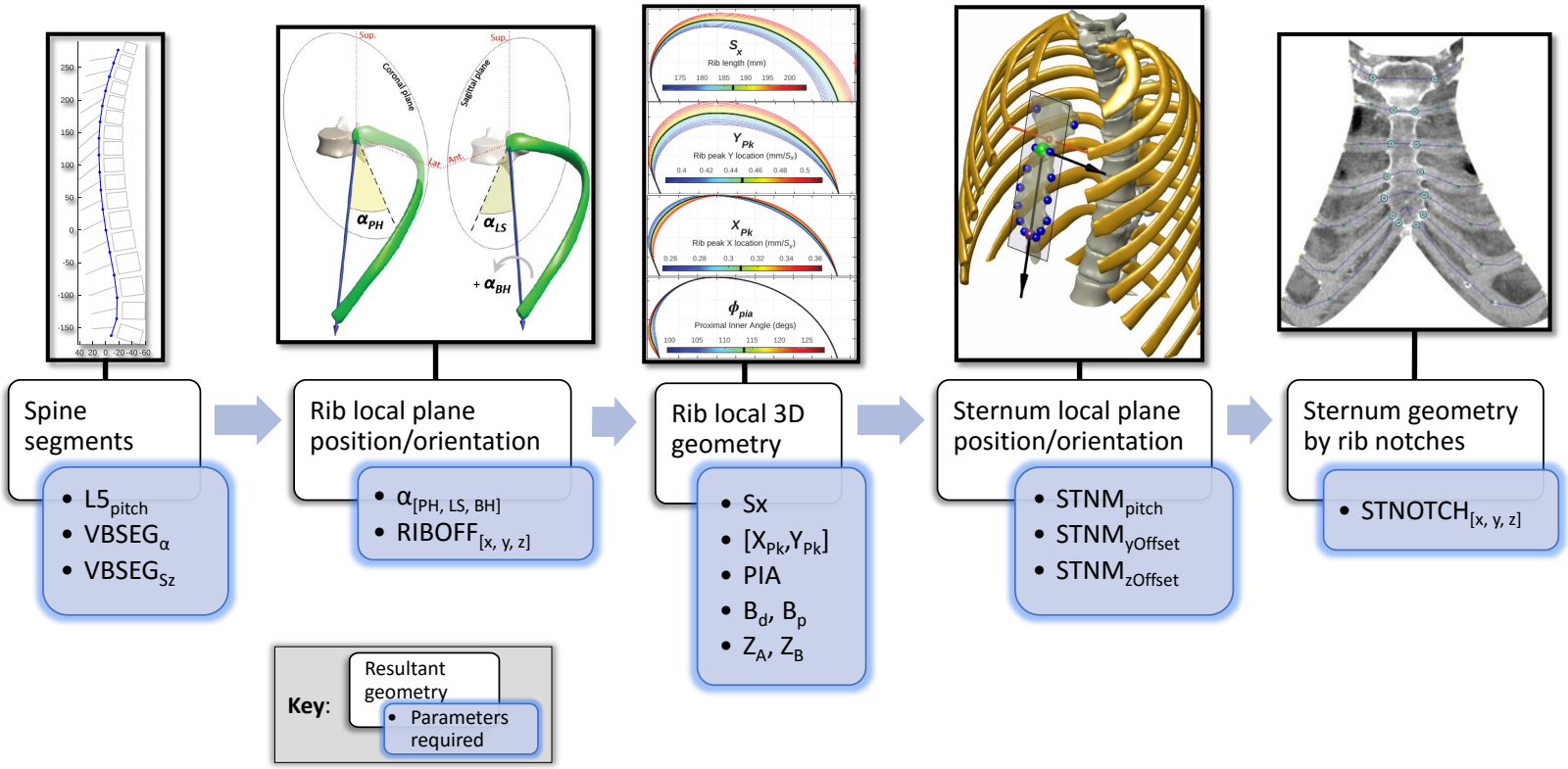

Figure 5.10: Flowchart showing the process for building the thoracic skeleton from individual parameters, beginning with the positions of vertebral bodies in the spine, followed by ribs offset from the spine, followed again by the sternum as offset from the ribs.

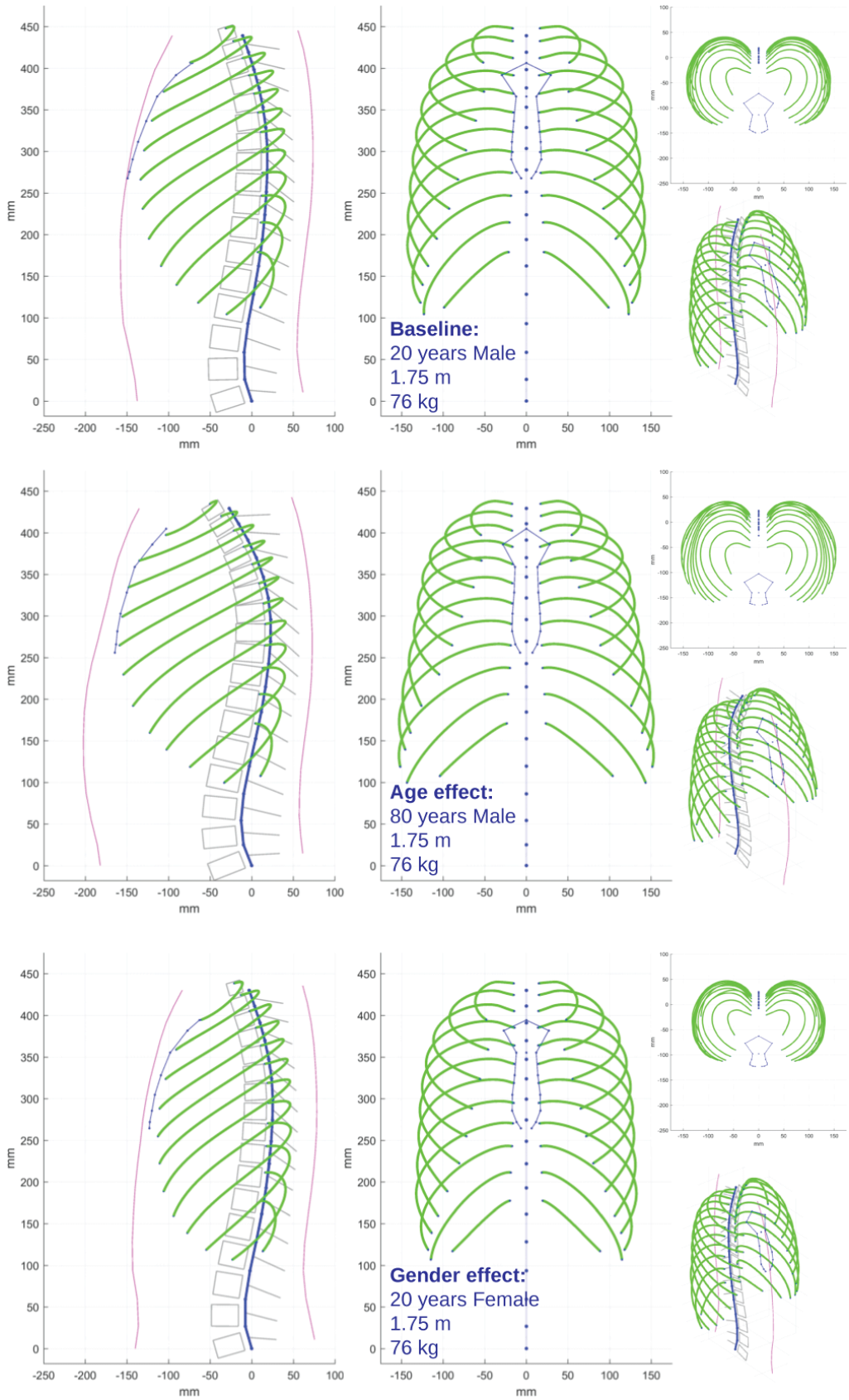

Figure 5.11: Age and sex effects on rib cage geometry.

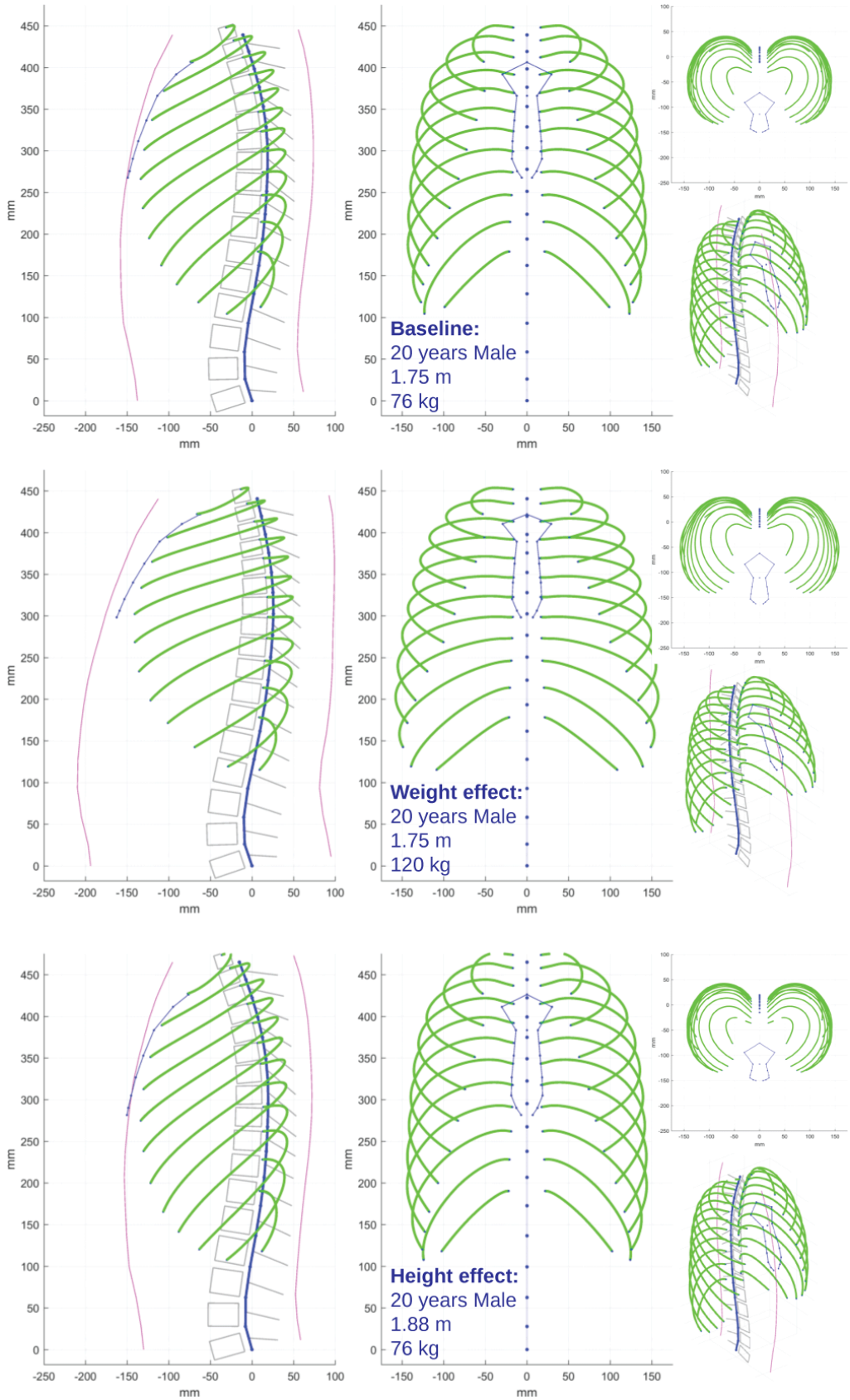

Figure 5.12: Height and weight effects on rib cage geometry.

5.5 Discussion of overall changes

5.5.1 Rib arc length

Results above showed that as age increases, the parameters Z_A and Z_B each change so as to reduce the out-of-plane deviation of ribs. In other words, as we age we tend to see ribs flattening out to become more planar. This is an important result and gives context to the changes in the in-plane rib shapes that were found with age in previous chapters. In Chapter 3 (highlighted in particular by Figures 3.13, 3.15 and 3.17) we saw that as the end-to-end length and in-plane aspect ratio of ribs increase with age, so too does their overall in-plane arc length (L_{2d}). This fact alone would be difficult to reconcile with the generally held truth that bone growth (the actual extension of long bones rather than mere remodeling) no longer occurs after skeletal maturity is reached. However when the 2D in-plane length is combined with the out-of-plane length, there is potential for increases in the former to be offset by decreases in the latter.

Testing this at the 6$^{\text{th}}$ rib level, we find that multivariate regression to L_{2d} shows that age is a small but significant factor in in-plane length ($p = 0.008$, L_{2d} increasing at $0.5\,\mathrm{mm}$ per decade). When accounting for both in-plane and out-of-plane shape, however, regression to L_{3d} no longer has age as a significant predictor of rib length ($p = 0.25$ at rib 6 and $p > 0.05$ for other mid-level ribs). In other words, results show that the overall arc length of ribs does not change significantly with age, whereas the path that the rib takes from its proximal to distal end does change with age. While it is not the focus of this thesis to investigate the underlying mechanisms that bring about this change, one hypothesis might be that repeated mechanical loading across the respiration cycle throughout a lifetime could lead to changing shape. Another possible mechanism could come from changes in material properties of the ribs and surrounding tissue that occur with age and might lead to altered stress states across the rib cage, which in turn reshape overall rib curvature.

5.5.2 Rib cage depth

Another thoracic feature of interest is that of overall chest depth (i.e., the anterior-posterior depth of the rib cage and sternum), which has implications when considering anterior loading of the thorax in MVCs. Shi et al. (2014) and Wang et al. (2016) reported an increase in overall rib cage depth with age, and results from the current work illustrated in Figure 5.11 confirm this effect, if to a slightly higher magnitude[1].

In the current study, the choice for sternum position is specified by the relative location of the 2nd rib notch to the distal ends of the 2nd ribs. As highlighted by Table 5.5, none of the resulting offset coefficients were seen to be significantly different from zero. Specifically, $STNM_{yOffset}$ indicates an independent effect of age is to shift the sternum only marginally more anteriorly from the ribs, at a rate of just $0.34\,\mathrm{mm}$ per decade. These results help to explain that the primary source of that depth increase of the chest comes from changes to the ribs themselves, rather than any relative shift of the sternum due to changes in costal cartilage. Specifically, the combined increases in rib α_{PH} angle and span S_x with age serve to push the distal ends of ribs both superiorly and anteriorly from their attachment points on spine. The overall age effect is illustrated in Figure 5.13, which highlights the cumulative changes to the spine (increased kyphosis) and ribs (as above) that serve to bring the anterior aspect of the chest further anteriorly with increasing age.

[1] Chest depth is not explicitly reported by Shi et al. (2014); Wang et al. (2016) however figures indicate an approximate $10\,\%$ increase mid-sternum compared to $15\,\%$ in the current work.

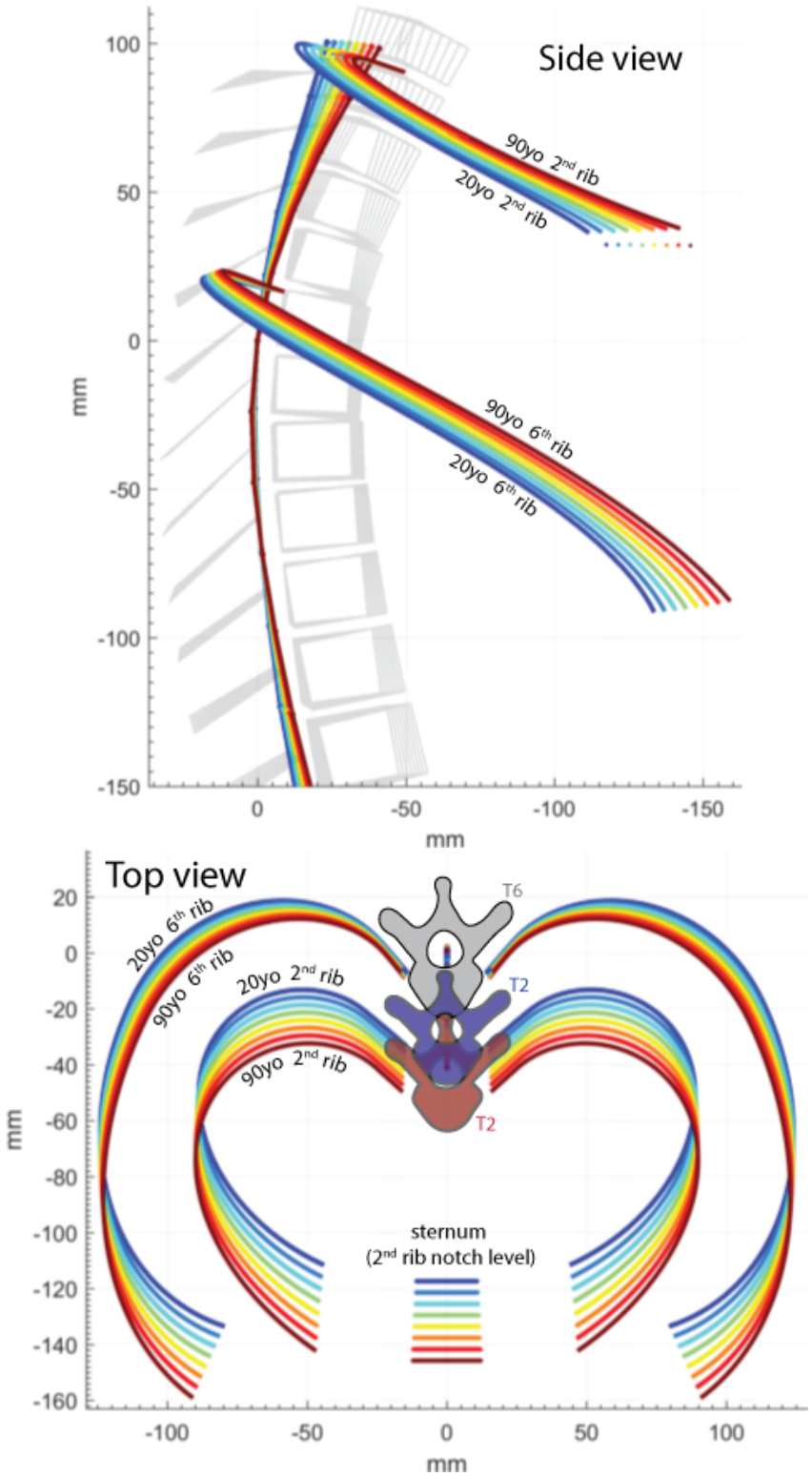

Figure 5.13: Age effect on rib cage shape and depth for F50 (162 cm, 73 kg) females ranging from 20 to 90 years of age at 10-year increments. All individuals are centered at their T6 vertebra, and ribs 2 and 6 are shown along with the position of the sternum 2nd rib notches.

5.5.3 Spine curvature

In order to compare results for the spine to past literature, Figure 5.14 shows the thoracic spine curvatures of a 20 year-old and 80 year-old man with $175\,\mathrm{cm}$ height and $25\,\mathrm{kg/m^2}$ BMI predicted by the demographics-based regression models, and those reported by two previous studies (Gayzik et al., 2008; Wang et al., 2016). The two previous studies used a point cloud of landmarks placed on vertebral bodies (with each study choosing slightly different vertebral locations), rather than the spinal canal as has been used in here. The methodology for developing spine geometry in the previous studies was a combination of GPA and PCA of the coordinate positions for the cloud of landmarks, which differs from the currently presented parameterization scheme. Another difference is the number and source of subjects in each study (63 for Gayzik et al. (2008) and 101 for Wang et al. (2016)). Here we have included a broader population base (of approximately 1000 subjects), and have used a specific parameterization that directly uses intrinsic geometric properties of the spine. Despite the differing methodologies, all studies show increased kyphosis with increased age.

When validating the results for accurate reflection of real spine curvature when that geometry was originally obtained using PCA, one might choose local measures such as the relative angle between vertebrae, and then assess whether the results obtained from the predicted geometry match well to the values seen throughout the population. One advantage of the parameterization scheme used here is that we are directly incorporating such measures into our parameterization, ensuring that there is no discrepancy between the expected values from the population and the actual produced geometry. This advantage is reflected in the plotted measures for vertebral angles shown in Figure 5.15, where it can be seen that the current results produce much smoother spine curvature than the two reference studies. It is unlikely, for example, that the T6 and T7 vertebrae differ in relative angle by almost $20°$ (as seen in Figure 5.15 for the Gayzik et al. (2008) 80 year-old). This particular example may come from an anomaly in the original dataset used in that study, however it

is also clear from Figure 5.15 that the methodology and population used here provide (by design) spine curves free of such anomalies.

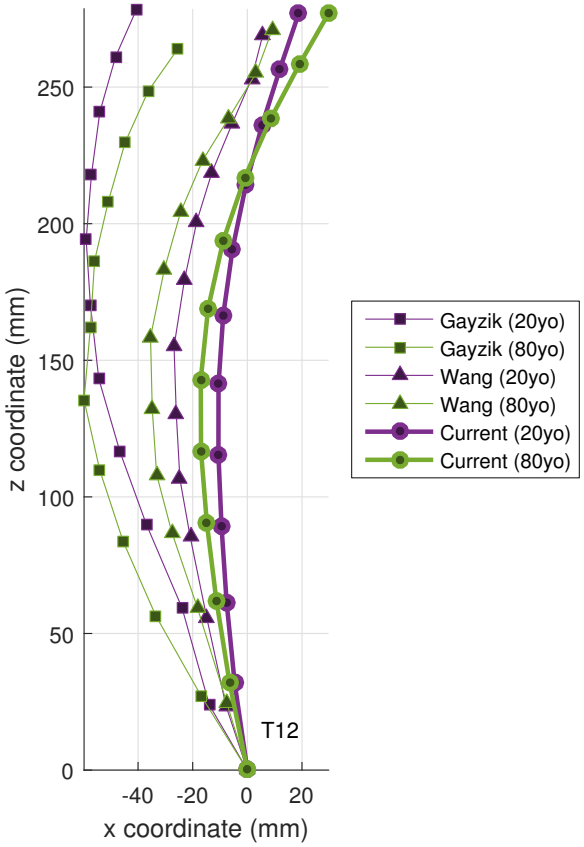

Figure 5.14: Age effect on thoracic spine curvature for 175 cm men with BMI 25 (weight 76 kg). Comparative values shown for two previous studies, however methodology differs with only the current study using spinal canal points for landmarks.

Another way of validating the resulting spine geometry is to use global measures of spine curvature. A standard clinical measure is the Cobb angle, which is derived from the inner angle in the sagittal plane subtended between the superior end-plate of the T4 vertebra and the inferior end-plate of the T9 vertebra. Taking end-plate surfaces as lying perpendicular to the spinal canal, this T4–T9 Cobb angle was measured from the CT scans in the adult population, resulting in a mean and standard deviation of 26.4° and 8.7°, respectively. This matches well to a population of adults without disease or skeletal deformity measured by Goh (2000), which had mean Cobb angles of 28.5° with standard deviation of 10.7°. Using linear regression of demographic factors to Cobb angle results within the

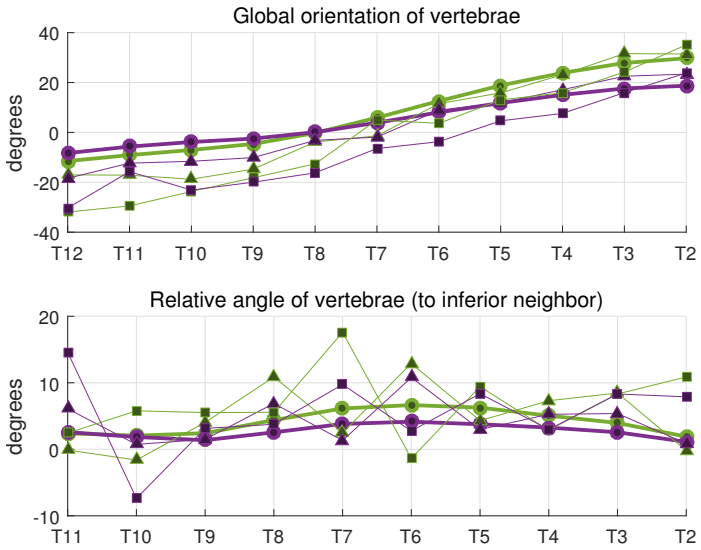

Figure 5.15: Age effect on thoracic spine curvature for $175\,\mathrm{cm}$ men with BMI 25 (weight $76\,\mathrm{kg}$). Comparative values shown for two previous studies, however methodology differs with only the current study using spinal canal points for landmarks.

current CT population, the independent effect of age was seen to increase Cobb angle by $1.7°$ per decade ($p < 0.001$). To validate that spines recreated using the current method of segment-wise parameters for segment height and relative angle, a series of M50 male spines were rebuilt based on the demographics regression models to spine parameters. Correspondingly, the predicted values based on regression from within the population for those same demographics were calculated. Figure 5.16 shows that the trend of increasing Cobb angle with age is well matched by the rebuilt spine shapes, albeit with a slightly higher rate of change ($2.2°$ per decade).

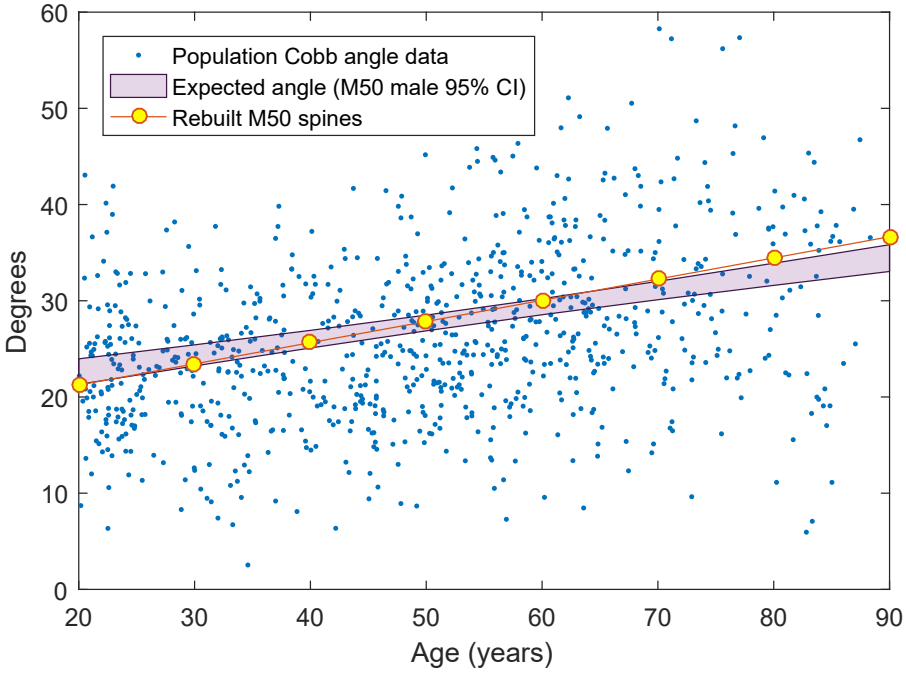

Figure 5.16: Comparison of T4–T9 Cobb angles between the expected values as measured directly from the population, and the resulting values from building spines via parameterized segments.

5.6 Discussion of methodology

This chapter has described a modular approach to the geometric modeling of thoracic anatomy. The focus has been on targeted models of individual anatomic components along with targeted models of those components' relationships. To conclude the chapter we will discuss the differences between this approach and that of the more generalized technique of using GPA and PCA to quantify shape via a cloud of homologous landmarks placed across the thoracic skeleton. The general methodology for using GPA and PCA is, broadly speaking, a 3-step process:

1. Perform GPA on the point clouds of landmarks from multiple subjects to minimize variance in their shared position and orientation.

2. Perform PCA to capture the principal components (directions and magnitudes) of the remaining variance between subjects' landmarks.

3. Use regression to describe those principal components in terms of demographic factors such as age.

Using the methodology above all landmarks are free to translate in independent directions driven by their principal components, and their accumulated movement provides for non-linear "morphing" of the point cloud (as opposed to linear scaling of the cloud as a rigid body) with changes in the predictive demographic factors. However, one property of the PCA methodology when applied to a whole rib cage (Gayzik et al., 2008; Shi et al., 2014; Wang et al., 2016) is that each of the individual landmarks alone are restricted to purely linear translation based on their individual principal component directions. In other words, when considering any given landmark across the rib cage, its position when predicted by PCA for any arbitrary age will always lie along a single vector in space. When predicted via linear regression, the "movement" of a landmark along this vector will be constant (with, say, increasing age). When using regression analyses with higher powered terms or other non-linear coefficients the movement of a landmark will no longer be constant with age, yet it will still be restricted to the same linear path. As stated above, the accumulated effect of movement from multiple landmarks can make for non-linear change in the overall structure, which is likely to be sufficient for many aspects of anatomic variation. However, there are forms of movement that are not possible to represent using purely linear changes.

The modular approach which has been used in this chapter overcomes this constraint by modeling individual aspects of geometry as separable components and allowing their combined results to dictate final landmark positions. For example, if the physical representation of changes in rib angle are well modeled by a rotation around their articulation point at the spine, then a landmark at the rib distal end would follow an arced trajectory as rib angle changes. This arc trajectory would be approximated by a best-fitting straight line using a PCA-based methodology, but would be modeled directly using the modular approach taken in this chapter which explicitly uses rib angle as a model parameter. This approach is sim-

ilar to that used by Weaver et al. (2014) who applied GPA models to individual ribs, then quantified each rib's position and orientation under separate analyses. It should be stressed that such approaches are not free of all mathematical constraints on landmark position. Instead, constraints are distributed across the individual models of geometry that are used for each piece of anatomy. In that sense, it is important when using the modular approach to select individual models that realistically represent their targeted pieces of anatomy.

One way of assessing the accuracy of modeled geometry is to compare the geometric features of any resulting geometry to those same features as measured from within an underlying population. This can be done using a PCA methodology by simply taking measurements (such as local rib, spine, or sternum measures, or indeed aggregate measures of chest depths, spine shape, etc.) from the resultant geometry after it has been predicted by demographic factors. However, a point which has been stressed throughout this thesis is the importance of incorporating as many of these same geometric measures as possible as direct parameters to any modular parametric model of geometry. This is reflected in the choices for rib shape model parameters to directly include rib size, aspect ratio, skewness, and orientation angles, along with choices for other anatomy such as vertebral segment size and relative angle to represent spine curvature. By explicitly making these choices for model parameters we ensure that the most accurate estimate (at least to the accuracy of the regression model used) of such geometric properties is provided.

Another advantage of the modular approach is that it results in meaningful model parameters that are easily understood. A well-known drawback to PCA-based models is that their output coefficients have no direct meaning (other than their mathematical representation of the principal components), and are interpreted or understood only indirectly by observation of their effects on the underlying structure. With the modular approach used here, however, each separate parametric model can be designed to include physically meaningful parameters such that their values can immediately provide insight. This is advantageous when trying to understand trends across demographic populations since regression

coefficients to demographic factors inherently provide the magnitude and direction of those changes. Importantly, such results also allow direct comparisons even to individuals who were not part of an original study population.

Overall, a primary feature of the modular approach is that intent can (and in fact should) be built into each anatomic component. If a researcher intends to evaluate the final model's accuracy in terms of specific geometric properties (say, rib angle or rib aspect ratio), then whenever possible, it is beneficial to include those geometric properties as directly modeled parameters. While this takes additional effort in terms of component model design than what a single generalized approach would require, it also has the potential to increase model accuracy, make it easier to assess that accuracy, and importantly, enhance the utility of the model as an explanatory tool. In this chapter we have used the modular approach to quantitatively describe thoracic anatomy, and have shown its explanatory power for describing changes across demographics at both the individual component level, and also at the level of a combined model of the overall thoracic skeleton.

CHAPTER 6

Conclusions

The thoracic skeleton is a complex structure consisting of multiple, differently shaped bones arranged to collectively form a cage that protects vital organs such as the heart, lungs, and major blood vessels. On the scale of populations, the geometry is further complicated by the fact that no two bodies are equivalent. Considerable variation is seen at every level of anatomy from overall chest sizes and aspect ratios, through to positioning and orientation of bones within the chest wall, and further still to the local curvature or geometric makeup of those bones.

Thoracic injuries occur at high rates in MVCs and are associated with increased mortality. Particularly in frontal crashes where the body is loaded through the chest, both chest deformation and rib fractures play a major role in these outcomes. Current physical ATD models and computational human body models are used as tools for engineers to improve occupant protection in the event of a crash. Recent trends suggest that a number of vulnerable populations are at higher risk of injury or death than the general population and may require specific attention in order to provide protection that is more tailored to their body makeup. These vulnerable populations tend to have demographic factors that are not typically represented in ATDs; they instead lie towards the extremities of population distributions in those factors, such as obese or elderly occupants who are at the upper ends of the weight and age spectrum, respectively. Similarly, females are underrepresented in the physical or computational models available today, a fact that no doubt contributes to

their increased risk of injury in a number of MVC scenarios. With each vulnerable population subgroup varying considerably in their makeup, no single model of their geometry is likely to offer the most benefit to engineers. Instead a more flexible modeling approach that has the ability to represent a greater breadth of the population is preferred. This thesis examines thoracic geometry from a broad population and aims to contribute to the body of knowledge that is required to build such a modeling system.

6.1 Study conclusions

This thesis has explored variations in thoracic geometric seen in the adult population and takes particular focus on the overall geometric makeup of human ribs. Revisiting the research goals set out in the Introduction, in studying population variability we have also attempted to address the following questions: What is the effect of age on the geometry of the ribs and the rib cage, and do any such changes have mechanical consequences in terms of the response of the body when subjected to loading?

The primary aspect of geometry that has been addressed in this thesis is the overall in-plane shape of human ribs. As an answer to the first part of the question above, we can conclude that significant shape changes to the ribs do in fact occur with age. Taking the 6$^{\text{th}}$ rib level as an example, we have found that the distance or span between ribs ends (S_x) tends to increase at a rate of $2.6\,\mathrm{mm}$ per decade. Correspondingly, the height of a rib in its local plane decreases resulting in an increased aspect ratio – represented in this thesis by reductions with age in the Y_{Pk} rib shape parameter. Coupled with results from Chapter 5 that also show a reduction in the out-of-plane deviation with age, this newly discovered in-plane age effect does not point to an overall lengthening of the rib as a whole, but instead suggest a reshaping of its centroidal path to form a flatter and more elongated curvature in older individuals (a change which best described graphically in any of Figures 3.10, 3.14, 3.16 and 5.13).

The second part of the question above is addressed via simulations presented in Chapter 4 that are aimed exclusively at isolating the effect of rib shape on its stiffness when subjected to simple loading conditions. Results found that the contribution to stiffness in axial loading that is brought about by shape was indeed seen to increase with age. Using the stiffness of typical 20-year-old rib shapes as a baseline, an approximately $14\,\%$ increase in stiffness was seen when loading typical 80-year-old rib shapes from otherwise equivalent demographics.

6.2 Study contributions

The specific contributions of this thesis are:

1. A new mathematical model of human rib shape. The six-parameter shape model presented in Chapter 2 offers the most accurate mathematical model to date for representing the in-plane shape of a rib's geometry. It uses logarithmic spirals and a simpler and more direct set of parameters than previous models, which leads to an improved ability to aggregate ribs to produce statistically generated rib shapes, and those resulting shapes have a higher degree of curvature continuity.

2. A predictive model for generating rib shapes based on population statistics, providing rib geometry that is representative of a given demographic specified in terms of age, height, weight, and sex. The statistical model provided in Chapter 3 is given in the form of a compact matrix of coefficients passed to linear regression models for each shape parameter. The resulting ribs are shown to match well to other measures of shape not explicitly included in the parameterization scheme. Its use in building flexible population-based models is demonstrated by the production of typical rib shapes from all rib levels that are representative of targeted groups from broadly sampled demographics factors.

3. A previously unreported outcome resulting in new information for the crash safety community regarding the relative effect of age on rib geometry. Older ribs are seen to have longer span with flatter overall curvature (both in-plane and out-of-plane). This change in centroidal geometry is found to be more strongly related to the independent effects of age than previously reported age-related changes in the angle of ribs in the sagittal plane.

4. An analysis of the likely independent effect of the identified shape changes on the mechanical stiffness of ribs to loading. The results of this analysis are useful to users and developers of human body computational models who wish to incorporate the concept of person age into their work. Results provide these researchers with the information that there is an approximately $14\,\%$ relative difference in rib stiffness under anterior loading between young and old adult models that comes about via the identified changes with age in overall rib shape.

5. A new parametric technique for building a scaffold model of the thoracic skeleton. Based on a similar methodology to the parametric rib shape model, we combine independent modeling of the spine via vertebral segments, the sternum via its rib notch locations, and other parameterizations for spatial relationships between parts of the body, and the resulting whole gives a coherent geometric representation of the thoracic cage. The modular approach once again uses direct measures of anatomy where possible in its parameterization. This helps ensure that any resulting geometry built from statistical operations on parameters will reflect shape properties that would be expected if measured directly from within the original population.

6.3 Applications and future work

The work presented in this thesis can be either applied or extended in a number of directions. The fields of application include clinical settings that may benefit from quanti-

tative measures of rib shape for the diagnosis of disease or deformity or for the treatment of injury. Results are also relevant to research into the biomechanical properties of ribs and the rib cage, particularly those addressing population variability in these properties. This thesis will conclude with a selection of specific applications to which its contents could be applied, along with the areas of future research that could improve upon its results.

6.3.1 Device design

One property of logarithmic spirals is that the curvature along their length is not constant, but instead changes continuously around rotational coordinate positions. The exceptionally strong fit between logarithmic spirals and true rib geometry highlighted by this thesis suggests that ribs also possess this property of continuous change in curvature along their length. SRF devices are built to span a large enough segment of the rib so as to stabilize a region containing one or more fractures, and consequently the precise local curvature at each fixation point is likely to be different, at least to some small degree. Some SRF devices are manufactured to a predetermined radius of curvature, in many cases a constant curvature. Results from this thesis suggest that in such cases, compliance between device and cortical surface may be better at one fixation end than the other, leaving potential for an improvement in device design based on the adoption of a device built with varying curvature along its length. Furthermore, given limitations on the number of devices expected to be held at any one institution, the population data presented in Chapter 3 would be an excellent source from which to select the particular curvature parameters in those devices that would provide best coverage for their intended recipients.

6.3.2 Computational modeling

In its current form, the results presented in this thesis regarding predicted shapes of ribs and the rib cage can be used to assess the geometry of currently available human body models. Shi et al. (2014); Wang et al. (2016); Weaver et al. (2014) have each presented

shape models for the thorax that have been used to morph geometry based on the same demographics factors that are considered here, and the results from this thesis are ideally placed to help verify the results from those studies. For example, each of the studies listed includes methods to adjust overall rib geometry, and thus produce new rib shapes that are intended to represent a chosen demographic. Intrinsic geometry measurements from those new rib shapes such as their size, aspect ratio, and skewness could be measured for comparison to the values measured from the large population that is reported in this study. Similarly, and as has been presented in Chapter 5 with regards to spine curvature and chest depth, the accumulated effects of individual body component changes can lead to more global changes that could be used to assess body size and shape. Such validation is routinely performed for global measures of thorax shape, and adding the validation of local measures to those morphing methodologies would allow for easier identification of potential mismatches between the intended target and the regenerated body geometries, consequently adding to the veracity of those morphing tools.

The model of the thoracic skeleton itself as presented in Chapter 5 provides a similar opportunity to develop a body morphing scheme that can drive modifications of existing FE models of the thorax to fit specific target demographics. The model as presented does use some simplifications in its geometry that would need to be considered before it is applied to a full 3D node and element cloud. For example, morphing handles work best when they fully surround a given geometry, thus making the transformation of geometry to new positions a matter of interpolation within the handles rather than extrapolation. The choice of simplified scaffolding (ribs as a single curve, spine as a series of segment lines) means that no cross-sectional morphing of any bony geometry would be feasible and thus would need to be handled appropriately by additional morphing constraints. Nevertheless, such considerations are needed for almost all forms of mesh morphing, and the model presented in this thesis has additional benefits from its direct use of geometric measures that would address a number of questions in terms of accuracy that often come from morphing of

human body geometry.

6.3.3 Future directions

As noted in the discussion of Chapter 3, the shape model presented for ribs is focused on the central axis of the rib and does not capture cross sectional geometry or other changes in rib cortical surfaces that may vary across the population. Perz et al. (2015) has explored the potential for cross sectional geometry of the ribs to be extracted from clinical and other higher resolution CT scans. Results there showed that higher resolution scans were capable of discerning cortical bone cross sectional surface to an acceptable accuracy, and conclusions included a provision that error in the determination of the rib geometrical properties due to limited image resolution in clinical CT could most likely be reduced by the development of correction functions based on direct comparisons to higher resolution scans. This suggests that, as long as measures could be taken to a sufficient accuracy from clinical scans, the population and image data utilized in this study could also be used to explore aspects of cross sectional rib geometry. This is likely to be limited to a subset of the higher resolution scans and comprise gross measures of cross-section rather than precise cortical thickness; however, a description of changes in those measures across the population would provide a basis to expand upon the results that have been presented in this thesis for overall rib shape.

Another area of future work is to extend the population considered in this thesis, as here were we have focused only on the adult population. This has been, in part, so as to separate changes in geometry that occur after skeletal maturity from the changes during growth, as these changes are driven by substantially different biological processes. Doing so has meant that simpler statistical representations of change (i.e., linear change with age) have been appropriate for our purposes. Nevertheless, the corresponding application of the shape model presented here to children will enhance our understanding of the geometric changes during growth and is a valuable direction of future research. Furthermore, a non-linear

statistical model that appropriately treats the multiple growth periods to adolescence, the transition period to adulthood, and indeed the various stages of aging would be a significant step towards a truly universal modeling system that is inclusive to people of all ages.

Finally, the skeletal geometry of the thorax is one part of a much larger whole. There is space to apply the techniques used here to other aspects of anatomy to similarly understand their variation across the population. Within the chest wall, the costal cartilage, intercostal and surrounding musculature, joint spaces, and further sternum or clavicular parameterizations would be ideal targets for expanding the scope of the work presented here. All of these components, and indeed aspects beyond mere geometry such as the material composition of those components, play key roles in the response of the chest to loading. In order to include material parameterizations, medical imaging alone (from CT in the case of this thesis) does not directly provide the material composition output required for FE modeling of a given tissue's mechanics. However, where experimental testing has produced population corridors for particular material properties, there is the possibility that coupling of those corridors to other features measured from clinical imaging (and hence from a wide population of individuals) can be achieved.

Bibliography

H. Abdulrahman, I. Afifi, A. El-Menyar, A. Al-Hassani, A. Almadani, H. Al-Thani, and R. Latifi. Clinical outcomes of multiple rib fractures: does age matter? *European Journal of Trauma and Emergency Surgery*, 39(6):605–611, Apr. 2013. ISSN 1863-9941. doi: 10.1007/s00068-013-0291-5. URL http://dx.doi.org/10.1007/s00068-013-0291-5.

A. M. Agnew, M. Schafman, K. Moorhouse, S. E. White, and Y.-S. Kang. The effect of age on the structural properties of human ribs. *Journal of the Mechanical Behavior of Biomedical Materials*, 41:302–314, Jan. 2015. ISSN 17516161. doi: 10.1016/j.jmbbm.2014.09.002. URL http://dx.doi.org/10.1016/j.jmbbm.2014.09.002.

E. Arajärvi and S. Santavirta. Chest injuries sustained in severe traffic accidents by seatbelt wearers. *The Journal of Trauma*, 29(1):37–41, Jan. 1989. ISSN 0022-5282. doi: 10.1097/00005373-198901000-00007. URL http://dx.doi.org/10.1097/00005373-198901000-00007.

W. S. Bartynski, M. T. Heller, S. Z. Grahovac, W. E. Rothfus, and M. Kurs-Lasky. Severe thoracic kyphosis in the older patient in the absence of vertebral fracture: association of extreme curve with age. *American Journal of Neuroradiology*, 26(8):2077–2085, Sept. 2005. ISSN 0195-6108. URL http://view.ncbi.nlm.nih.gov/pubmed/16155162.

N. Beadle, T. L. Burnett, J. A. Hoyland, M. J. Sherratt, and A. J. Freemont. A novel ex vivo model of compressive immature rib fractures at pathophysiological rates of loading. *Journal of the Mechanical Behavior of Biomedical Materials*, 51:154–162, Nov. 2015. ISSN 17516161. doi: 10.1016/j.jmbbm.2015.06.031. URL http://dx.doi.org/10.1016/j.jmbbm.2015.06.031.

F. Bellemare, A. Jeanneret, and J. Couture. Sex differences in thoracic dimensions and configuration. *American Journal of Respiratory and Critical Care Medicine*, 168(3):305–312, Aug. 2003. ISSN 1073-449X. doi: 10.1164/rccm.200208-876OC. URL http://dx.doi.org/10.1164/rccm.200208-876OC.

F. Bellemare, T. Fuamba, and A. Bourgeault. Sexual dimorphism of human ribs. *Respiratory Physiology & Neurobiology*, 150(2-3):233–239, Feb. 2006. ISSN 1569-9048. doi: 10.1016/j.resp.2005.04.002. URL http://dx.doi.org/10.1016/j.resp.2005.04.002.

J.-F. Bellemare, M.-P. Cordeau, P. Leblanc, and F. Bellemare. Thoracic Dimensions at Maximum Lung Inflation in Normal Subjects and in Patients With Obstructive and Restrictive Lung Diseases. *Chest*, 119(2):376–386, Feb. 2001. ISSN 0012-3692. doi: 10.1378/chest.119.2.376. URL http://dx.doi.org/10.1378/chest.119.2.376.

E. Bergeron, A. Lavoie, D. Clas, L. Moore, S. Ratte, S. Tetreault, J. Lemaire, and M. Martin. Elderly trauma patients with rib fractures are at greater risk of death and pneumonia. *The Journal of Trauma*, 54(3):478–485, Mar. 2003. ISSN 0022-5282. doi: 10.1097/01.TA.0000037095.83469.4C. URL http://dx.doi.org/10.1097/01.TA.0000037095.83469.4C.

D. Bose, M. Segui-Gomez, ScD, and J. R. Crandall. Vulnerability of Female Drivers Involved in Motor Vehicle Crashes: An Analysis of US Population at Risk. *American Journal of Public Health*, 101(12):2368–2373, Dec. 2011. ISSN 1541-0048. doi: 10.2105/ajph.2011.300275. URL http://dx.doi.org/10.2105/ajph.2011.300275.

E. M. Bulger, M. A. Arneson, C. N. Mock, and G. J. Jurkovich. Rib fractures in the elderly. *The Journal of Trauma*, 48(6), June 2000. ISSN 0022-5282. URL http://view.ncbi.nlm.nih.gov/pubmed/10866248.

Z. Cai, F. Lan, J. Chen, and F. Zhao. Development and Validation of a Finite Element Model of the Human Thoracic for Rib Fractures Prediction in Automobile Collisions. In *Proceedings of the FISITA 2012 World Automotive Congress*, volume 197 of *Lecture Notes in Electrical Engineering*, pages 375–388. Springer Berlin Heidelberg, 2013. doi: 10.1007/978-3-642-33805-2_31. URL http://dx.doi.org/10.1007/978-3-642-33805-2_31.

Z. Cai, F. Lan, and J. Chen. Development and validation of a human biomechanical model for rib fracture and thorax injuries in blunt impact. *Computer Methods in Biomechanics and Biomedical Engineering*, 18(9):974–980, July 2015. doi: 10.1080/10255842.2013.864642. URL http://dx.doi.org/10.1080/10255842.2013.864642.

P. M. Carter, C. A. Flannagan, M. P. Reed, R. M. Cunningham, and J. D. Rupp. Comparing the effects of age, BMI and gender on severe injury (AIS 3+) in motor-vehicle crashes. *Accident Analysis & Prevention*, 72:146–160, Nov. 2014. ISSN 0001-4575. doi: 10.1016/j.aap.2014.05.024. URL http://dx.doi.org/10.1016/j.aap.2014.05.024.

J. M. Cavanaugh, Y. Zhu, Y. Huang, and A. I. King. Injury and Response of the Thorax in Side Impact Cadaveric Tests. In *Stapp Car Crash Conference*, volume 1 of *SAE Technical Paper Series*, 400 Commonwealth Drive, Warrendale, PA, United States, Nov. 1993. SAE International. doi: 10.4271/933127. URL http://dx.doi.org/10.4271/933127.

D. Cesari and R. Bouquet. Comparison of Hybrid III and Human Cadaver Thorax Deformations Loaded by a Thoracic Belt. In *Stapp Car Crash Conference*, volume 1 of *SAE*

Technical Paper Series, 400 Commonwealth Drive, Warrendale, PA, United States, Nov. 1994. SAE International. doi: 10.4271/942209. URL http://dx.doi.org/10.4271/942209.

E. Charpail, X. Trosseille, P. Petit, S. Laporte, F. Lavaste, and G. Vallancien. Characterization of PMHS Ribs: A New Test Methodology. *Stapp Car Crash Journal*, 49:183–198, Nov. 2005. ISSN 1532-8546. URL http://view.ncbi.nlm.nih.gov/pubmed/17096274.

H.-Y. Choi, H.-W. Eom, S.-T. Kho, and I.-H. Lee. SAE Technical Paper SeriesFinite Element Human Model for Crashworthiness Simulation. In *Digital Human Modeling For Design And Engineering Conference And Exposition*, volume 1, 400 Commonwealth Drive, Warrendale, PA, United States, May 1999. SAE International. doi: 10.4271/1999-01-1906. URL http://dx.doi.org/10.4271/1999-01-1906.

J. M. Cormier. The influence of body mass index on thoracic injuries in frontal impacts. *Accident Analysis & Prevention*, 40(2):610–615, Mar. 2008. ISSN 00014575. doi: 10.1016/j.aap.2007.08.016. URL http://dx.doi.org/10.1016/j.aap.2007.08.016.

D. J. Daegling, M. W. Warren, J. L. Hotzman, and C. J. Self. Structural Analysis of Human Rib Fracture and Implications for Forensic Interpretation*. *Journal of Forensic Sciences*, 53(6):1301–1307, Nov. 2008. ISSN 0022-1198. doi: 10.1111/j.1556-4029.2008.00876.x. URL http://dx.doi.org/10.1111/j.1556-4029.2008.00876.x.

J. Dansereau and I. A. F. Stokes. Measurements of the three-dimensional shape of the rib cage. *Journal of Biomechanics*, 21(11):893–901, Jan. 1988. ISSN 00219290. doi: 10.1016/0021-9290(88)90127-3. URL http://dx.doi.org/10.1016/0021-9290(88)90127-3.

Y.-C. Deng, W. Kong, and H. Ho. SAE Technical Paper SeriesDevelopment of a Finite Element Human Thorax Model for Impact Injury Studies. In *International Congress & Exposition*, volume 1, 400 Commonwealth Drive, Warrendale, PA, United States, Mar. 1999. SAE International. doi: 10.4271/1999-01-0715. URL http://dx.doi.org/10.4271/1999-01-0715.

DOT. Traffic safety facts 2007. A compilation of motor vehicle crash data from the Fatality Analysis Reporting System and the General Estimate System, 2008.

R. H. Eppinger. On the Development of a Deformation Measurement System and Its Application Toward Developing Mechanically Based injury Indices. In *33rd Stapp Car Crash Conference*, volume 1 of *SAE Technical Paper Series*, 400 Commonwealth Drive, Warrendale, PA, United States, Oct. 1989. SAE International. doi: 10.4271/892426. URL http://dx.doi.org/10.4271/892426.

Federal Highway Administration. Distribution of licensed drivers by sex and percentage in each age groupand relation to the population. *Department of Transportation*

US Highway Statistics 1999, 2015a. URL http://www.fhwa.dot.gov/ohim/hs99/tables/dl20.pdf.

Federal Highway Administration. Distribution of licensed drivers by sex and percentage in each age group and relation to the population. *Department of Transportation US Highway Statistics 2013*, 2015b. URL https://www.fhwa.dot.gov/policyinformation/statistics/2013/pdf/dl20.pdf.

FHA. Federal Highway Administration 2009 National Household Travel Survey. url: http://nhts.ornl.gov, 2010. Accessed July 1, 2016.

M. M. Finucane, G. A. Stevens, M. J. Cowan, G. Danaei, J. K. Lin, C. J. Paciorek, G. M. Singh, H. R. Gutierrez, Y. Lu, A. N. Bahalim, F. Farzadfar, L. M. Riley, and M. Ezzati. National, regional, and global trends in body-mass index since 1980: systematic analysis of health examination surveys and epidemiological studies with 960 country-years and 9·1 million participants. *The Lancet*, 377(9765):557–567, Feb. 2011. ISSN 01406736. doi: 10.1016/s0140-6736(10)62037-5. URL http://dx.doi.org/10.1016/s0140-6736(10)62037-5.

C. D. Fryar, Q. Gu, and C. L. Ogden. Anthropometric reference data for children and adults: United States, 2007-2010. *Vital and Health Statistics. Series 11, Data from the National Health Survey*, (252):1–48, Oct. 2012. ISSN 0083-1980. URL http://view.ncbi.nlm.nih.gov/pubmed/25204692.

F. S. Gayzik, M. M. Yu, K. A. Danelson, D. E. Slice, and J. D. Stitzel. Quantification of age-related shape change of the human rib cage through geometric morphometrics. *Journal of Biomechanics*, 41(7):1545–1554, Jan. 2008. ISSN 00219290. doi: 10.1016/j.jbiomech.2008.02.006. URL http://dx.doi.org/10.1016/j.jbiomech.2008.02.006.

T. A. Gennarelli, E. Wodzin, and A. for the Advancement of Automotive Medicine. *Abbreviated injury scale 2005 : update 2008*. Association for the Advancement of Automative Medicine, 2008. ISBN 9780000002020. URL http://www.worldcat.org/isbn/9780000002020.

S. Goh. A comparison of three methods for measuring thoracic kyphosis: implications for clinical studies. *Rheumatology*, 39(3):310–315, Mar. 2000. ISSN 1460-2172. doi: 10.1093/rheumatology/39.3.310. URL http://dx.doi.org/10.1093/rheumatology/39.3.310.

S. Gordy, L. Fabricant, B. Ham, R. Mullins, and J. Mayberry. The contribution of rib fractures to chronic pain and disability. *The American Journal of Surgery*, 207(5):659–663, May 2014. ISSN 0002-9610. doi: 10.1016/j.amjsurg.2013.12.012. URL http://dx.doi.org/10.1016/j.amjsurg.2013.12.012.

A. Granetzny, M. A. El-Aal, E. Emam, A. Shalaby, and A. Boseila. Surgical versus conservative treatment of flail chest. Evaluation of the pulmonary status. *Interactive CardioVascular and Thoracic Surgery*, 4(6):583–587, Dec. 2005. ISSN 1569-9285.

doi: 10.1510/icvts.2005.111807. URL http://dx.doi.org/10.1510/icvts.2005.111807.

G. Granik and I. Stein. Human ribs: Static testing as a promising medical application. *Journal of Biomechanics*, 6(3):237–240, May 1973. ISSN 00219290. doi: 10.1016/0021-9290(73)90045-6. URL http://dx.doi.org/10.1016/0021-9290(73)90045-6.

H. Gray. *Anatomy of the human body*. Lea & Febiger, 1918.

E. Haug, H.-Y. Choi, S. Robin, and M. Beaugonin. *Human Models for Crash and Impact Simulation*, volume 12, pages 231–452. Elsevier, 2004. ISBN 9780444515667. doi: 10.1016/s1570-8659(03)12004-2. URL http://dx.doi.org/10.1016/s1570-8659(03)12004-2.

R. S. Hoke and D. Chamberlain. Skeletal chest injuries secondary to cardiopulmonary resuscitation. *Resuscitation*, 63(3):327–338, Dec. 2004. ISSN 03009572. doi: 10.1016/j.resuscitation.2004.05.019. URL http://dx.doi.org/10.1016/j.resuscitation.2004.05.019.

J. B. Holcomb, N. R. McMullin, R. A. Kozar, M. H. Lygas, and F. A. Moore. Morbidity from rib fractures increases after age 45. *Journal of the American College of Surgeons*, 196(4):549–555, Apr. 2003. ISSN 1072-7515. doi: 10.1016/S1072-7515(02)01894-X. URL http://dx.doi.org/10.1016/S1072-7515(02)01894-X.

S. Holcombe, M. Kindig, P. Zhang, C. Parenteau, P. Rabban, L. Hully, and S. Wang. Age-based predictive model of the pediatric ribcage. *JSAE Transaction*, 2013.

S. A. Holcombe, S. C. Wang, and J. B. Grotberg. Modeling female and male rib shapes with logarithmic spirals. *Journal of Biomechanics*, 2016. ISSN 00219290. doi: 10.1016/j.jbiomech.2016.07.021. URL http://dx.doi.org/10.1016/j.jbiomech.2016.07.021.

J. Hu and M. P. Reed. Focusing on Vulnerable Populations in Crashes:Recent Advances in Finite Element Human Models for Injury Biomechanics Research. *Journal Of Automotive Safety And Energy*, 3(4):295, 2012. URL http://www.journalase.com:8080/Jweb_qcaqyjn/EN/abstract/article_8508.shtml.

D. F. Huelke. The anatomy of the human chest. *The Human Thorax-Anatomy, Injury and Biomechanics, SAE P-67*, pages 1–9, 1976.

M. Iwamoto, Y. Kisanuki, I. Watanabe, K. Furusu, K. Miki, and J. Hasegawa. Development of a finite element model of the total human model for safety (THUMS) and application to injury reconstruction. In *Proceedings of the International Research Council on the Biomechanics of Injury conference*, volume 30, pages 12–p. International Research Council on Biomechanics of Injury, 2002.

A. R. Kemper, C. McNally, C. A. Pullins, L. J. Freeman, S. M. Duma, and S. M. Rouhana. The biomechanics of human ribs: material and structural properties from dynamic tension and bending tests. *Stapp Car Crash Journal*, 51:235–273, Oct. 2007. ISSN 1532-8546. URL http://view.ncbi.nlm.nih.gov/pubmed/18278600.

R. Kent and J. Patrie. Chest deflection tolerance to blunt anterior loading is sensitive to age but not load distribution. *Forensic Science International*, 149(2-3):121–128, May 2005. ISSN 0379-0738. doi: 10.1016/j.forsciint.2004.04.086. URL http://dx.doi.org/10.1016/j.forsciint.2004.04.086.

R. Kent, G. Shaw, D. Lessley, J. Crandall, D. Kallieris, and M. Svensson. Comparison of Belted Hybrid III, THOR, and Cadaver Thoracic Responses in Oblique Frontal and Full Frontal Sled Tests. In *SAE 2003 World Congress & Exhibition*, volume 1 of *SAE Technical Paper Series*, 400 Commonwealth Drive, Warrendale, PA, United States, Mar. 2003a. SAE International. doi: 10.4271/2003-01-0160. URL http://dx.doi.org/10.4271/2003-01-0160.

R. Kent, B. Henary, and F. Matsuoka. On the fatal crash experience of older drivers. In *Annual Proceedings/Association for the Advancement of Automotive Medicine*, volume 49, page 371. Association for the Advancement of Automotive Medicine, 2005a.

R. Kent, S.-H. H. Lee, K. Darvish, S. Wang, C. S. Poster, A. W. Lange, C. Brede, D. Lange, and F. Matsuoka. Structural and material changes in the aging thorax and their role in crash protection for older occupants. *Stapp Car Crash Journal*, 49:231–249, Nov. 2005b. ISSN 1532-8546. URL http://view.ncbi.nlm.nih.gov/pubmed/17096276.

R. Kent, W. Woods, and O. Bostrom. Fatality risk and the presence of rib fractures. *Annual Proceedings, Association for the Advancement of Automotive Medicine*, 52:73–82, Oct. 2008. ISSN 1943-2461. URL http://www.ncbi.nlm.nih.gov/pmc/articles/PMC3256783/.

R. W. Kent, J. R. Crandall, J. Bolton, P. Prasad, G. Nusholtz, and H. Mertz. The influence of superficial soft tissues and restraint condition on thoracic skeletal injury prediction. *Stapp Car Crash Journal*, 45:183–204, Nov. 2001. ISSN 1532-8546. URL http://view.ncbi.nlm.nih.gov/pubmed/17458745.

R. W. Kent, C. Sherwood, D. Lessley, B. Overby, and F. Matsouka. Age-related changes in the effective stiffness of the human thorax using four loading conditions. In *Proceedings of the International Research Council on the Biomechanics of Injury conference*, volume 31, page 15p. International Research Council on Biomechanics of Injury, 2003b.

M. Kindig, A. G. Lau, and R. W. Kent. Biomechanical response of ribs under quasistatic frontal loading. *Traffic Injury Prevention*, 12(4):377–387, Aug. 2011. ISSN 1538-957X. doi: 10.1080/15389588.2011.583960. URL http://dx.doi.org/10.1080/15389588.2011.583960.

M. W. Kindig and R. W. Kent. Characterization of the centroidal geometry of human ribs. *Journal of Biomechanical Engineering*, 135(11), Nov. 2013. ISSN 1528-8951. doi: 10.1115/1.4025329. URL http://dx.doi.org/10.1115/1.4025329.

E. Kralj, M. Podbregar, N. Kejžar, and J. Balažic. Frequency and number of resuscitation related rib and sternum fractures are higher than generally considered. *Resuscitation*, 93: 136–141, Aug. 2015. ISSN 03009572. doi: 10.1016/j.resuscitation.2015.02.034. URL http://dx.doi.org/10.1016/j.resuscitation.2015.02.034.

C. K. Kroell. *Thoracic response to blunt frontal loading*. Research Laboratories, General Motors Corporation, 1976.

C. K. Kroell, D. C. Schneider, and A. M. Nahum. Impact Tolerance and Response of the Human Thorax. volume 14th, Feb. 1971. doi: 10.4271/710851. URL http://dx.doi.org/10.4271/710851.

C. K. Kroell, D. C. Schneider, and A. M. Nahum. Impact Tolerance and Response of the Human Thorax II. Feb. 1974. doi: 10.4271/741187. URL http://dx.doi.org/10.4271/741187.

A. G. Lau, M. W. Kindig, and R. W. Kent. Morphology, distribution, mineral density and volume fraction of human calcified costal cartilage. *Acta Biomaterialia*, 7(3):1202–1209, Mar. 2011. ISSN 17427061. doi: 10.1016/j.actbio.2010.10.019. URL http://dx.doi.org/10.1016/j.actbio.2010.10.019.

W. Lederer, D. Mair, W. Rabl, and M. Baubin. Frequency of rib and sternum fractures associated with out-of-hospital cardiopulmonary resuscitation is underestimated by conventional chest X-ray. *Resuscitation*, 60(2):157–162, Feb. 2004. ISSN 0300-9572. URL http://view.ncbi.nlm.nih.gov/pubmed/15036733.

W. Y. Lee, W. Y. Yee, P. A. Cameron, and M. J. Bailey. Road traffic injuries in the elderly. *Emergency Medicine Journal : EMJ*, 23(1):42–46, Jan. 2006. ISSN 1472-0213. doi: 10.1136/emj.2005.023754. URL http://dx.doi.org/10.1136/emj.2005.023754.

Z. Li, M. W. Kindig, J. R. Kerrigan, C. D. Untaroiu, D. Subit, J. R. Crandall, and R. W. Kent. Rib fractures under anterior-posterior dynamic loads: experimental and finite-element study. *Journal of Biomechanics*, 43(2):228–234, Jan. 2010. ISSN 1873-2380. doi: 10.1016/j.jbiomech.2009.08.040. URL http://dx.doi.org/10.1016/j.jbiomech.2009.08.040.

D. H. Livingston and C. J. Hauser. Trauma to the chest wall and lung. *Trauma*, 5, 2004.

E. Lizee, S. Robin, E. Song, N. Bertholon, J.-Y. Le Coz, B. Besnault, and F. Lavaste. SAE Technical Paper SeriesDevelopment of a 3D Finite Element Model of the Human Body. In *Stapp Car Crash Conference*, volume 1, 400 Commonwealth Drive, Warrendale, PA, United States, Nov. 1998. SAE International. doi: 10.4271/983152. URL http://dx.doi.org/10.4271/983152.

X. Ma, P. W. Laud, F. Pintar, J.-E. E. Kim, A. Shih, W. Shen, S. B. Heymsfield, D. B. Allison, and S. Zhu. Obesity and non-fatal motor vehicle crash injuries: sex difference effects. *International journal of obesity (2005)*, 35(9):1216–1224, Sept. 2011. ISSN 1476-5497. URL http://view.ncbi.nlm.nih.gov/pubmed/21224830.

S. Marasco and P. Saxena. Surgical rib fixation – Technical aspects. *Injury*, 46(5):929–932, May 2015. ISSN 00201383. doi: 10.1016/j.injury.2014.12.021. URL http://dx.doi.org/10.1016/j.injury.2014.12.021.

S. F. Marasco, I. D. Šutalo, and A. V. Bui. Mode of Failure of Rib Fixation With Absorbable Plates: A Clinical and Numerical Modeling Study. *The Journal of Trauma: Injury, Infection, and Critical Care*, 68(5):1225–1233, May 2010. ISSN 0022-5282. doi: 10.1097/ta.0b013e3181d27cab. URL http://dx.doi.org/10.1097/ta.0b013e3181d27cab.

S. F. Marasco, A. R. Davies, J. Cooper, D. Varma, V. Bennett, R. Nevill, G. Lee, M. Bailey, and M. Fitzgerald. Prospective Randomized Controlled Trial of Operative Rib Fixation in Traumatic Flail Chest. *Journal of the American College of Surgeons*, 216(5):924–932, May 2013. ISSN 10727515. doi: 10.1016/j.jamcollsurg.2012.12.024. URL http://dx.doi.org/10.1016/j.jamcollsurg.2012.12.024.

J. H. Marcus, R. M. Morgan, R. H. Eppinger, D. Kallieris, R. Mattern, and G. Schmidt. Human Response to and Injury from Lateral Impact. In *27th Stapp Car Crash Conference*, volume 1 of *SAE Technical Paper Series*, 400 Commonwealth Drive, Warrendale, PA, United States, Oct. 1983. SAE International. doi: 10.4271/831634. URL http://dx.doi.org/10.4271/831634.

S. S. Margulies, J. R. Rodarte, and E. A. Hoffman. Geometry and kinematics of dog ribs. *Journal of Applied Physiology (Bethesda, Md. : 1985)*, 67(2):707–712, Aug. 1989. ISSN 8750-7587. URL http://view.ncbi.nlm.nih.gov/pubmed/2793673.

J. W. Melvin, D. Mohan, and R. L. Stalnaker. Occupant Injury Assessment Criteria. In *SAE Automobile Engineering and Manufacturing Meeting*, volume 1 of *SAE Technical Paper Series*, 400 Commonwealth Drive, Warrendale, PA, United States, Feb. 1975. SAE International. doi: 10.4271/750914. URL http://dx.doi.org/10.4271/750914.

H. J. Mertz, A. L. Irwin, J. W. Melvin, R. L. Stanaker, and M. S. Beebe. Size, weight and biomechanical impact response requirements for adult size small female and large male dummies. Technical report, SAE Technical Paper, 1989.

H. J. Mertz, A. L. Irwin, and P. Prasad. Biomechanical and scaling bases for frontal and side impact injury assessment reference values. *Stapp Car Crash Journal*, 47:155–188, Oct. 2003. ISSN 1532-8546. URL http://view.ncbi.nlm.nih.gov/pubmed/17096249.

M. Mohr, E. Abrams, C. Engel, W. B. Long, and M. Bottlang. Geometry of human ribs pertinent to orthopedic chest-wall reconstruction. *Journal of Biomechanics*, 40(6):1310–1317, Jan. 2007. ISSN 0021-9290. doi: 10.1016/j.jbiomech.2006.05.017. URL http://dx.doi.org/10.1016/j.jbiomech.2006.05.017.

R. M. Morgan, R. H. Eppinger, M. P. Haffner, N. Yoganandan, F. A. Pintar, A. Sances, J. R. Crandall, W. D. Pilkey, G. S. Klopp, D. Kallieris, E. Miltner, R. Mattem, S. M. Kuppa, and C. L. Sharpless. Thoracic Trauma Assessment Formulations for Restrained Drivers in Simulated Frontal Impacts. In *Stapp Car Crash Conference*, volume 1, 400 Commonwealth Drive, Warrendale, PA, United States, Nov. 1994. SAE International. doi: 10.4271/942206. URL http://dx.doi.org/10.4271/942206.

A. Morris, R. Welsh, and A. Hassan. Requirements for the crash protection of older vehicle passengers. *Annual proceedings / Association for the Advancement of Automotive Medicine. Association for the Advancement of Automotive Medicine*, 47:165–180, 2003. ISSN 1540-0360. URL http://www.ncbi.nlm.nih.gov/pmc/articles/PMC3217559/.

A. M. Nahum, C. W. Gadd, D. C. Schneider, and C. K. Kroell. The biomechanical basis for chest impact protection. I. Force-deflection characteristics of the thorax. *The Journal of Trauma*, 11(10):874–882, Oct. 1971. ISSN 0022-5282. doi: 10.1097/00005373-197110000-00009. URL http://dx.doi.org/10.1097/00005373-197110000-00009.

National Highway Traffic Safety Administration. FARS Encyclopedia. urlhttp://www-fars.nhtsa.dot.gov, 2014. [Online; accessed 20-July-2016].

R. F. Neathery. Analysis of Chest Impact Response Data and Scaled Performance Recommendations. In *18th Stapp Car Crash Conference*, volume 1 of *SAE Technical Paper 741188*, 400 Commonwealth Drive, Warrendale, PA, United States, Feb. 1974. SAE International. doi: 10.4271/741188. URL http://dx.doi.org/10.4271/741188.

R. F. Neathery, C. K. Kroell, and H. J. Mertz. Prediction of Thoracic Injury from Dummy Responses. In *19th Stapp Car Crash Conference (1975)*, volume 1 of *SAE Technical Paper Series*, 400 Commonwealth Drive, Warrendale, PA, United States, Feb. 1975. SAE International. doi: 10.4271/751151. URL http://dx.doi.org/10.4271/751151.

C. L. Ogden, M. D. Carroll, B. K. Kit, and K. M. Flegal. Prevalence of obesity in the United States, 2009-2010. *NCHS data brief*, (82):1–8, Jan. 2012. ISSN 1941-4927. URL http://view.ncbi.nlm.nih.gov/pubmed/22617494.

J. M. Ortman, V. A. Velkoff, H. Hogan, and Others. An aging nation: the older population in the United States. *Washington, DC: US Census Bureau*, pages 25–1140, 2014.

C. S. Parenteau, D. Zuby, K. Brolin, M. Y. Svensson, C. Palmertz, and S. C. Wang. Restrained Male and Female Occupants in Frontal Crashes: Are We Different? In *2013 IRCOBI Conference Proceedings*, 2013.

R. Perz, J. Toczyski, and D. Subit. Variation in the human ribs geometrical properties and mechanical response based on X-ray computed tomography images resolution. *Journal of the Mechanical Behavior of Biomedical Materials*, 41:292–301, Jan. 2015. ISSN 1878-0180. doi: 10.1016/j.jmbbm.2014.07.036. URL http://dx.doi.org/10.1016/j.jmbbm.2014.07.036.

D. F. Preusser, A. F. Williams, S. A. Ferguson, R. G. Ulmer, and H. B. Weinstein. Fatal crash risk for older drivers at intersections. *Accident; Analysis and Prevention*, 30(2): 151–159, Mar. 1998. ISSN 0001-4575. doi: 10.1016/S0001-4575(97)00090-0. URL http://dx.doi.org/10.1016/S0001-4575(97)00090-0.

J. Pulido, G. Barrio, J. Hoyos, E. Jiménez-Mejías, M. D. Mar, S. Houwing, and P. Lardelli-Claret. The role of exposure on differences in driver death rates by gender and age: Results of a quasi-induced method on crash data in Spain. *Accident; Analysis and Prevention*, 94:162–167, Sept. 2016. ISSN 1879-2057. URL http://view.ncbi.nlm.nih.gov/pubmed/27305640.

T. M. Rice and M. Zhu. Driver obesity and the risk of fatal injury during traffic collisions. *Emergency Medicine Journal*, 31(1):9–12, Jan. 2014. ISSN 1472-0213. doi: 10.1136/emermed-2012-201859. URL http://dx.doi.org/10.1136/emermed-2012-201859.

S. A. Ridella, J. D. Rupp, and K. Poland. Age-related differences in AIS 3+ crash injury risk, types, causation and mechanisms. In *Ircobi Conference*, volume 2012, 2012.

S. B. Roberts. Simple Quantitative Anatomical Model for In-vivo Human Ribs. *Journal of Bioengineering*, 1(4):443–453, 1977.

S. B. Roberts and P. H. Chen. Global geometric characteristics of typical human ribs. *Journal of Biomechanics*, 5(2):191–201, Mar. 1972. ISSN 00219290. doi: 10.1016/0021-9290(72)90055-3. URL http://dx.doi.org/10.1016/0021-9290(72)90055-3.

S. Robin. HUMOS: human model for safety–a joint effort towards the development of refined human-like car occupant models. In *17th international technical conference on the enhanced safety vehicle*, page 297, 2001.

E. Romano, T. Kelley-Baker, and R. B. Voas. Female involvement in fatal crashes: Increasingly riskier or increasingly exposed? *Accident Analysis & Prevention*, 40 (5):1781–1788, Sept. 2008. ISSN 0001-4575. doi: 10.1016/j.aap.2008.06.016. URL http://dx.doi.org/10.1016/j.aap.2008.06.016.

J. Ruan, R. El-Jawahri, L. Chai, S. Barbat, and P. Prasad. Prediction and analysis of human thoracic impact responses and injuries in cadaver impacts using a full human body finite

element model. *Stapp Car Crash Journal*, 47:299–321, Oct. 2003. ISSN 1532-8546. URL http://view.ncbi.nlm.nih.gov/pubmed/17096254.

J. S. Ruan, R. El-Jawahri, S. Barbat, and P. Prasad. Biomechanical Analysis of Human Abdominal Impact Responses and Injuries through Finite Element Simulations of a Full Human Body Model. *Stapp Car Crash Journal*, 49:343–366, Nov. 2005. ISSN 1532-8546. URL http://view.ncbi.nlm.nih.gov/pubmed/17096281.

K. Saladin. *Anatomy & Physiology: A Unity of Form and Function*. McGraw-Hill Science/Engineering/Math, 5 edition, Sept. 2009. ISBN 0077361350. doi: 10.1086/343592. URL http://dx.doi.org/10.1086/343592.

A. B. Schultz, D. R. Benson, and C. Hirsch. Force-deformation properties of human ribs. *Journal of Biomechanics*, 7(3):303–309, May 1974. ISSN 00219290. doi: 10.1016/0021-9290(74)90023-2. URL http://dx.doi.org/10.1016/0021-9290(74)90023-2.

J. M. Shaw, R. G. Herriott, J. D. McFadden, B. R. Donnelly, and J. H. Bolte. Oblique and lateral impact response of the PMHS thorax. *Stapp Car Crash Journal*, 50:147–167, Nov. 2006. ISSN 1532-8546. URL http://view.ncbi.nlm.nih.gov/pubmed/17311163.

X. Shi, L. Cao, M. P. Reed, J. D. Rupp, C. N. Hoff, and J. Hu. A statistical human rib cage geometry model accounting for variations by age, sex, stature and body mass index. *Journal of Biomechanics*, 47(10):2277–2285, July 2014. ISSN 00219290. doi: 10.1016/j.jbiomech.2014.04.045. URL http://dx.doi.org/10.1016/j.jbiomech.2014.04.045.

M. Shields, M. D. Carroll, and C. L. Ogden. Adult obesity prevalence in Canada and the United States. *NCHS data brief*, (56):1–8, Mar. 2011. ISSN 1941-4927. URL http://view.ncbi.nlm.nih.gov/pubmed/21592419.

D. E. Slice and J. Stitzel. Landmark-based geometric morphometrics and the study of allometry. In *Proceedings of the Society of Automotive Engineers Digital Human Modeling for Design and Engineering Symposium*, volume 113, pages 199–207. Society of Automotive Engineers, 2004.

J. Sobotta. *Atlas and text-book of human anatomy*, volume 3. Saunders, 1911.

J. Staal, B. van Ginneken, and M. A. Viergever. Automatic rib segmentation and labeling in computed tomography scans using a general framework for detection, recognition and segmentation of objects in volumetric data. *Medical Image Analysis*, 11(1):35–46, Feb. 2007. ISSN 1361-8415. doi: 10.1016/j.media.2006.10.001. URL http://dx.doi.org/10.1016/j.media.2006.10.001.

R. L. Stalnaker, C. Tarrière, A. Fayon, G. Walfisch, M. Balthazard, J. Masset, C. Got, and A. Patel. Modification of Part 572 Dummy for Lateral Impact According to Biomechanical Data. In *23rd Stapp Car Crash Conference*, volume 1 of *SAE Technical Paper*

Series, 400 Commonwealth Drive, Warrendale, PA, United States, Feb. 1979. SAE International. doi: 10.4271/791031. URL http://dx.doi.org/10.4271/791031.

H. Tanaka, T. Yukioka, Y. Yamaguti, S. Shimizu, H. Goto, H. Matsuda, and S. Shimazaki. Surgical Stabilization of Internal Pneumatic Stabilization? A Prospective Randomized Study of Management of Severe Flail Chest Patients. *The Journal of Trauma: Injury, Infection, and Critical Care*, 52(4):727–732, Apr. 2002. ISSN 0022-5282. doi: 10.1097/00005373-200204000-00020. URL http://dx.doi.org/10.1097/00005373-200204000-00020.

X. Trosseille, P. Baudrit, T. Leport, and G. Vallancien. Rib cage strain pattern as a function of chest loading configuration. *Stapp Car Crash Journal*, 52:205–231, Nov. 2008. ISSN 1532-8546. URL http://view.ncbi.nlm.nih.gov/pubmed/19085164.

United Nations. World Population Ageing 2015. *Department of Economic and Social Affairs, Population Division*, (ST/ESA/SER.A/390), 2015.

P. Vezin and J. P. Verriest. Development of a set of numerical human models for safety. In *19th International Technical Conference on the Enhanced Safety of Vehicles, Washington DC*, pages 6–9, 2005.

D. C. Viano, I. V. Lau, C. Asbury, A. I. King, and P. Begeman. Biomechanics of the human chest, abdomen, and pelvis in lateral impact. *Accident Analysis & Prevention*, 21(6): 553–574, Dec. 1989. ISSN 0001-4575. doi: 10.1016/0001-4575(89)90070-5. URL http://dx.doi.org/10.1016/0001-4575(89)90070-5.

D. C. Viano, C. S. Parenteau, and M. L. Edwards. Crash Injury Risks for Obese Occupants Using a Matched-Pair Analysis. *Traffic Injury Prevention*, 9(1):59–64, Feb. 2008. doi: 10.1080/15389580701737645. URL http://dx.doi.org/10.1080/15389580701737645.

Y. Wang, L. Cao, Z. Bai, M. P. Reed, J. D. Rupp, C. N. Hoff, and J. Hu. A parametric ribcage geometry model accounting for variations among the adult population. *Journal of Biomechanics*, 2016. ISSN 00219290. doi: 10.1016/j.jbiomech.2016.06.020. URL http://dx.doi.org/10.1016/j.jbiomech.2016.06.020.

A. A. Weaver, S. L. Schoell, and J. D. Stitzel. Morphometric analysis of variation in the ribs with age and sex. *Journal of Anatomy*, 225(2):246–261, Aug. 2014. ISSN 1469-7580. doi: 10.1111/joa.12203. URL http://dx.doi.org/10.1111/joa.12203.

E. W. Weisstein. Logarithmic spiral. From MathWorld - A Wolfram Web Resource. URL http://mathworld.wolfram.com/LogarithmicSpiral.html. Last visited on 4/4/2016.

N. Yoganandan, F. A. Pintar, D. Skrade, W. Chmiel, J. M. Reinartz, and A. Sances. Thoracic Biomechanics with Air Bag Restraint. In *Stapp Car Crash Conference*, volume 1 of *SAE Technical Paper Series*, 400 Commonwealth Drive, Warrendale, PA, United States, Nov. 1993. SAE International. doi: 10.4271/933121. URL http://dx.doi.org/10.4271/933121.

J. Zhao and G. Narwani. Development of a human body finite element model for restraint system R&D applications. In *The 19th International Technical Conference on the Enhanced Safety of Vehicles (ESV), Paper*, number 05-0399, 2005.

Q. Zhou, S. W. Rouhana, and J. W. Melvin. Age Effects on Thoracic Injury Tolerance. In *40th Stapp Car Crash Conference*, volume 1 of *SAE Technical Paper Series*, pages 137–148, 400 Commonwealth Drive, Warrendale, PA, United States, Nov. 1996. Society of Automotive Engineers SAE, SAE International. doi: 10.4271/962421. URL http://dx.doi.org/10.4271/962421.